Università degli Studi di Bologna

FACOLTÀ DI SCIENZE MATEMATICHE, FISICHE E NATURALI

Dottorato di Ricerca in Fisica
XIV ciclo

Neutrino oscillation studies with a massive magnetized calorimeter

Tesi presentata da:
Marco Selvi

Tutors:
Prof. M. Basile
Prof.ssa G. Sartorelli

Coordinatore del dottorato:
Prof. G. Venturi

Anno Accademico 2000/01

Contents

Chapter 1

Introduction

The question whether neutrinos are massive, and hence the question of the existence of neutrino oscillations, is currently one of the main unsettled challenges in physics. All experiments measuring the flux of solar neutrinos observe a deficit compared to the prediction of solar models [1]. The ratio of muon to electron events observed in atmospheric neutrino interactions is measured by most experiments to be less than expected from models of cosmic ray interactions in the atmosphere [2]. The measurement of the up/down asymmetry of this ratio by the Super-Kamiokande collaboration [3] is generally considered to be the strongest evidence for neutrino oscillations so far. The K2K experiment [4] observes a number of neutrino interactions lower than expected and is consistent with the oscillation hypothesis [5] [6], even if the statistic is too small to exclude other phenomena. Furthermore, the LSND experiment has observed possible oscillation signals in the $\bar{\nu}_\mu - \bar{\nu}_e$ and $\nu_\mu - \nu_e$ channels [7]. Finally, neutrinos are a candidate for a partial solution to the missing dark matter problem [8] if at least one mass eigenstate lies in the eV range. These observations make the study of neutrino oscillations a very challenging task.

While the cumulative evidence for neutrino oscillations is very striking, the final proof that the observed anomalies are actually due to neutrino oscillations is still outstanding. In particular, the current observations of atmospheric neutrinos are all consistent with the hypothesis of maximal ν_μ oscillations, but do not yet exclude some alternative unconventional explanations [9, 10, 11, 12].

The main physics goal of the massive (34 kt) magnetized calorimeter studied in this thesis is to establish the occurrence of neutrino oscillations in atmospheric neutrinos through the explicit observation of the full first oscillation swing in ν_μ disappearance [13], and to investigate and presumably exclude alternative explanations. This also yields a significantly improved measurement of the oscillation parameters with respect to previous measurements.
The strong magnetic field, adopted in the detector design to extend the sensitivity to the full parameter range allowed by current experiments, is a novel feature among atmospheric neutrino detectors.

A completely new fitting procedure for the measurement of the direction and the momentum of the outgoing muons has been adopted, in this work, in the analysis of atmospheric neutrino

simulated data. It results somewhat more efficient, while having comparable resolutions with the one used in the Proposal. It allows also an improvement in the reconstruction of the muon direction, both for contained and partially-contained events.
A staged approach in the detector construction has been studied. Results on the physics reach of a first 12 kt module are presented.
Moreover, a full simulation of a different geometry of the apparatus, based on vertical iron planes interleaved with sensitive elements, has been developed and results on atmospheric neutrinos are presented.

In December 1999, the CERN Council approved the construction of a Long Baseline Beam from CERN to Gran Sasso. It is a wide-band ν_μ beam, optimized for τ appearance. We study the performances of the detector in reconstructing such kind of events, that present a completely different pattern with respect to the atmospheric sample. The measurement of the oscillation pattern performed with atmospherics can be usefully supplemented by measurements in the CERN to Gran Sasso neutrino beam, especially if Δm^2 is in the upper part of the SK allowed region.

Among the various future project for neutrino beams, we study in details the physics reach of a neutrino-factory [14], a neutrino beam coming from the decay of accelerated muons. A neutrino-factory provides an intense, well-known, wide-band beam of ν_e and ν_μ of opposite helicity. Such a beam allows to study the oscillation between ν_e and ν_μ even if the mixing angle (θ_{13}) is very small. Other topics are the study of matter effects and the sign of Δm^2; moreover, if the solar solution is the Large Mixing Angle, CP violation in the leptonic sector is explorable. We study in details the charge recognition of the detector and the ability to separate the muon from the hadronic shower in the CC interaction, in order to reject the various sources of background. Test beam results on a prototype of the detector are analyzed in order to prove that the requested resolution on the hadronic shower direction could be achieved. To show the detector sensitivity, we perform an analysis to determine the oscillation parameter region in which it is possible to discover a non-zero θ_{13} value, given the estimated signal efficiency and background rejection.

The thesis is organized as follows:
Chapter 2 deals with the physics of neutrino oscillations in vacuum and in matter.
The status of the current measurement about neutrino oscillations is shown in chapter 3 as well as the description of the future projects and the need and motivation for a massive magnetized detector.
The experimental set-up is described in chapter 4.
Details of the simulation and analysis strategies respectively for atmospherics, CNGS and ν-factory events are documented in chapters 5, 6 and 7.
Finally, chapter 8 summarizes the general conclusions.

Chapter 2

Neutrino Physics

2.1 General properties of neutrinos

What do we know about neutrinos? Neutrinos are electrically neutral particles of spin 1/2. There are at least three species (or flavours) of very light neutrinos, ν_e, ν_μ and ν_τ, which are left handed, and their antiparticles $\bar{\nu}_e$, $\bar{\nu}_\mu$ and $\bar{\nu}_\tau$, which are right handed. Electron-type neutrinos and antineutrinos are produced in nuclear $\beta^\pm$ decay,

$$\begin{aligned} A(Z,N) &\to A(Z+1,N-1) + e^- + \bar{\nu}_e\,, \\ A(Z,N) &\to A(Z-1,N+1) + e^+ + \nu_e\,, \end{aligned} \tag{2.1}$$

and in particular in the neutron decay process $n \to p + e^- + \bar{\nu}_e$. They are also produced in muon decays $\mu^\pm \to e^\pm + \bar{\nu}_\mu(\nu_\mu) + \nu_e(\bar{\nu}_e)$, and as a subdominant mode, in pion decays $\pi^\pm \to e^\pm + \nu_e(\bar{\nu}_e)$ and in some other decays and reactions. The elementary processes responsible for the nuclear beta decays or pion decays are actually the quark transitions $u \to d + e^+ + \nu_e$ and $d \to u + e^- + \bar{\nu}_e$. Muon neutrinos and antineutrinos are produced in muon decays, pion decays $\pi^\pm \to \mu^\pm + \nu_\mu(\bar{\nu}_\mu)$ and some other processes. Neutrinos of the third type, tau, are expected to be produced in $\tau^\pm$ decays. They have been recentely experimentally detected by the DONUT experiment at Fermilab [15]. Neutrinos of each flavour participate in reactions in which the charged lepton of the corresponding type are involved; these reactions are mediated by $W^\pm$ bosons. Thus, these so-called charged current reactions involve the processes $W^\pm \to l_a^\pm + \nu_a(\bar{\nu}_a)$ where $a = e,\ \mu$ or τ, or related processes. Neutrinos can also participate in neutral current reactions mediated by Z^0 bosons; these are elastic or quasielastic scattering processes and decays $Z^0 \to \nu_a \bar{\nu}_a$.

The latter process allowed us to count the number of light neutrino species that have the usual electroweak interactions. Indeed, neutrinos from the Z^0 decays are not detected, and therefore the difference between the measured total width of the Z^0 boson and the sum of its partial widths of decay into quarks and charged leptons, the so-called invisible width, $\Gamma_{inv} = \Gamma_{tot} - \Gamma_{vis} = 498 \pm 4.2$ MeV, should be due to the decay into $\nu\bar{\nu}$ pairs. Taking into account that the partial width of Z^0 decay into one $\nu\bar{\nu}$ pair $\Gamma_{\nu\bar{\nu}} = 166.9$ MeV one finds the number of the light active neutrino species [16]:

$$N_\nu = \frac{\Gamma_{inv}}{\Gamma_{\nu\bar{\nu}}} = 2.994 \pm 0.012\,, \tag{2.2}$$

in a very good agreement with the existence of the three neutrino flavours. There are also indirect limits on the number of light ($m < 1$ MeV) neutrino species (including possible electroweak singlet, i.e. “sterile” neutrinos) coming from big bang nucleosynthesis:

$$N_\nu < 3.3\,, \tag{2.3}$$

though this limit is less reliable than the laboratory one (2.2), and probably four neutrino species can still be tolerated [17].

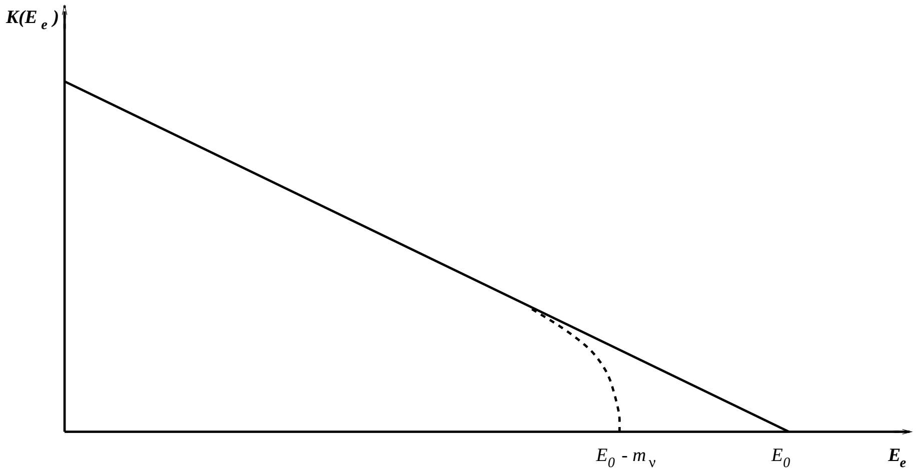

Figure 2.1: Kurie plots for $m_\nu = 0$ (solid line) and $m_\nu \neq 0$ (dashed line)

What do we know about the neutrino mass? Direct kinematic searches of neutrino mass produced only the upper limits [16]:

$$m_{\nu_1} < 2.5 \text{ eV at } 95\% \text{ c.l. (Troitsk)}\,; < 6 \text{ eV at } 95\% \text{ c.l. (Mainz)}\,; \tag{2.4}$$

$$m_{\nu_2} < 170 \text{ keV at } 90\% \text{ c.l. (PSI; } \pi^+ \to \mu^+ + \nu_\mu)\,; \tag{2.5}$$

$$m_{\nu_3} < 18.2 \text{ MeV at } 95\% \text{ c.l. (ALEPH; } \tau^- \to 5\pi + \nu_\tau) \tag{2.6}$$

Here ν_1, ν_2 and ν_3 are the primary mass components of ν_e, ν_μ and ν_τ, respectively. The limits in eqs. (2.5) and (2.6) come from the comparison of the total energy release with the energy of decay products. The limits in eq. (2.4) are obtained from the tritium beta decay experiments and are based on the analyses of the so-called Kurie plot. The electron spectrum in the allowed β decay is

$$N_e(E_e)dE_e \;\propto\; F(Z,E_e)\sqrt{E_e^2 - m_e^2}\,E_e(E_0 - E_e)^2\,dE_e\,, \quad (m_\nu = 0)\,; \tag{2.7}$$

$$N_e(E_e)dE_e \;\propto\; F(Z,E_e)\sqrt{E_e^2 - m_e^2}\,E_e(E_0 - E_e)\sqrt{(E_0 - E_e)^2 - m_\nu^2}\,dE_e\,, \quad (m_\nu \neq 0)\,. \tag{2.8}$$

Here $F(Z,E_e)$ is the well known function which takes into account the interaction between the emitted electron and the nucleus in the final state and E_0 is the energy release. Thus, the shape of the β spectrum should depend on whether or not neutrinos have a mass. It follows from these equations that the plot of the Kurie function $K(E_e) \equiv [N_e(E_e)/(F(Z,E_e)p_eE_e)]^{1/2}$ versus E_e should be a straight line when $m_\nu = 0$ but should have a different shape close to the endpoint of the spectrum when $m_\nu \neq 0$ (fig. 2.1). Analyses of the Kurie plots for beta decay of tritium which has a very low energy release give the results of eq. (2.4). However, all the experiments showed some excess of the number of electrons near the endpoint of the spectrum rather than a deficiency that is expected if $m_\nu \neq 0$. This excess is most likely due to unknown systematic effects. For this reason the conservative upper limit on the lightest neutrino mass recommended by the Particle Data Group [16] is

$$m_1 < 15 \text{ eV} \tag{2.9}$$

rather than the limits in (2.4).

Are neutrinos Dirac particles (like quarks or charged leptons) or Majorana particles? In other words, can neutrinos be their own antiparticles? It is known experimentally that neutrinos emitted in β^- decay (which we call electron antineutrinos) cannot be captured in reactions which are caused by electron neutrinos; for example, the reaction $\bar{\nu}_e + {}^{37}\text{Cl} \to {}^{37}\text{Ar} + e^-$ does not occur, whereas the reaction $\nu_e + {}^{37}\text{Cl} \to {}^{37}\text{Ar} + e^-$ does, and in fact was used in the first experiment to detect the solar neutrinos. Does this mean that neutrinos are different from antineutrinos, i.e. cannot be Majorana particles? Not necessarily. The reason is that the weak interactions that are responsible for neutrino interactions are chiral $(V - A)$: in the Cl-Ar reaction mentioned above, only neutrinos of left handed chirality can be detected. The particles which we call $\bar{\nu}_e$ are right handed, i.e. have the "wrong chirality", and so cannot participate in the Cl-Ar reaction (this is called "chiral prohibition"). If neutrinos are massive, the chirality (i.e. $1 \pm \gamma_5$) is not a good quantum number, and an electron antineutrino which was produced right handed can develop a small left handed component, so that the reaction $\bar{\nu}_e + {}^{37}\text{Cl} \to {}^{37}\text{Ar} + e^-$ can become possible. However, the "wrong chirality" admixture is of the order m_ν / E, i.e. extremely small due to the smallness of the neutrino mass compared to typical beta decay energies. Therefore the probability of the $\bar{\nu}_e + {}^{37}\text{Cl} \to {}^{37}\text{Ar} + e^-$ process should be suppressed by the factor $(m_\nu / E)^2$, which can be the reason for its non-observation.

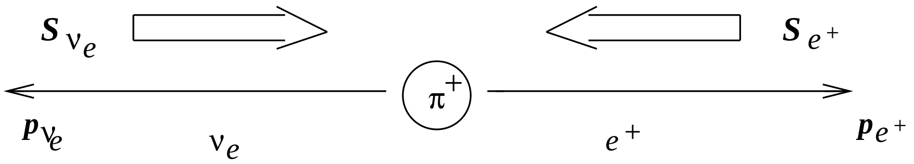

Figure 2.2: Charged pion decay

On of the most outstanding manifestations of the chiral prohibition rule are the decays of charged pions. They also show that one should carefully discriminate between the chirality $(1 \pm \gamma_5)$ and helicity, which is the projection of the spin of the particle on its momentum. In the limit of massless fermions they coincide, but for massive fermions they do not. Let us assume that neutrinos are massless and consider the decay $\pi^+ \to l^+ + \nu_l$ of pions at rest, where l^+ is μ^+ or e^+ and ν_l is the corresponding neutrino. The $V - A$ structure of weak interactions requires the emitted ν_l to be of left handed chirality. For $m_\nu = 0$ this also means that it has the left handed (or negative) helicity with its spin antiparallel to its momentum. Conservation of total angular momentum then requires l^+ to be of negative helicity, too (see fig. 2.2). However, the l^+ are antiparticles, and due to the $V - A$ structure of weak interactions they must be produced in the states of right handed chirality. Therefore the amplitude of the process must be proportional to the admixture of right handed chirality in left handed (negative) helicity of the charged lepton, i.e. to its mass: $A(\pi^+ \to l^+ + \nu_l) \propto m_l$. We therefore expect

$$R_\pi \equiv \frac{\Gamma(\pi^+ \to e^+ + \nu_e)}{\Gamma(\pi^+ \to \mu^+ + \nu_\mu)} = \left(\frac{m_e}{m_\mu}\right)^2 \left(\frac{m_\pi^2 - m_e}{m_\pi^2 - m_\mu^2}\right)^2 = 1.28 \times 10^{-4} . \tag{2.10}$$

where we have taken into account the difference of the phase space factors for the decays into μ^+ and e^+. Experimentally we have

$$R_\pi = (1.230 \pm 0.004) \times 10^{-4} , \tag{2.11}$$

in a very good agreement with the theoretical prediction; the 4% difference is actually due to the fact that (2.10) does not include radiation corrections.

Neutrinos are elusive particles, and neutrino experiments are very difficult. This is because the interactions of neutrinos are mediated by heavy $W^\pm$ and Z^0 bosons and so at low energies they are very weak. The mean free path of a 1 MeV neutrino in lead is about 1 light year! Therefore neutrino detection requires very large detectors and/or very intense neutrino beams.

What are the main sources of neutrinos? One of the strongest neutrino sources is our sun. It emits about 2×10^{38} electron neutrinos per second, leading to the neutrino flux at the surface of the earth of $\sim 6 \times 10^{10}$ $cm^{-2}s^{-1}$ in the energy range $E \leq 0.42$ MeV and $\sim 5 \times 10^6$ $cm^{-2}s^{-1}$ in the energy range 0.8 MeV $\leq E \leq$ 15 MeV. Nuclear power plants are a powerful source of electron antineutrinos. A 3 GW plant emits about 7.7×10^{20} $\bar{\nu}_e$ of the energy $\sim$ a few MeV per second and creates a flux of $\sim 6 \times 10^{11}$ $cm^{-2}s^{-1}$ at 100 m. At remote locations the averaged $\bar{\nu}_e$ number density created by all nuclear power plants on the earth is about $10^6 - 10^7$ cm^{-3}. The relic neutrinos, i.e. the neutrinos left over from the early epochs of the evolution of the universe, have a number density of about 110 cm^{-3} for each neutrino species and a black-body spectrum with the average energy of about 5×10^{-4} eV. Natural radioactivity of the earth results in the flux of $\sim 6 \times 10^6$ $cm^{-2}s^{-1}$ (or number density of $\sim 2 \times 10^{-4}$ cm^{-3}) of neutrinos of the energy $E \leq 1$ MeV. The flux of atmospheric neutrinos at the earth's surface is $\sim 10^{-1}$ $cm^{-2}s^{-1}$. An important tool for studying neutrino properties are particle accelerators which produce neutrino beams of the energy ranging typically between 30 MeV and 30 GeV. Finally, a very rare and short-lived but yet a very important source of neutrinos are type II supernovae. They emit $\sim 6 \times 10^{58}$ neutrinos and antineutrinos of all flavours over the time interval of about 10 s and with the typical energies $E \leq 30$ MeV. Observation of the neutrino burst from the supernova 1987A allowed us to obtain important constraints on neutrino properties.

2.2 Neutrino Oscillation in vacuum

Neutrino oscillations are the most sensitive probe of neutrino mass. Solar and supernova neutrino experiments may be able to discover the neutrino mass as small as 10^{-5} eV or even smaller, far beyond the reach of the direct kinematic search experiments. The idea of neutrino oscillations was first introduced by Pontecorvo [18]. The essence of this effect is very simple, and examples of the oscillation phenomena can be found in nearly every textbook on quantum mechanics. Consider, for example, a two-level quantum system. If the system is in one of its stationary states $|\Psi_i\rangle$ (eigenstates of the Hamiltonian), it will remain in this state, and the time evolution of the wave function is very simple – it just picks up a phase factor: $|\Psi_i(t)\rangle = e^{-iE_it}|\Psi_i(0)\rangle$.

If, however, a state is prepared which is not one of the eigenstates of the Hamiltonian of the system, the probability to find the system in this state will oscillate in time with the frequency $\omega_{21} = E_2 - E_1$ where E_1 and E_2 are the eigenenergies of the system.

In the case of neutrino oscillations, neutrinos are produced by the charged-current weak interactions and therefore are weak-eigenstate neutrinos ν_e, ν_μ or ν_τ. However, the neutrino mass matrix in this (flavour) basis is in general not diagonal. This means that the mass eigenstate neutrinos ν_1, ν_2 and ν_3 (the states that diagonalize the neutrino mass matrix, i.e. the free propagation eigenstates) are in general different from the flavour eigenstates. Therefore the probability of finding a neutrino created in a given flavour state to be in the same state (or any other flavour state) oscillates with time.

We shall consider neutrino oscillations in the case of Dirac neutrino mass term and then will comment on the Majorana and Dirac + Majorana cases. The part of the Lagrangian that describes the lepton masses and charged current interactions is

$$-\mathcal{L}_{W+m} = \frac{g}{\sqrt{2}}\,\overline{e}'_{aL}\,\gamma^\mu\,\nu'_{aL}\,W^-_\mu + (m_l)_{ab}\overline{e}'_{aL}e'_{bR} + (m_D)_{ab}\,\overline{\nu}'_{aL}\nu'_{bR} + h.c. \tag{2.12}$$

Here the primes are used to denote the flavour eigenstate fields. It follows from this expression that the individual lepton flavours L_e, L_μ and L_τ are not conserved when the Dirac neutrino mass term is present, but the total lepton number $L = L_e + L_\mu + L_\tau$ is still conserved.

The mass matrix of charged leptons m_l and the neutrino mass matrix m_D are general complex matrices which can be diagonalized by bi-unitary transformations. Let us write

$$e'_L = V_L\,e_L\,, \qquad e'_R = V_R\,e_R \qquad \nu'_L = U_L\,\nu_L\,, \qquad \nu'_R = U_R\,\nu_R\,, \tag{2.13}$$

and choose the unitary matrices V_L, V_R, U_L and U_R so that they diagonalize the mass matrices of charged leptons and neutrinos:

$$V_L^\dagger\,m_l\,V_R = (m_l)_{diag}\,, \qquad U_L^\dagger\,m_D\,U_R = (m_D)_{diag}\,. \tag{2.14}$$

The "unprimed" fields e_{iL}, e_{iR}, ν_{iL} and ν_{iR} are then the components of the Dirac mass eigenstate fields $e_i = e_{iL} + e_{iR}$ and $\nu_i = \nu_{iL} + \nu_{iR}$. The Lagrangian in eq. (2.12) can be written in the mass eigenstate basis as

$$-\mathcal{L}_{W+m} = \frac{g}{\sqrt{2}}\,\overline{e_i}\,\gamma^\mu\,(V_L^\dagger U_L)_{ij}\,\nu_{Lj}\,W^-_\mu + m_{li}\overline{e}_{Li}e_{Ri} + m_{Di}\,\overline{\nu}_{Li}\nu_{Ri} + h.c.\,, \tag{2.15}$$

where m_{li} are the charged lepton masses and m_{Di} are the neutrino masses. The matrix $U = V_L^\dagger U_L$ is called the lepton mixing matrix, or Maki-Nakagawa-Sakata (MNS) matrix [19]. It is the leptonic analog of the CKM mixing matrix. It relates a neutrino flavour eigenstate $|\nu'_a\rangle$ produced or absorbed alongside with the corresponding charged lepton, to the mass eigenstates $|\nu_i\rangle$:

$$|\nu'_a\rangle = U^*_{ai}\,|\nu_i\rangle\,, \tag{2.16}$$

In what follows, to simplify the notation we shall omit the primes and distinguish between the flavour and mass eigenstates just by using the indices from the beginning of the Latin alphabet for the former and from its middle for the latter. Assume that at a time $t = 0$ the flavour eigenstate $|\nu_a\rangle$ was produced. What is the probability to find the neutrino in a state $|\nu_b\rangle$ at a later time t? Time evolution of the flavour eigenstates is not simple, therefore it is more convenient to follow the evolution of the system in the mass eigenstate basis (we shall discuss evolution in the flavour basis in sec. 2.3). The initial state at $t = 0$ is $|\nu(0)\rangle = |\nu_a\rangle = U^*_{aj}|\nu_j\rangle$; the neutrino state at a later time t is then

$$|\nu(t)\rangle = U^*_{aj}\, e^{-iE_j t}|\nu_j\rangle\,. \tag{2.17}$$

The probability amplitude of finding the neutrino at the time t in a flavour state $|\nu_b\rangle$ is

$$A(\nu_a \to \nu_b;\, t) = \langle\nu_b|\nu(t)\rangle = U^*_{aj}\, e^{-iE_j t}\, \langle\nu_b|\nu_j\rangle = U_{bi}U^*_{aj}\, e^{-iE_j t}\, \langle\nu_i|\nu_j\rangle = U_{bj}\, e^{-iE_j t}\, U^*_{aj}\,. \tag{2.18}$$

As usual, the sum over all intermediate states j is implied. The last expression here has a very simple physical meaning. The factor $U^*_{aj} = U^\dagger_{ja}$ is the amplitude of transformation of the initial flavour eigenstate neutrino ν_a into a mass eigenstate one ν_j; the factor $e^{-iE_j t}$ is just the propagator describing the time evolution of the mass eigenstate neutrino ν_j in the energy representation, and finally the factor U_{bj} converts the time-evolved mass eigenstate ν_j into the flavour eigenstate ν_b. The neutrino oscillation probability, i.e. the probability of the transformation of a flavour eigenstate neutrino ν_a into another one ν_b, is then

$$P(\nu_a \to \nu_b;\, t) = |A(\nu_a \to \nu_b;\, t)|^2 = |U_{bj}\, e^{-iE_j t}\, U^*_{aj}|^2\,. \tag{2.19}$$

We have discussed neutrino oscillations in the case of Dirac neutrinos. What happens if neutrinos have a Majorana mass term rather than the Dirac one? Eq. (2.12) now has to be modified: the term $(m_D)_{ab}\,\overline{\nu}'_{aL}\nu'_{bR} + h.c.$ has to be replaced by $(m_M)_{ab}\,\overline{\nu^c_{aL}}'\,\nu'_{bR} + h.c. = (m_M)_{ab}\,\nu'^T_{aL}\,C\,\nu'_{bR} + h.c.$ This mass term breaks not only the individual lepton flavours but also the total lepton number. The symmetric Majorana mass matrix $(m_M)_{ab}$ is diagonalized by the transformation $U_L^T\, m_M\, U_L = (m_M)_{diag}$, so one can again use the field transformations (2.13). Therefore the structure of the charged current interactions is the same as in the case of the Dirac neutrinos, and the diagonalization of the neutrino mass matrix in the case of the n fermion generations again gives n mass eigenstates. Thus the oscillation probabilities in the case of the Majorana mass term are the same as in the case of the Dirac mass term. This, in particular, means that one cannot distinguish between Dirac and Majorana neutrinos by studying neutrino oscillations. Essentially, this is because the total lepton number is not violated by the neutrino flavour oscillations.

The situation is different in the case when the neutrino mass term is of the most general Dirac + Majorana (D + M) form (which, like in the pure Dirac case, requires the existence of the electroweak singlet neutrinos ν_R). In particular, in the case of n ν_L and n ν_R species, the neutrino mass matrix has the dimension $2n \times 2n$, leading to $2n$ massive Majorana neutrino states. The total lepton number conservation is violated by the Majorana mass term. Unlike in the pure Dirac and pure Majorana cases, in this D + M case one can have a new type of neutrino oscillations: in addition to the usual flavour oscillations $\nu_a \to \nu_b$, oscillations into "sterile" states, $\nu_a \to \nu^c_b$, can occur. These oscillations violate the total lepton number L. Thus, the D + M case can in principle be distinguished from the pure Dirac and Majorana cases in neutrino oscillations experiments. For more detailed discussion of the D + M case see, e.g., [20].

The only practical way of answering the question whether neutrinos are Dirac or Majorana particles, known at the moment, is to look for the neutrinoless double beta decay

$$A(Z,N) \to A(Z \pm 2, N \mp 2) + 2e^{\mp} \,. \tag{2.20}$$

This process can only occur if neutrinos are Majorana particles. If $2\beta 0\nu$ decay is mediated by the standard weak interactions, the amplitude of the process is proportional to the effective neutrino mass

$$A(2\beta 0\nu) \propto \sum_i U_{ei}^2 \, m_i \equiv \langle m_{\nu_e} \rangle_{eff} \,, \tag{2.21}$$

where U_{ai} is the lepton mixing matrix. Neutrinoless double beta decay was searched for experimentally but up to now have not been discovered. The experiments allowed to put upper bounds on the effective Majorana neutrino mass, the best limit coming from the Heidelberg – Moscow experiment on 2β decay of ^{76}Ge [21]:

$$\langle m_{\nu_e} \rangle_{eff} < 0.2 - 0.6 \text{ eV} \,, \tag{2.22}$$

depending on the value of the nuclear matrix element which is not precisely known. If the $2\beta 0\nu$ decay is discovered, it will be possible to infer the value of the effective Majorana neutrino mass $\langle m_{\nu_e} \rangle_{eff}$. As follows from (2.21), this would give the lower limit on the mass of the heaviest neutrino. For a recent review of 2β decay experiments, see [22].

2.2.1 2 flavour case

Let us now consider neutrino oscillations in a simple case of just two neutrino species, ν_e and ν_μ. The lepton mixing matrix U can be written as

$$U = \begin{pmatrix} c & s \\ -s & c \end{pmatrix} , \tag{2.23}$$

where $c = \cos\theta_0$, $s = \sin\theta_0$, θ_0 being the mixing angle. The neutrino mass and flavour eigenstates are therefore related through

$$\begin{aligned} |\nu_e\rangle &= c\,|\nu_1\rangle + s\,|\nu_2\rangle \,, \\ |\nu_\mu\rangle &= -s\,|\nu_1\rangle + c\,|\nu_2\rangle \,. \end{aligned} \tag{2.24}$$

Substituting (2.23) into (2.19) and taking into account that for relativistic neutrinos of the momentum p,

$$E_i = \sqrt{p^2 + m_i^2} \simeq p + \frac{m_i^2}{2p} \simeq p + \frac{m_i^2}{2E} \,, \tag{2.25}$$

we find the transition probabilities

$$P(\nu_e \to \nu_\mu;\, t) = P(\nu_\mu \to \nu_e;\, t) = \sin^2 2\theta_0 \, \sin^2\left(\frac{\Delta m^2}{4E} t\right) . \tag{2.26}$$

Here $\Delta m^2 = m_2^2 - m_1^2$. The survival probabilities are $P(\nu_e \to \nu_e;\, t) = P(\nu_\mu \to \nu_\mu;\, t) = 1 - P(\nu_e \to \nu_e;\, t)$. It is convenient to rewrite the transition probability in terms of the distance L travelled by neutrinos. For relativistic neutrinos $L \simeq t$, and one has

$$P(\nu_e \to \nu_\mu;\, L) = \sin^2 2\theta_0 \, \sin^2\left(\pi \frac{L}{l_{osc}}\right) , \tag{2.27}$$

where l_{osc} is the oscillation length defined as

$$l_{osc} = \frac{4\pi E}{\Delta m^2} \simeq 2.48\ m\, \frac{E\,(\mathrm{MeV})}{\Delta m^2\,(\mathrm{eV}^2)} = 2.48\ km\, \frac{E\,(\mathrm{GeV})}{\Delta m^2\,(\mathrm{eV}^2)} \tag{2.28}$$

It is equal to the distance between any two closest minima or maxima of the transition probability (see fig. 2.3). Notice that l_{osc} is inversely proportional to the energy difference of the neutrino mass eigenstates: $l_{osc} = 2\pi/(E_2 - E_1)$. Another convenient form of the expression for the transition probability is

$$P(\nu_e \to \nu_\mu;\ L) = \sin^2 2\theta_0\ \sin^2\left(1.27\Delta m^2 \frac{L}{E}\right)\ , \tag{2.29}$$

where L is in m and E in MeV or L is in km and E in GeV.

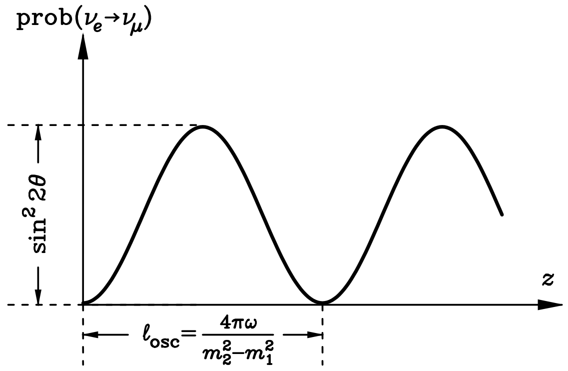

Figure 2.3: Pattern of two–flavour neutrino oscillations (neutrino energy ω, distance z). From [23].

Let us discuss the probability of neutrino oscillations (2.27) (see fig. 2.3). It has two factors. The first one ($\sin^2 2\theta_0$) does not depend on the distance travelled by neutrinos; it describes the amplitude (or depth) of the neutrino oscillations. The amplitude is maximal (equal to one) when the mixing angle $\theta_0 = 45°$, which corresponds to maximal mixing. When θ_0 is close to zero or $90°$, flavour eigenstates are nearly aligned with mass eigenstates, which corresponds to small mixing. In this case the oscillation amplitude is small. The second factor oscillates with time or distance L travelled by neutrinos. The phase of the sine (the oscillation phase) is proportional to the energy difference of the mass eigenstates $\Delta m^2/2E$ and to the distance L. In order to have an appreciable transition probability, it is not enough to have large mixing: in addition, the oscillation phase should be not too small. When the oscillation phase is very large, the transition probability undergoes fast oscillations. Averaging over small energy intervals corresponding to the finite energy resolution of the detector, or over small variations of the distance between the neutrino production and detection points corresponding to the finite sizes of the neutrino source and detector, results then in averaging out the neutrino oscillations. The observed transition probability in this case is

$$\overline{P(\nu_e \to \nu_\mu)} = \overline{P(\nu_\mu \to \nu_e)} = \frac{1}{2}\sin^2 2\theta_0\,. \tag{2.30}$$

In our discussion we have been assuming that the initially produced neutrino state has a certain momentum. Since it is a mixture of different mass eigenstates, its energy is not well defined in this case. We then consider the time evolution of the neutrino state. Alternatively, one could assume that the neutrino is produced in a state of a certain energy but not well defined momentum, and consider the evolution of the neutrino system in space. For relativistic neutrinos the result will be the same. Which description is more correct? Does the initially produced state have a certain energy or a certain momentum? In general, since the production process takes finite time and is localized in space, neither neutrino energy nor momentum is well defined; moreover, the transition probability depends on both the neutrino production and detection processes. Fortunately, for relativistic neutrinos these subtleties are unimportant, and the simple description in terms of the states with certain momentum or energy gives the correct answer [1].

2.2.2 3 flavour case

Consider now the case of three neutrino flavours. The neutrino flavour eigenstate and mass eigenstate fields are related through

$$\begin{pmatrix} \nu_{eL} \\ \nu_{\mu L} \\ \nu_{\tau L} \end{pmatrix} = \begin{pmatrix} U_{e1} & U_{e2} & U_{e3} \\ U_{\mu 1} & U_{\mu 2} & U_{\mu 3} \\ U_{\tau 1} & U_{\tau 2} & U_{\tau 3} \end{pmatrix} \begin{pmatrix} \nu_{1L} \\ \nu_{2L} \\ \nu_{3L} \end{pmatrix} . \tag{2.31}$$

In general, in the case of Dirac neutrinos the lepton mixing matrix U in (2.31) depends on three mixing angles θ_{12}, θ_{13} and θ_{23} and one CP-violating phase δ (in the case of Majorana neutrinos there are two additional, so-called Majorana phases, see discussions in sections 2.2.3). It is convenient to use the parametrization of the matrix U which coincides with the standard parametrization of the quark mixing matrix [16]:

$$U = \begin{pmatrix} c_{12}\, c_{13} & s_{12}\, c_{13} & s_{13}\, e^{-i\delta} \\ -s_{12}\, c_{23} - c_{12}\, s_{23}\, s_{13}\, e^{i\delta} & c_{12}\, c_{23} - s_{12}\, s_{23}\, s_{13}\, e^{i\delta} & s_{23}\, c_{13} \\ s_{12}\, s_{23} - c_{12}\, c_{23}\, s_{13}\, e^{i\delta} & -c_{12}\, s_{23} - s_{12}\, c_{23}\, s_{13}\, e^{i\delta} & c_{23}\, c_{13} \end{pmatrix} . \tag{2.32}$$

Here $c_{ij} = \cos\theta_{ij}$, $s_{ij} = \sin\theta_{ij}$. The probabilities of oscillations between various flavour states are given by the general expression (2.19). Unlike in the two-flavour case, they in general do not have a simple form. There are, however, several practically important limiting cases in which one can obtain very simple approximate expressions for the oscillation probabilities in terms of the 2-flavour ones. Assume first that the neutrino mass squared differences $\Delta m_{ij}^2 = m_i^2 - m_j^2$ have a hierarchy

$$|\Delta m_{21}^2| \ll |\Delta m_{31}^2| \simeq |\Delta m_{32}^2| . \tag{2.33}$$

This means that either $m_1 \ll (\leq)\, m_2 \ll m_3$ (direct hierarchy) or $m_3 \ll m_1 \approx m_2$ (inverted mass hierarchy). These cases are of practical interest since the solar neutrino data indicate that one needs a small mass squared difference $\Delta m_{\odot}^2 \sim 10^{-5}$ eV^2 for the solution of the solar neutrino problem through the matter-enhanced neutrino oscillations (or $\Delta m_{\odot}^2 \sim 10^{-10}$ eV^2 for the vacuum oscillations solution) whereas the explanation of the atmospheric neutrino experiments

[1] Uncertainties of neutrino energy and momentum may be important for the question of coherence of the neutrino state in the case of the oscillations over very long baselines L, e.g. for oscillations of solar or supernova neutrinos on their way to the earth. For discussion see, e.g., [24].

through the neutrino oscillations requires $\Delta m^2_{atm} \sim 10^{-3}$ eV^2, much larger than $\Delta m^2_{\odot}$. Consider first the oscillations over the baselines L for which

$$\frac{\Delta m^2_{21}}{2E} L \ll 1\,. \tag{2.34}$$

This case is relevant for atmospheric, reactor and accelerator neutrino experiments. It follows from (2.34) that the oscillations due to the small mass difference Δm^2_{21} are effectively frozen in this case, and one can consider the limit $\Delta m^2_{21} \to 0$. The probability of $\nu_a \to \nu_b$ oscillations then takes a very simple form:

$$P(\nu_a \to \nu_b;\, L) = 4|U_{a3}|^2\,|U_{b3}|^2\,\sin^2\left(\frac{\Delta m^2_{31}}{4E}\,L\right)\,. \tag{2.35}$$

It resembles the 2-flavour oscillation probability. The probabilities of oscillations between ν_e, ν_μ and ν_τ are

$$P(\nu_e \to \nu_\mu;\, L) = 4|U_{e3}|^2\,|U_{\mu 3}|^2\,\sin^2\left(\frac{\Delta m^2_{31}}{4E}\,L\right) = s^2_{23}\,\sin^2 2\theta_{13}\,\sin^2\left(\frac{\Delta m^2_{31}}{4E}\,L\right)\,, \tag{2.36}$$

$$P(\nu_e \to \nu_\tau;\, L) = 4|U_{e3}|^2\,|U_{\tau 3}|^2\,\sin^2\left(\frac{\Delta m^2_{31}}{4E}\,L\right) = c^2_{23}\,\sin^2 2\theta_{13}\,\sin^2\left(\frac{\Delta m^2_{31}}{4E}\,L\right)\,, \tag{2.37}$$

$$P(\nu_\mu \to \nu_\tau;\, L) = 4|U_{\mu 3}|^2\,|U_{\tau 3}|^2\,\sin^2\left(\frac{\Delta m^2_{31}}{4E}\,L\right) = c^4_{13}\,\sin^2 2\theta_{23}\,\sin^2\left(\frac{\Delta m^2_{31}}{4E}\,L\right)\,, \tag{2.38}$$

with $P(\nu_b \to \nu_a;\, L) = P(\nu_a \to \nu_b;\, L)$. They depend only on the elements of the third column of the lepton mixing matrix U and one mass squared difference. The survival probability for electron neutrinos takes a particularly simple form

$$P(\nu_e \to \nu_e;\, L) = 1 - \sin^2 2\theta_{13}\,\sin^2\left(\frac{\Delta m^2_{31}}{4E}\,L\right)\,, \tag{2.39}$$

i.e. it coincides with the ν_e survival probability in the 2-flavour case with the mass squared difference $\Delta m^2 = \Delta m^2_{31}$ and mixing angle $\theta_0 = \theta_{13}$.

Consider now another limiting case, which is relevant for the solar neutrino oscillations and also for very long baseline reactor experiments (such as KamLAND, see sec. 3.2). We shall be again assuming the hierarchy (2.33) and in addition

$$\frac{\Delta m^2_{31}}{2E} L \simeq \frac{\Delta m^2_{32}}{2E} L \gg 1\,. \tag{2.40}$$

whereas the condition (2.34) is no longer necessary. In this case the oscillations due to the mass squared differences Δm_{31} and Δm_{32} are very fast and lead to an averaged effect; the ν_e survival probability is then

$$P(\nu_e \to \nu_e) \simeq c^4_{13} P + s^4_{13}\,, \tag{2.41}$$

where P is the ν_e survival probability in the 2-flavour case with the mass squared difference $\Delta m^2 = \Delta m^2_{21}$ and mixing angle $\theta_0 = \theta_{12}$. In the case of neutrino oscillations in vacuum one has

$$P = 1 - \sin^2 2\theta_{12}\,\sin^2\left(\frac{\Delta m^2_{21}}{4E}\,L\right)\,. \tag{2.42}$$

Finally, consider the limit $U_{e3} = 0$ (the results will be also approximately valid for $|U_{e3}| \ll 1$). In this case one obtains

$$P(\nu_e \to \nu_\mu;\, L) = c_{23}^2 \sin^2 2\theta_{12}\, \sin^2 \Delta_{21}\,, \tag{2.43}$$
$$P(\nu_e \to \nu_\tau;\, L) = s_{23}^2 \sin^2 2\theta_{12}\, \sin^2 \Delta_{21}\,, \tag{2.44}$$
$$P(\nu_\mu \to \nu_\tau;\, L) = \sin^2 2\theta_{23}\, (-s_{12}^2\, c_{12}^2 \sin^2 \Delta_{21} + s_{12}^2\, \sin^2 \Delta_{31} + c_{12}^2 \sin^2 \Delta_{32})\,, \tag{2.45}$$

where $\Delta_{ij} \equiv (\Delta m_{ij}^2/4E)L$, and no assumption about the hierarchy of the mass squared differences has been made. Notice that the limiting cases that we have discussed here are not mutually excluding, i.e. have some overlap with each other.

In general, when considering the propagation of solar neutrinos in the sun or in the earth, one should take into account matter effects on neutrino oscillations. The same is true for the terrestrial atmospheric and long baseline accelerator neutrino oscillation experiments in which the neutrino trajectories or their significant portions go through the matter of the earth. Matter effects on $\nu_\mu \leftrightarrow \nu_\tau$ oscillations are relatively small (they vanish in the 2-flavour approximation), but they may be quite appreciable for $\nu_e \leftrightarrow \nu_\mu$ and $\nu_e \leftrightarrow \nu_\tau$ oscillations. We shall discuss these effects in sec. 2.3. As we shall see, eq. (2.41) remains valid in the case of neutrino oscillations in matter as well, but the two-flavour probability (2.42) has to be modified. Eqs. (2.36) - (2.38), (2.39) and (2.43) - (2.45) are also modified in the case of neutrino oscillations in matter.

2.2.3 Implications of CP, T and CPT symmetries

We shall now consider the consequences of CP, T and CPT symmetries for neutrino oscillations. Charge conjugation operation C is not well defined for neutrinos as it would convert a left handed neutrino into a non-existent left handed antineutrino. CP, however, is well defined: it converts a left handed neutrino ν_L into a right handed antineutrino which is the antiparticle of ν_L. Thus, CP essentially acts as the particle - antiparticle conjugation. If CP is conserved, the probabilities of oscillations between particles and their antiparticles coincide:

$$\text{CP}: \qquad P(\nu_a \to \nu_b;\, t) = P(\bar\nu_a \to \bar\nu_b;\, t)\,. \tag{2.46}$$

In quantum field theory, the same field operator that annihilates a particle also creates its antiparticle, whereas its Hermitean conjugate does the opposite. Therefore the action of the particle – antiparticle conjugation on the lepton mixing matrix U amounts to $U \to U^*$. This means that CP is only conserved in the leptonic sector if the mixing matrix U is real or can be made real by a rephasing of the lepton fields.

In general, a unitary $n \times n$ matrix depends on $n(n-1)/2$ angles and $n(n+1)/2$ phases. In the Dirac case, $2n-1$ phases can be removed by a proper rephasing of the left handed fields, leaving $n(n+1)/2 - (2n-1) = (n-1)(n-2)/2$ physical phases (the rephasing of the left handed field leaves the lepton mass terms unchanged since the phases can be absorbed into the corresponding rephasing of the right-handed fields). Thus, in the Dirac case CP non-conservation is only possible in the case of $n \geq 3$ generations. In the Majorana case there is less freedom to rephase the fields since the Majorana mass terms are of the form $\nu_L \nu_L + h.c.$ rather than of the form $\bar\nu_R \nu_L + h.c.$ and so the phases of neutrino fields cannot be absorbed. Therefore in the Majorana case only n phases can be removed, leaving $n(n+1)/2 - n = n(n-1)/2$ physical phases.

Out of these phases, $(n-1)(n-2)/2$ are the usual, Dirac-type phases while the remaining $n-1$ are specific for the Majorana case, so called Majorana phases. Majorana phases do not lead to any observable effects for neutrino oscillations [25], and we shall not consider them here.

CPT transformation can be considered as a combined action of CP, which results in the interchange between paricles and antiparticles, and time reversal, which interchanges the initial and final states. Therefore under CPT transformation the oscillation probability $P(\nu_a \to \nu_b;\, t)$ goes into $P(\bar{\nu}_b \to \bar{\nu}_a;\, t)$. One the other hand, from eq. (2.18) it follows that the CPT transformation $U \to U^*$, $t \to -t$ transforms the oscillation amplitude $A(\nu_a \to \nu_b;\, t)$ into its complex conjugate. Therefore the oscillation probabilities are invariant with respect to CPT, i.e. the following equality holds:

$$\text{CPT}: \qquad P(\nu_a \to \nu_b;\, t) = P(\bar{\nu}_b \to \bar{\nu}_a;\, t)\,. \tag{2.47}$$

CPT invariance implies, in particular, that the survival probabilities for neutrinos and antineutrinos are the same: $P(\nu_a \to \nu_a;\, t) = P(\bar{\nu}_a \to \bar{\nu}_a;\, t)$.

Finally, time reversal T interchanges the initial and final states, so if T is conserved one has

$$\text{T}: \qquad P(\nu_a \to \nu_b;\, t) = P(\nu_b \to \nu_a;\, t)\,. \tag{2.48}$$

From CPT invariance it follows that CP conservation is equivalent to T conservation; indeed, it is easy to see that (2.46) and (2.47) lead to (2.48).

Let us now consider effects of CP-violation on neutrino oscillations. If CP is not conserved, the oscillation probabilities for neutrinos are different from those for antineutrinos. As we pointed out before, this is only possible if the lepton mixing matrix U is essentially complex, i.e. has unremovable phases. For three lepton generations, there is only one such phase δ, and so there should be only one CP-odd oscillation asymmetry. Let us denote the CP-odd asymmetries as

$$\Delta P_{ab} \equiv P(\nu_a \to \nu_b;\, t) - P(\bar{\nu}_a \to \bar{\nu}_b;\, t)\,. \tag{2.49}$$

From CPT invariance one finds $\Delta P_{ab} = -\Delta P_{ba}$. Using the parametrization (2.32) of the mixing matrix U it is not difficult to find

$$\begin{aligned}\Delta P_{e\mu} = \Delta P_{\mu\tau} = \Delta P_{\tau e} = 4 s_{12}\, c_{12}\, s_{13}\, c_{13}^2\, s_{23}\, c_{23}\, \sin\delta \qquad\qquad \\ \times \left[\sin\left(\frac{\Delta m_{12}^2}{2E}t\right) + \sin\left(\frac{\Delta m_{23}^2}{2E}t\right) + \sin\left(\frac{\Delta m_{31}^2}{2E}t\right)\right]\,.\end{aligned} \tag{2.50}$$

This expression has several interesting features. First, as expected, it vanishes in the limit $\delta = 0$. Second, it vanishes if any of the mixing angles θ_{12}, θ_{13} or θ_{23} is zero or 90°. In particular, oscillation probabilities (2.43)-(2.45) obtained in the limit $\theta_{13} = 0$ are CP-symmetric. Third, since the mass squared differences satisfy the relation $\Delta m_{12}^2 + \Delta m_{23}^2 + \Delta m_{31}^2 = 0$, the CP-odd asymmetry (2.50) vanishes if even one of Δm_{ij}^2 is zero. We have already encountered this situation – the transition probabilities (2.35) - (2.39). derived in the limit $\Delta m_{21}^2 = 0$ depend only on the absolute values of U_{ai} and are therefore CP-invariant. The relation between Δm_{ij}^2 also means that in the limit of the small arguments of the sines (small oscillation phases) in eq. (2.50) the probability asymmetry is cubic (more precisely, tri-linear) in small phases rather than linear. Another important difference between the usual oscillation probabilities and the CP-odd asymmetry (2.50) is that while the former contain squared sines of the oscillation phases and therefore oscillate near non-zero average values, the latter is linear in these sines and so oscillates around zero. This means that in the case of very large oscillation phases, when the averaging regime sets in, the CP-odd asymmetry of neutrino oscillations averages to zero. It is for this reason that the oscillation probability (2.41) is CP-invariant.

It follows from the above discussion that the experimental observation of CP violation effect in neutrino oscillations is a very difficult task. The CP-odd probability asymmetry is suppressed if any one of the three lepton mixing angles is small, and we know from the CHOOZ reactor neutrino experiment that the mixing angle θ_{13} is small (see sec. 3.2 below for a discussion of the reactor and accelerator data). The atmospheric neutrino experiments indicate that the mixing angle θ_{23} is rather large, but the value of θ_{12} is largely unknown: the present solar neutrino data allow both large and small values for this mixing angle. The hierarchy (2.33) of the mass squared differences which follows from the solar and atmospheric neutrino observations further hinders experimental searches of CP violation in the neutrino oscillation experiments. In addition, matter effects on neutrino oscillations may mimic CP violation and so make the searches of the genuine CP violation even more difficult. Still, the presently allowed values of neutrino parameters do not exclude a possibility of observation of CP violation effects in the future neutrino experiments. Discovering CP-nonconservation in the leptonic sector would be of great importance, so the goal is worth pursuing.

2.3 Neutrino oscillations in matter

Neutrino oscillations in matter may differ from the oscillations in vacuum in a very significant way. The most striking manifestation of the matter effects on neutrino oscillations is the resonance enhancement of the oscillation probability – the Mikheyev - Smirnov - Wolfenstein (MSW) effect [26, 27]. In vacuum, the oscillation probability cannot exceed $\sin^2 2\theta_0$, and for small mixing angles it is always small. Matter can enhance neutrino mixing, and the probabilities of neutrino oscillations in matter can be large (close to unity) even if the mixing angle in vacuum is very small. Matter enhanced neutrino oscillations provide a very elegant solution of the solar neutrino problem; matter effects on oscillations of solar and atmospheric neutrinos inside the earth can be quite important. Neutrino oscillations in supernovae and in the early universe may also be strongly affected by matter.

How does the matter affect neutrino propagation? Neutrinos can be absorbed by the matter constituents, or scattered off them, changing their momentum and energy. However the probabilities of these processes, being proportional to the square of the Fermi constant G_F, are typically very small. Neutrinos can also experience forward scattering, an elastic scattering in which their momentum is not changed. This process is coherent, and it creates mean potentials V_a for neutrinos which are proportional to the number densities of the scatterers. These potentials are of the first order in G_F, but one could still expect them to be too small and of no practical interest. This expectation, however, would be wrong. To assess the importance of matter effects on neutrino oscillations, one has to compare the matter-induced potentials of neutrinos V_a with the characteristic neutrino kinetic energy differences $\Delta m^2/2E$. Although the potentials V_a are typically very small, so are $\Delta m^2/2E$; if V_a are comparable to or larger than

$\Delta m^2/2E$, matter can strongly affect neutrino oscillations.

2.3.1 Evolution equation

We shall now consider neutrino oscillations in matter in some detail. Neutrinos of all three flavours – ν_e, ν_μ and ν_τ – interact with the electrons, protons and neutrons of matter through neutral current (NC) interaction mediated by Z^0 bosons. Electron neutrinos in addition have charged current (CC) interactions with the electrons of the medium, which are mediated by the $W^\pm$ exchange (see fig. 2.4).

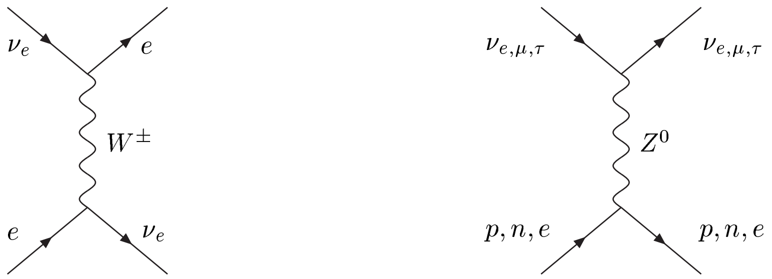

Figure 2.4: Neutrino scattering diagrams

Let us consider the CC interactions. At low neutrino energies, they are described by the effective Hamiltonian

$$H_{CC} = \frac{G_F}{\sqrt{2}}\,[\bar{e}\gamma_\mu(1-\gamma_5)\nu_e][\bar{\nu}_e\gamma^\mu(1-\gamma_5)e] = \frac{G_F}{\sqrt{2}}\,[\bar{e}\gamma_\mu(1-\gamma_5)e][\bar{\nu}_e\gamma^\mu(1-\gamma_5)\nu_e]\,, \tag{2.51}$$

where we have used the Fierz transformation. In order to obtain the coherent forward scattering contribution to the energy of ν_e in matter (i.e. the matter-induced potential for ν_e) we fix the variables corresponding to ν_e and integrate over all the variables that correspond to the electron:

$$H_{eff}(\nu_e) = \langle H_{CC}\rangle_{electron} \equiv \bar{\nu}_e V_e \nu_e\,. \tag{2.52}$$

Furthermore, we have

$$\langle\bar{e}\gamma_0 e\rangle = \langle e^\dagger e\rangle = N_e\,, \qquad \langle\bar{e}\boldsymbol{\gamma}e\rangle = \langle\mathbf{v}_e\rangle\,, \quad \langle\bar{e}\gamma_0\gamma_5 e\rangle = \langle\frac{\boldsymbol{\sigma}_e\mathbf{p}_e}{E_e}\rangle\,, \quad \langle\bar{e}\boldsymbol{\gamma}\gamma_5 e\rangle = \langle\boldsymbol{\sigma}_e\rangle\,, \tag{2.53}$$

where N_e is the electron number density. For unpolarized medium of zero total momentum only the first term survives, and we obtain

$$(V_e)_{CC} \equiv V_{CC} = \sqrt{2}\,G_F N_e\,. \tag{2.54}$$

Analogously, one can find the NC contributions V_{NC} to the matter-induced neutrino potentials. Since NC interaction are flavour independent, these contributions are the same for neutrinos of all three flavours. In an electrically neutral medium, the number densities of protons and electrons coincide, and the corresponding contributions to V_{NC} cancel. The direct calculation of the contribution due to the NC scattering of neutrinos off neutrons gives $(V_a)_{NC} = -G_F N_n/\sqrt{2}$, where N_n is the neutron number density. Together with eq. (2.54) this gives

$$V_e = \sqrt{2}\,G_F\left(N_e - \frac{N_n}{2}\right)\,, \qquad V_\mu = V_\tau = \sqrt{2}\,G_F\left(-\frac{N_n}{2}\right)\,. \tag{2.55}$$

For antineutrinos, one has to replace $V_a \to -V_a$.

Let us now consider the evolution of a system of oscillating neutrinos in matter. In vacuum, the evolution is most easily followed in the mass eigenstate basis. In matter it is more convenient to do that in the flavour basis because the effective potentials of neutrinos are diagonal in this basis. Consider first the two-flavour case. As usual, we write $\nu_{fl} = U\nu_m$ where ν_{fl} and ν_m are two-component vectors of neutrino fields in the flavour and mass eigenstate bases and the matrix U is given by eq. (2.23). In the absence of matter, the evolution equation in the mass eigenstate basis is $i(d/dt)|\nu_m\rangle = H_m|\nu_m\rangle$, where $H_m = diag(E_1, E_2)$. This gives the evolution equation in the flavour basis: $i(d/dt)|\nu_{fl}\rangle = H_{fl}|\nu_{fl}\rangle = UH_mU^\dagger|\nu_{fl}\rangle$. For relativistic neutrinos $E_i \simeq p + m_i^2/2E$, and we thus obtain

$$i\frac{d}{dt}\begin{pmatrix} \nu_e \\ \nu_\mu \end{pmatrix} = \begin{pmatrix} \left(p + \frac{m_1^2+m_2^2}{4E}\right) - \frac{\Delta m^2}{4E}\cos 2\theta_0 & \frac{\Delta m^2}{4E}\sin 2\theta_0 \\ \frac{\Delta m^2}{4E}\sin 2\theta_0 & \left(p + \frac{m_1^2+m_2^2}{4E}\right) + \frac{\Delta m^2}{4E}\cos 2\theta_0 \end{pmatrix}\begin{pmatrix} \nu_e \\ \nu_\mu \end{pmatrix}. \quad (2.56)$$

Here ν_e and ν_μ stand for time dependent amplitudes of finding the electron and muon neutrino respectively. The expressions in the brackets in the diagonal elements of the effective Hamiltonian in eq. (2.56) coincide. They can only modify the common phase of the neutrino states and therefore have no effect on neutrino oscillations which depend on the phase differences. For this reason one can omit these terms. The evolution equation describing neutrino oscillations in vacuum in the flavour basis then takes the form

$$i\frac{d}{dt}\begin{pmatrix} \nu_e \\ \nu_\mu \end{pmatrix} = \begin{pmatrix} -\frac{\Delta m^2}{4E}\cos 2\theta_0 & \frac{\Delta m^2}{4E}\sin 2\theta_0 \\ \frac{\Delta m^2}{4E}\sin 2\theta_0 & \frac{\Delta m^2}{4E}\cos 2\theta_0 \end{pmatrix}\begin{pmatrix} \nu_e \\ \nu_\mu \end{pmatrix}. \quad (2.57)$$

We now proceed to derive the neutrino evolution equation in matter. To do that, one has to add the matter-induced potentials V_e and V_μ to the diagonal elements of the effective Hamiltonian H_{fl} in eq. (2.57). Notice that V_e and V_μ contain a common term due to NC interactions. As we already know, such common terms in the diagonal elements are of no consequence for neutrino oscillations; we can therefore omit them [2]. This gives

$$i\frac{d}{dt}\begin{pmatrix} \nu_e \\ \nu_\mu \end{pmatrix} = \begin{pmatrix} -\frac{\Delta m^2}{4E}\cos 2\theta_0 + \sqrt{2}\,G_F N_e & \frac{\Delta m^2}{4E}\sin 2\theta_0 \\ \frac{\Delta m^2}{4E}\sin 2\theta_0 & \frac{\Delta m^2}{4E}\cos 2\theta_0 \end{pmatrix}\begin{pmatrix} \nu_e \\ \nu_\mu \end{pmatrix}. \quad (2.58)$$

This is the evolution equation which describes $\nu_e \leftrightarrow \nu_\mu$ oscillations in matter. The equation for $\nu_e \leftrightarrow \nu_\tau$ oscillations has the same form. In the two-flavour approximation, $\nu_\mu \leftrightarrow \nu_\tau$ oscillations are not modified in matter since $V_\mu = V_\tau$; however, in the full 3-flavour framework matter does influence the $\nu_\mu \leftrightarrow \nu_\tau$ oscillations because of the mixing with ν_e.

2.3.2 Constant density case

Let us now consider the evolution equation (2.58). In general, the electron number density N_e depends on the coordinate along the neutrino trajectory or, in our description in eq. (2.58), on t. We shall first consider a simple case of constant matter density and chemical composition, i.e.

[2] The NC contribution does, however, affect the oscillations between the usual and "sterile" (electroweak singlet) neutrinos in matter.

$N_e = const$. Diagonalization of the effective Hamiltonian in (2.58) gives the following neutrino eigenstates in matter:

$$\begin{aligned} \nu_A &= \nu_e \cos\theta + \nu_\mu \sin\theta\,, \\ \nu_B &= -\nu_e \sin\theta + \nu_\mu \cos\theta\,, \end{aligned} \tag{2.59}$$

where the mixing angle θ is given by

$$\tan 2\theta = \frac{\frac{\Delta m^2}{2E}\sin 2\theta_0}{\frac{\Delta m^2}{2E}\cos 2\theta_0 - \sqrt{2}\,G_F\,N_e}\,. \tag{2.60}$$

It is different from the vacuum mixing angle θ_0 and therefore the matter eigenstates ν_A and ν_B do not coincide with mass eigenstates ν_1 and ν_2. The difference of neutrino eigenenergies in matter is

$$E_A - E_B = \sqrt{\left(\frac{\Delta m^2}{2E}\cos 2\theta_0 - \sqrt{2}\,G_F\,N_e\right)^2 + \left(\frac{\Delta m^2}{2E}\right)^2 \sin^2 2\theta_0}\,. \tag{2.61}$$

It is now easy to find the probability of $\nu_e \leftrightarrow \nu_\mu$ oscillations in matter:

$$P(\nu_e \to \nu_\mu;\, L) = \sin^2 2\theta\, \sin^2\left(\pi \frac{L}{l_m}\right)\,, \tag{2.62}$$

where

$$l_m = \frac{2\pi}{E_A - E_B} = \frac{2\pi}{\sqrt{\left(\frac{\Delta m^2}{2E}\cos 2\theta_0 - \sqrt{2}\,G_F\,N_e\right)^2 + \left(\frac{\Delta m^2}{2E}\right)^2 \sin^2 2\theta_0}}\,. \tag{2.63}$$

It has exactly the same form as the probability of oscillations in vacuum (2.27), except that the vacuum mixing angle θ_0 and oscillation length l_{osc} are replaced by those in matter, θ and l_m. In the limit of zero matter density $\theta = \theta_0$, $l_m = l_{osc}$, and the vacuum oscillation probability is recovered.

The oscillation amplitude

$$\sin^2 2\theta = \frac{\left(\frac{\Delta m^2}{2E}\right)^2 \sin^2 2\theta_0}{\left(\frac{\Delta m^2}{2E}\cos 2\theta_0 - \sqrt{2}\,G_F\,N_e\right)^2 + \left(\frac{\Delta m^2}{2E}\right)^2 \sin^2 2\theta_0} \tag{2.64}$$

has a typical resonance form, with the maximum value $\sin^2 2\theta = 1$ achieved when the condition

$$\sqrt{2}\,G_F\,N_e = \frac{\Delta m^2}{2E}\cos 2\theta_0 \tag{2.65}$$

is satisfied. It is called the MSW resonance condition. From (2.60) or (2.64) it follows that when (2.65) is fulfilled, mixing in matter is maximal ($\theta = 45°$), independently from the vacuum mixing angle θ_0. Thus, the probability of neutrino flavour transition in matter can be large even if the vacuum mixing angle is very small!

For the resonance enhancement of neutrino oscillations in matter to be possible, the r.h.s. of (2.65) must be positive:

$$\Delta m^2 \cos 2\theta_0 = (m_2^2 - m_1^2)(\cos^2\theta_0 - \sin^2\theta_0) > 0\,, \tag{2.66}$$

i.e. if ν_2 is heavier than ν_1, one needs $\cos^2\theta_0 > \sin^2\theta_0$, and vice versa. It follows from eq. (2.24) that the condition (2.66) is equivalent to the requirement that of the two mass eigenstates

ν_1 and ν_2, the lower-mass one have a larger ν_e component. If one chooses the convention $\cos 2\theta_0 > 0$, (as is usually done) then (2.66) reduces to $\Delta m^2 \equiv \Delta m_{21}^2 > 0$. The resonance condition for antineutrinos is then $\Delta m^2 < 0$. Therefore, for a given sign of Δm^2, either neutrinos or antineutrinos (but not both) can experience the resonantly enhanced oscillations in matter.

Chapter 3

Status of neutrino oscillation studies

3.1 The solar neutrino problem

The first experiment in which the solar neutrinos have been observed was the Homestake experiment of Davis and his collaborators. It is based on the reaction

$$\nu_e + {}^{37}\mathrm{Cl} \to {}^{37}\mathrm{Ar} + e^- \,. \tag{3.1}$$

The energy threshold of reaction (3.1) is 0.814 MeV, so only the ^{8}B and ^{7}Be and *pep* neutrinos are detected in the Homestake experiment (see fig. 3.1), the largest contribution coming from the ^{8}B neutrinos. The two gallium solar neutrino experiments, SAGE and Gallex, employ the reaction

$$\nu_e + {}^{71}\mathrm{Ga} \to {}^{71}\mathrm{Ge} + e^- \,. \tag{3.2}$$

The energy threshold of this reaction is 0.233 MeV, and so the gallium experiments can also detect the lowest energy *pp* neutrinos. The next two experiments – Kamiokande and its up-scaled version Super-Kamiokande – are the water Cherenkov detectors and use the neutrino-electron scattering reaction

$$\nu_a + e^- \to \nu_a + e^- \,. \tag{3.3}$$

to detect solar neutrinos. This reaction has zero physical threshold, but one has to introduce energy cuts to suppress the background. In the Kamiokande experiment solar neutrinos with the energies $E > 7.5$ MeV were detected, whereas the threshold used by Super-Kamiokande (SK) in their analysis is at present 5.5 MeV. With these energy cuts, the Kamiokande and SK detection rates are only sensitive to the ^{8}B component of the solar neutrino flux (the highest-energy *hep* neutrinos give a negligible contribution to the total detection rates as their flux is very low).

In all five solar neutrino experiments (Homestake, Gallex, SAGE, Kamio-kande and SK) fewer neutrinos than expected were detected, the degree of deficiency being different in the experiments of different types (see table I). This has been called the solar neutrino problem.

The solar neutrino problem is not just the problem of the deficit of the observed neutrino flux: results of different experiments seem to be inconsistent with each other. In the absence of new neutrino physics, the energy spectra of the various components of the solar neutrino flux are given by the standard nuclear physics and well known, and only the total fluxes of these components may be different from those predicted by the standard solar models. The fluxes inferred from different experiments are not consistent with each other, and in fact the best fit

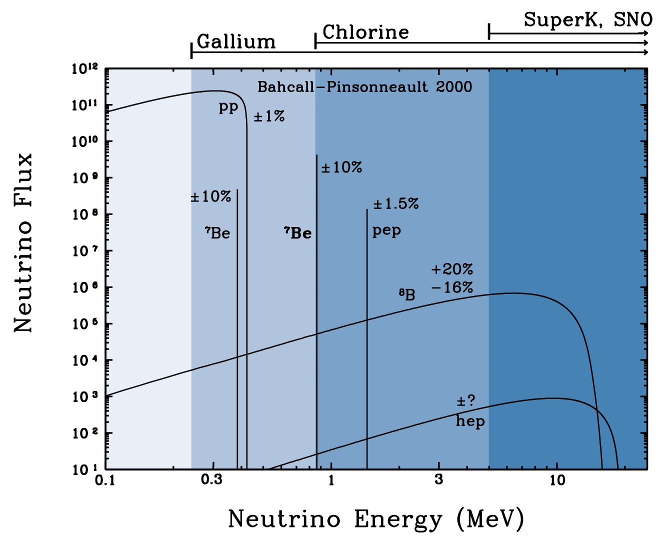

Figure 3.1: Solar neutrino spectrum and estimated theoretical errors of fluxes. The thresholds of solar neutrino experiments are indicated above the figure. From [28].

Table 3.1: Detection rates in five solar neutrino experiments. Units are SNU (1 SNU = 10^{-36} captures per target atom per second) for all the experiments except Kamiokande and SK, for which they are $10^6 cm^{-2} s^{-1}$. From [30].

Experiment	Data	Theory (BP98)	Data/Theory
Homestake	$2.56 \pm 0.16 \pm 0.14$	$7.7\pm^{1.2}_{1.0}$	0.33 ± 0.027
Kamiokande	$2.80 \pm 0.19 \pm 0.33$	$5.15^{+1.0}_{-0.7}$	0.54 ± 0.07
SAGE	$75.4\,^{+7.0}_{-6.8}\,^{+3.5}_{-3.0}$	129^{+8}_{-6}	0.58 ± 0.06
Gallex+GNO	$74.1\,^{+6.7}_{-6.8}$	129^{+8}_{-6}	0.57 ± 0.06
Super-Kamiokande	$2.40 \pm 0.03\,^{+0.08}_{-0.07}$	$5.15^{+1.0}_{-0.7}$	0.465 ± 0.016

value of the the ^{7}Be neutrino flux is negative! One is then led to conclude that neutrinos are not standard.

There are several possible particle-physics solutions of the solar neutrino problem, the most natural one being neutrino oscillations. The neutrino oscillation solution has become even more plausible after the strong evidence for atmospheric neutrino oscillations was reported by the SK Collaboration. Neutrino oscillations can convert a fraction of solar ν_e into ν_μ or ν_τ (or their combination). Since the energy of solar neutrinos is smaller than the masses of muons and tauons, these ν_μ or ν_τ cannot be detected in the CC reactions of the type (3.1) or (3.2) and therefore are invisible in the chlorine and gallium experiments. They can scatter on electrons through the neutral current (NC) interactions and therefore should contribute to the detection rates in water Cherenkov detectors. However, the cross section of the NC channel of reaction (3.3) is about a factor of 6 smaller than that of the CC channel, and so the deficit of the neutrino flux observed in the Kamiokande and SK experiments can be explained. The probabilities of neutrino oscillations depend on neutrino energy, and the distortion of the energy spectrum of the experimentally detected solar neutrinos, which is necessary to reconcile the data of different experiments, is readily obtained.

The oscillations of solar neutrinos inside the sun can be strongly enhanced due to the MSW

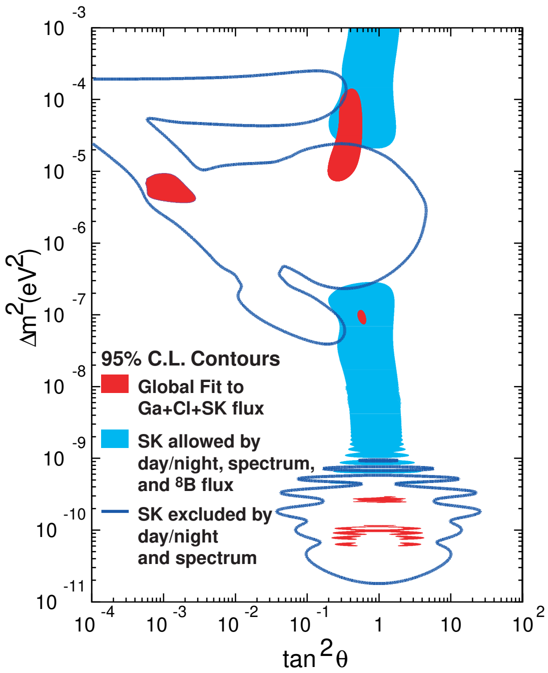

Figure 3.2: Solar neutrino parameter space: the dark areas show the global flux fit solutions. The interiors of the dark lines indicate the SK excluded regions; the light shaded areas indicate the SK allowed regions [31].

effect [26] and the solar data can be fitted even with a very small vacuum mixing angle. Solar matter can also influence neutrino oscillations if the vacuum mixing angle is not small. The allowed values of the neutrino oscillation parameters $\tan^2\theta$ and Δm^2 which fit the detection rates in the chlorine, gallium and water Cherenkov experiments in the 2-flavour scheme are shown in fig. 3.2 for oscillations of ν_e into active neutrinos (dark shaded areas). In the case of the matter enhanced oscillations, there are three allowed ranges of the parameters corresponding to the small mixing angle (SMA), large mixing angle (LMA) and low Δm^2 (LOW) MSW solutions. There is also the vacuum oscillation (VO) solution corresponding to very small values of Δm^2, for which the neutrino oscillation length for typical solar neutrino energies ($\sim$ a few MeV) is comparable to the distance between the sun and the earth. This solution is also known as "just so" oscillation solution. The detection rates in the five solar neutrino experiments can also be explained by $\nu_e \to \nu_s$ oscillations, for which there is only the SMA solution with the allowed region of parameters similar to that for oscillations into active neutrinos [29, 31].

The use of the variable $\tan^2\theta$ instead of the usual $\sin^2 2\theta$ in fig. 3.2 is worth a comment. The probability of 2-flavour neutrino oscillations in vacuum is invariant under the substitutions $\theta \to \pi/2 - \theta$ or $\Delta m^2 \to -\Delta m^2$, but the oscillation probability in matter is not. It is, however, invariant under the combined action of these substitutions. To cover the full parameter space it is sufficient to assume $0 \leq \theta \leq \pi/4$ and allow for both signs of Δm^2, or to assume that Δm^2 is always positive (which can always be achieved by renaming the mass eigenstates $\nu_1 \leftrightarrow \nu_2$) and let θ be in the full domain $[0, \pi/2]$. Usually, the first approach was adopted; however, the solutions of the solar neutrino problem in the region $\Delta m^2 < 0$ have not been studied (except in the 3-neutrino [32] and 4-neutrino [33] frameworks). This was motivated by the fact that there is no MSW enhancement for neutrinos in this region of parameters. However, in [34] it has been emphasized that if one allows for large enough confidence levels, or treats the solar ^{8}B neutrino flux as a free parameter, or leaves the Homestake result out, solutions in this "dark side" of the parameter space exist, provided that the mixing angle is close to the maximal one. It is convenient to assume $\Delta m^2 > 0$ and plot the allowed regions of the parameter space in the plane $(\tan^2\theta,\, \Delta m^2)$ with $0 \le \theta \le \pi/2$; in the conventional approach one would need two separate plots for $\Delta m^2 > 0$ and $\Delta m^2 < 0$.

3.1.1 Day-night effect

Solar neutrinos detected during night travel some distance inside the earth on their way to the detector, and their oscillations can be affected by the matter of the earth. In particular, a fraction of ν_μ or ν_τ produced as a result of the solar ν_e oscillations can be reconverted into ν_e by oscillations enhanced by the matter of the earth. The day/night difference due to the earth "regeneration" effect (and in general the zenith angle dependence of the neutrino signal) can in principle be observed in real-time experiments, such as SK. The day/night effect is expected to be appreciable in the case of the LMA solution, but very small in the case of the SMA solution. For the LOW solution, the day/night effect is expected to be quite sizeable in the low-energy part of the solar neutrino spectrum (in particular, for ^{7}Be neutrinos), but small for the high-energy part detected by SK. There is no day/night effect in the case of the VO solution.

The zenit angle dependence of the solar neutrino signal measured by the SK is shown in fig. 3.3. The value of day/night asymmetry measured in the SK experiment is [29]

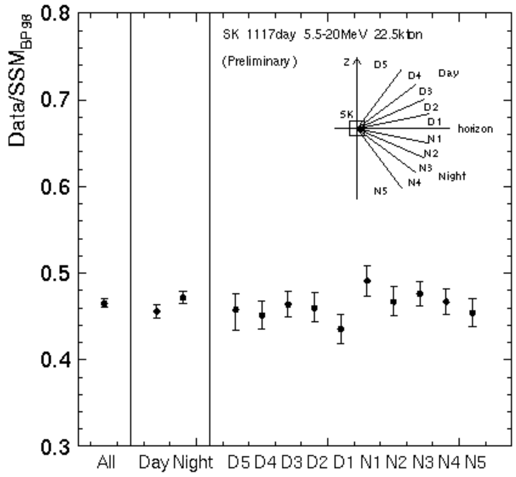

Figure 3.3: Zenith angle dependence of the solar neutrino flux measured by the Super-Kamiokande experiment [31].

$$\frac{D-N}{(D+N)/2} = -0.034 \pm 0.022\,(stat.)^{+0.013}_{-0.012}\,(syst.)\,, \tag{3.4}$$

i.e. shows an excess of the night-time flux at about 1.3σ. This excess, however, is not statistically significant. The smallness of the SK day/night asymmetry results in the exclusion of the lower-

Δm^2 part of the LMA allowed region (see fig. 3.2). This is a good news for future very long baseline accelerator experiments as it improves the prospects of observation of CP violation in neutrino oscillations. The zenith angle event dependence measured by the SK shows a rather flat distribution of the excess of events over different night-time zenith angle bins. This is rather typical for the LMA and LOW solutions (although for LOW solution one can expect some excess of events in the second night bin $N2$ [35]), whereas for the SMA solution one normally expects the excess (or deficiency) to be concentrated in the vertical upward bin with zenith angles θ in the range $-1 < \cos\theta < -0.8$.

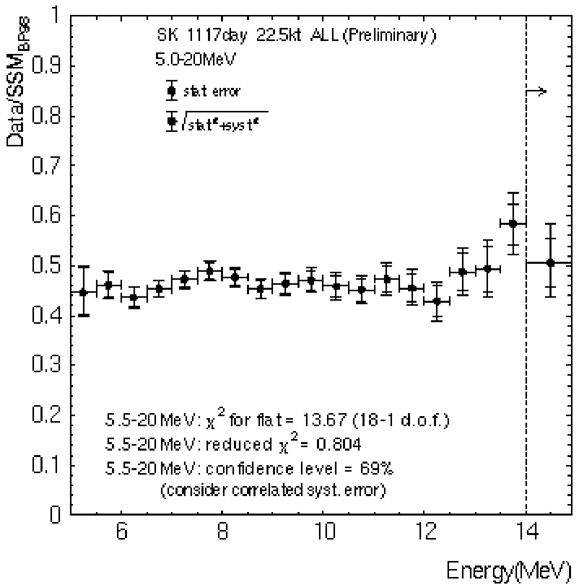

Figure 3.4: Recoil electron energy spectrum in the Super-Kamiokande experiment normalized to the standard solar model prediction. From [31].

3.1.2 Energy spectrum distortion

Neutrino oscillations should result in certain distortions of the spectrum of the detected solar neutrinos, which can be studied by measuring the recoil electron spectrum in the reaction (3.3). This spectrum has been measured in the SK experiment, and the results are shown in fig. (3.4). In the absence of the neutrino spectrum distortion, the ratio measured/expected electron spectrum presented in this figure should be a horizontal line. The measured relative spectrum is rather flat; in particular, the excess of high-energy events seen in the earlier SK data has essentially disappeared. This allowed SK to put an upper limit on the flux of the *hep* neutrinos: $f_{hep} < 13.2 f_{hep}$(BP98), with the best fit value $f_{hep} = (5.4 \pm 4.5) f_{hep}$(BP98), where BP98 stands for the Bahcall-Pinsonneault 98 standard solar model.

The flatness of the SK relative spectrum disfavours the VO solution and the larger-$\sin^2 2\theta$ part of the SMA parameter space; on the other hand the small-$\sin^2 2\theta$ part of the SMA parameter space is disfavoured since it predicts a positive day-night asymmetry while the asymmetry measured by SK is negative (at 1.3σ level). This allowed the SK Collaboration to conclude that at present the VO and SMA solutions are disfavoured at 95% c.l., while the LMA and LOW solutions are favoured (see fig. 3.2). Oscillations into sterile neutrinos are also disfavoured at

95% c.l..

While this result is certainly interesting and shows the directions in which the solar neutrino data seem to lead us, one should clearly understand that in fact the VO and SMA solutions are *not* yet excluded. The solar neutrino data are not fully settled yet, and caution is advised when drawing conclusions. It is worth remembering that just a few years ago the LOW solution, which is now a perfectly respectable one, was disfavoured, and shortly before that it just did not exist. Obviously, more data are needed to clear the situation up.

3.1.3 Future experiments

Fortunately, several new experiments which can potentially resolve the problem are now under way or will be soon put into operation. The SNO (Sudbury Neutrino Observatory) experiment started taking data in 1999, and its first results were reported at the Neutrino 2000 Conference [36]. The SNO detector consists of 1000 tons of heavy water, and is capable of detecting solar neutrinos in three different channels:

$$\nu_e + d \to p + p + e^- \qquad (\mathrm{CC}), \quad E_{min} = 1.44 \text{ MeV}\,, \tag{3.5}$$

$$\nu_a + d \to p + n + \nu_a \qquad (\mathrm{NC}), \quad E_{min} = 2.23 \text{ MeV}\,, \tag{3.6}$$

and $\nu_a e$ scattering process (3.3) which can proceed through both CC and NC channels. The CC reaction (3.5) is very well suited for measuring the solar neutrino spectrum: unlike in the case of $\nu_a e$ scattering (3.3) in which the energy of incoming neutrino is shared between two light particles in the final state, the final state of the reaction (3.5) contains only one light particle – electron, and a heavy $2p$ system whose kinetic energy is relatively small. Therefore the electron energy is strongly correlated with the energy of the incoming neutrino. The CC electron spectrum measured by SNO (fig. 3.5) confirms the flat spectrum measured by SK.

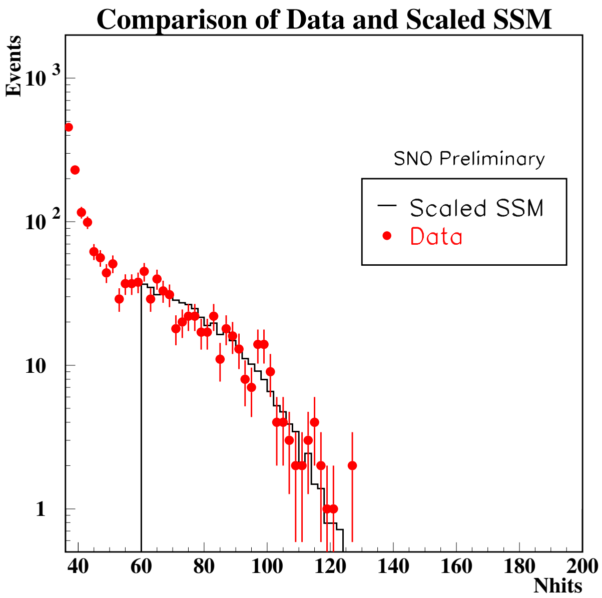

Figure 3.5: CC electron spectrum (distribution of events vs number of PMT hits). The line is a scaled standard solar model prediction. The scaling factor is not specified. From [37].

The cross section of the NC reaction (3.6) is the same for neutrinos of all three flavours, and therefore oscillations between ν_e and ν_μ or ν_τ would not change the NC detection rate in the SNO experiment. On the other hand, these oscillations would deplete the solar ν_e flux, reducing the CC event rate. Therefore the CC/NC ratio is a sensitive probe of neutrino flavour oscillations. If solar ν_e oscillate into electroweak singlet (sterile) neutrinos, both CC and NC event rates will be suppressed.

In summer 2001 new data were presented by the SNO collaboration. The flux of ν_e's from ^{8}B decay measured by the CC reaction rate is $\phi^{\rm CC}(\nu_e) = 1.75 \pm 0.07$ (stat.)$^{+0.12}_{-0.11}$ (sys.) $\pm$ 0.05 (theor.) $\times 10^6$ cm^{-2}s^{-1}. Assuming no flavor transformation, the flux inferred from the ES reaction rate, which also has a small sensitivity to ν_μ's and ν_τ's, is $\phi^{\rm ES}(\nu_x) = 2.39 \pm$ 0.34 (stat.)$^{+0.16}_{-0.14}$ (sys.) $\times 10^6$ cm^{-2}s^{-1}. Comparison of $\phi^{\rm CC}(\nu_e)$ to the Super-Kamiokande Collaboration's precision value of $\phi^{\rm ES}(\nu_x)$ yields a 3.3σ difference, assuming the systematic uncertainties are normally distributed, providing evidence that there is a non-electron flavor active neutrino component in the solar flux. The total flux of active ^{8}B neutrinos is thus determined to be $5.44 \pm 0.99 \times 10^6$ cm^{-2}s^{-1}, in close agreement with the predictions of solar models.

The Borexino experiment is scheduled to start taking data in 2002. It will detect solar neutrinos through the $\nu_a e$ scattering with a very low energy threshold, and will be able to detect the ^{7}Be neutrino line. Different solutions of the solar neutrino problem predict different degree of suppression of ^{7}Be neutrinos, and their detection could help discriminate between these solutions. Observation of the ^{7}Be neutrino line would be especially important in the case of the VO solution. Due to the eccentricity of the earth's orbit, the distance between the sun and the earth varies by about 3.5% during the year, and this should lead to varying oscillation phase (and therefore varying solar neutrino signal) in the case of vacuum neutrino oscillations. This seasonal variation can in principle be separated from the trivial 7% variation due to the $1/L^2$ law which is not related to neutrino oscillations [1]. Since the oscillation phase depends on neutrino energy, integration over significant energy intervals may make it difficult to observe the seasonal variations of the solar neutrino flux due to VO. The ^{7}Be neutrinos are monochromatic, which should facilitate the observation of the seasonal variations at Borexino.

Borexino will also be capable of confirming or refuting the LOW solution: a strong day/night effect predicted for ^{7}Be neutrinos by this solution should be clearly detectable at Borexino [37]. On the other hand, the LMA solution will be tested by the KamLAND experiment, which will start taking data in 2001. Although it will be a reactor neutrino experiment, its very long baseline will enable it to probe very small values of Δm^2, relevant for the LMA solution (see the next section). One can hope that the combined data of the currently operating and forthcoming experiments will allow to finally resolve the solar neutrino problem.

3.2 Reactor neutrino experiments

In reactor neutrino experiments oscillations of electron antineutrinos into another neutrino species are searched for by studying possible depletion of the $\bar\nu_e$ flux beyond the usual geometrical one. These are the disappearance experiments, because the energies of the reactor $\bar\nu_e$'s

[1] The seasonal dependence of the SK detection rate is in a good agreement with the $1/L^2$ law, with $\chi^2/d.o.f. =$ 4.1/7 (goodness of fit 76%).

($\langle E\rangle \simeq 3$ MeV) are too small to allow the detection of muon or tauon antineutrinos in CC experiments. Small $\bar{\nu}_e$ energy makes the reactor neutrino experiments sensitive to oscillations with rather small values of Δm^2. Up to now, no evidence for neutrino oscillations has been found in the reactor neutrino experiments, which allowed to exclude certain regions in the neutrino parameter space. The best constraints were obtained by the CHOOZ experiment in France [38]. For the values of $\Delta m_{31}^2 \equiv \Delta m_{atm}^2$ in the SK allowed region $(1.5-5)\times 10^{-3}$ eV^2, the CHOOZ results give the following constraint on the element U_{e3} of the lepton mixing matrix: $|U_{e3}|^2(1-|U_{e3}|^2) < 0.055-0.015$ at 90% c.l., i.e. $|U_{e3}|$ is either small or close to unity. The latter possibility is excluded by solar and atmospheric neutrino observations, and one finally obtains

$$\sin^2\theta_{13} \equiv |U_{e3}|^2 \leq (0.06-0.018) \quad \text{for} \quad \Delta m_{31}^2 = (1.5-5)\times 10^{-3}\ \text{eV}^2\,. \tag{3.7}$$

This is the most stringent constraint on $|U_{e3}|$ to date.

Presently, a long baseline reactor experiment KamLAND is under construction in Japan. This will be a large liquid scintillator detector experiment using the former Kamiokande site. KamLAND will detect electron antineutrinos coming from several Japanese and Korean power reactors at an average distance of about 180 km. KamLAND is scheduled to start taking data in 2001 and will be sensitive to values of Δm^2 as low as 4×10^{-6} eV^2, i.e. in the range relevant for the solar neutrino oscillations! It is expected to be able to probe the LMA solution of the solar neutrino problem (see fig. 3.6). It may also be able to directly detect solar ^{8}B and ^{7}Be neutrinos after its liquid scintillator has been purified to ultra high purity level by recirculating through purification.

3.3 Short baseline accelerator neutrino experiments

There have been a number of accelerator experiments looking for neutrino oscillations. In all but one no evidence for oscillations was found and constraints on oscillation parameters were obtained. The LSND Collaboration have obtained an evidence for $\bar{\nu}_\mu \to \bar{\nu}_e$ and $\nu_\mu \to \nu_e$ oscillations [39]. The LSND result is the only indication for neutrino oscillations that is a signal and not a deficiency. The KARMEN experiment [40] is looking for neutrino oscillations in $\bar{\nu}_\mu \to \bar{\nu}_e$ channel. No evidence for oscillations has been obtained, and part of the LSND allowed region has been excluded. In fig. 3.7 the results from LSND and KARMEN experiments are shown along with the relevant constraints from the BNL E776, CCFR, CHOOZ and Bugey experiments. One can see that the only domain of the LSND allowed region which is presently not excluded is a narrow strip with $\sin^2 2\theta \simeq 1\times 10^{-3} - 4\times 10^{-2}$ and $\Delta m^2 \simeq 0.2-2$ eV^2.

The existing neutrino anomalies (solar neutrino problem, atmospheric neutrino anomaly and the LSND result), if all interpreted in terms of neutrino oscillations, require three different scales of mass squared differences: $\Delta m_\odot^2 \leq 10^{-4}$ eV^2, $\Delta m_{atm}^2 \sim 10^{-3}$ eV^2 and $\Delta m_{\rm LSND}^2 \geq 0.2$ eV^2. This is only possible with four (or more) light neutrino species. The fourth light neutrino cannot be just the 4th generation neutrino similar to ν_e, ν_μ and ν_τ because this would be in conflict with the experimentally measured width of Z^0 boson [see eq. (2.2)]. It can only be an electroweak singlet (sterile) neutrino. Therefore the LSND result, if correct, would imply the existence of a light sterile neutrino.

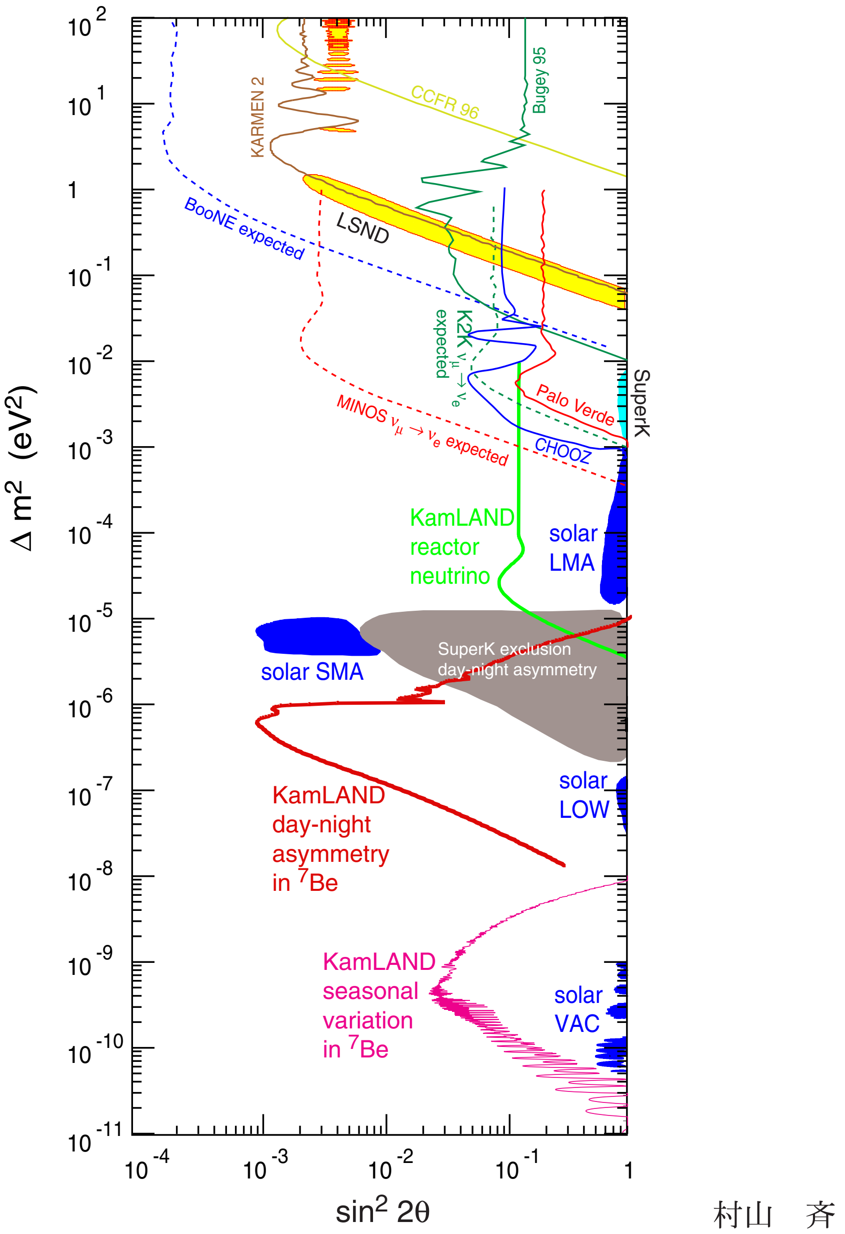

Figure 3.6: Left panel: results of the present and sensitivities of future $\nu_e \leftrightarrow \nu_\mu$ oscillations searches (90% c.l.). The plot by H. Murayama.

Out of all experimental evidences for neutrino oscillations, the LSND result is the only one that has not yet been confirmed by other experiments. It is therefore very important to have it independently checked. This will be done by the MiniBooNE (first phase of BooNE) experiment at Fermilab [41]. MiniBooNE will be capable of observing both $\nu_\mu \to \nu_e$ appearance and ν_μ disappearance. If the LSND signal is due to $\nu_\mu \to \nu_e$ oscillations, MiniBooNE is expected to detect an excess of several hundred of ν_e events during its first year of operation, establishing the oscillation signal at 8σ to 10σ level (see fig. 3.6). If this happens, the second detector will be installed, with the goal to accurately measure the oscillation parameters. MiniBooNE will

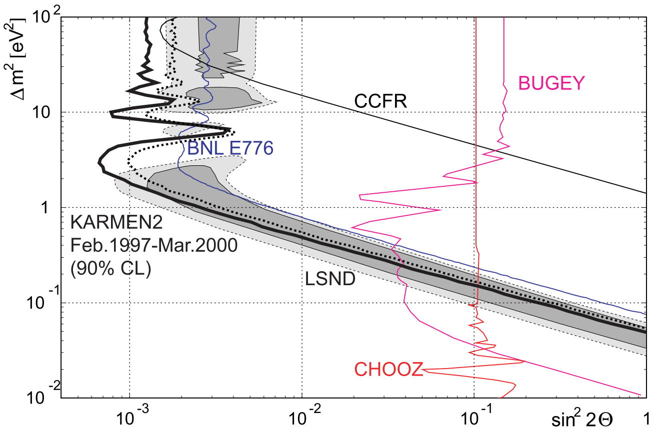

Figure 3.7: LSND allowed parameter region for $\bar{\nu}_\mu \to \bar{\nu}_e$ oscillations (shaded areas) along with KARMEN, BNL E776, CCFR, CHOOZ and Bugey exclusion regions.

begin taking data in 2002.

3.4 Long baseline accelerator neutrino experiments

A number of long baseline accelerator neutrino experiments have been proposed to date. They are designed to independently test the oscillation interpretation of the results of the atmospheric neutrino experiments, accurately measure the oscillation parameters and to (possibly) identify the oscillation channel.

3.4.1 K2K

The first of these experiments, K2K (KEK to Super-Kamiokande), started taking data in 1999. It has a baseline of 250 km, average neutrino energy $\langle E \rangle \simeq 1.4$ GeV and is looking for ν_μ disappearance. K2K should be able to test the highest-Δm^2 part of the region of oscillation parameters allowed by the SK atmospheric neutrino data, but not the lowest-Δm^2 part of it. The sensitivity for ν_μ disappearance expected after 3 years at nominal intensity extends down to between 2 and 3×10^{-3} eV^2 (figure 3.8). With the small envisaged statistics (170 events without oscillations in 5 years), and the small L/E reach, the oscillation pattern is unlikely to get fully resolved.

The data collected from June 1999 to March 2001 (2.6×10^{19} protons on target) have been reported [5]. The observed number of fully contained μ-like event is 44 with a background of less than 10^{-3} events. This has to be compared with the expected number $63.9^{+6.1}_{-6.6}$ assuming no neutrino oscillations. The observed deficiency of μ-like events disfavours the no-oscillation hypothesis at 2σ level and supports the neutrino oscillation interpretation of the SK atmospheric neutrino data [6]. However, more data have to be accumulated before definitive conclusions can be drawn.

3.4.2 NUMI

The construction of the American long baseline programme NUMI [42] started in 1999. MINOS is a 5.4 kt (3.3 kt fiducial mass) detector dedicated to ν_μ disappearance. The beam is scheduled to be operative in December 2004, and the detector is planned to be partially operational in 2003 (with cosmics), and fully completed in 2004. The expected performance of MINOS for 10 kty is outlined in figure 3.8. The experimental sensitivity reaches 2×10^{-3} eV^2 in Δm^2 with the reference beam ($< E_\nu >\sim 17$ GeV), and 6×10^{-4} eV^2 with a low energy version of the beam called PH2(low) ($< E_\nu >\sim 5$ GeV); the corresponding discovery contour (4 σ) goes down to 1×10^{-3} eV^2.

The oscillation pattern is, in principle, dectable at the highest allowed Δm^2 if the low energy beam is used [43], but it has a hard time to observe a reappearance signal in the lower Δm^2 range.

3.4.3 CNGS

The CERN neutrino beam to Gran Sasso (CNGS) [48] was approved in december 1999, to become operational in 2005. The main physics goal of the CNGS project is the experimental observation of τ appearance. This could be achieved either directly through the detection of the τ decay kink in nuclear emulsion (Opera) [49] or indirectly through τ detection using kinematical criteria (Icarus) [51].
The beam spectrum ($< E_\nu >= 17\ GeV$) is, therefore, optimized in order to get the highest number of τ from ν_τ interactions.

However, with this energy spectrum and the CERN-Gran Sasso baseline (732 km), assuming the Δm^2 values allowed by the SK experiment, the $\nu_\mu \to \nu_\tau$ oscillation probability is such that the expected ν_τ event rate can be critically small in the low Δm^2 region. Combining this with the τ detection threshold, it is impossible to observe an oscillation pattern in ν_τ appearance.

Opera

Opera is based on the Emulsion Cloud Chamber (ECC) detector, and has a modular structure. Each module is constituted by an active region, made of a sandwich of passive material plates interspaced with emulsion layer, and a tracking system for vertex determination and magnetized iron specrometers. Tau identification is allowed by the fine granularity of ECC that enable to see the τ decay kink, while muon charge and momentum is measured by the spectrometers, and the interaction vertex in active target is determined by tracking system. The total mass proposed for the full detector is 2 kt.

After selection cuts, performed in order to reject various kind of backgrounds, the number of the expected τ events and backgrounds detected by the full OPERA detector, in 5 years of data taking, with the CNGS expected flux is shown in table 3.2 .

With the background estimates and the corresponding systematic uncertainties, the observation of at least 6 events is required after a 5 years run to obtain a 4σ statistical significance on the detected signal. This means that the experiment becomes very difficult at low Δm^2.

The overall sensitivity to $\nu_\mu \to \nu_\tau$ oscillations at 90% C.L. is shown in figure 3.9 for a five year run ($2.25 \times 10^{20} pot$).

A measurement of the oscillation parameters can be obtained from the number of detected τ

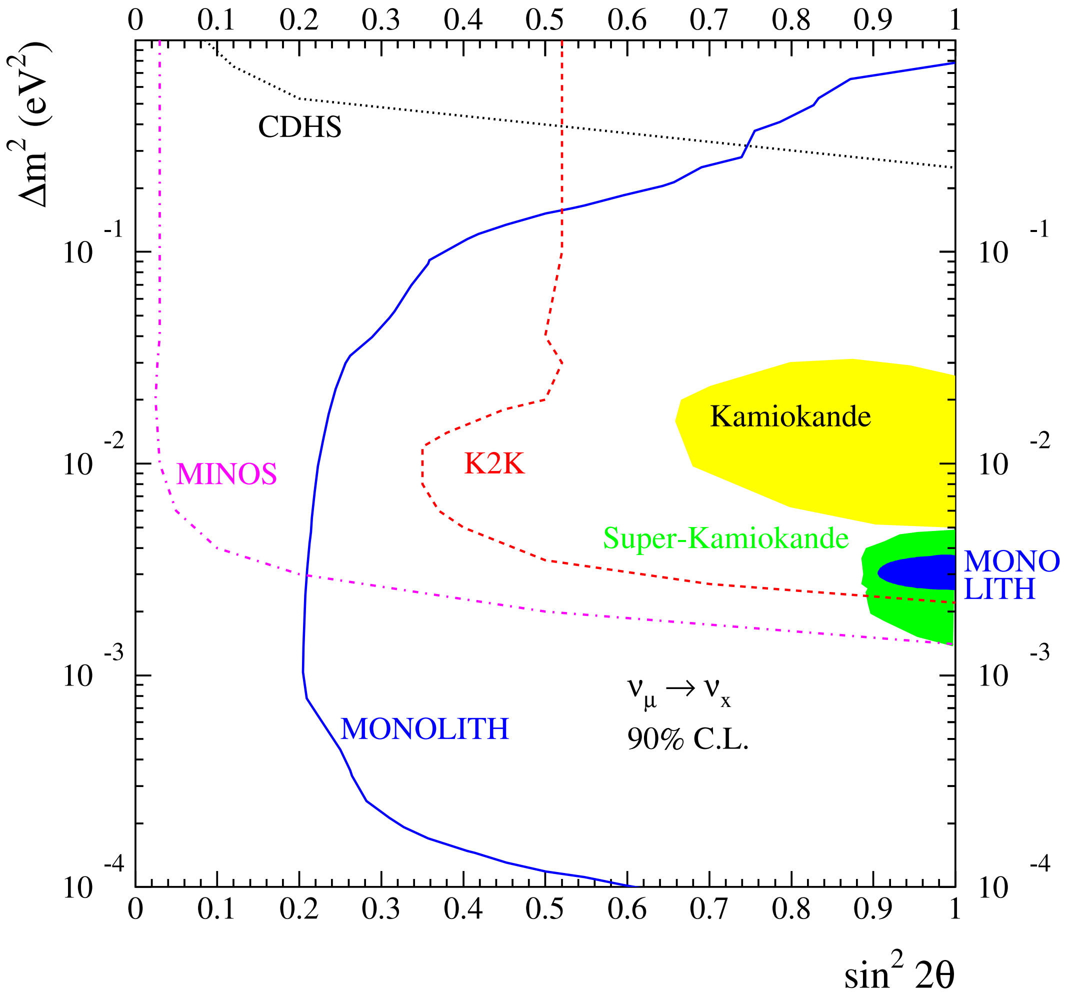

Figure 3.8: Expected sensitivity contours for ν_μ disappearance for K2K [4, 44] (5 years), MINOS [42] (3 years reference beam, for low energy beam see text) and MONOLITH (4 years). Also shown are the exclusion contour from CDHS [45] , the recent allowed areas from Super-Kamiokande [46] and Kamiokande [47] and the expected allowed area of MONOLITH for $\Delta m^2 = 3.0\ 10^{-3}$ (4 years).

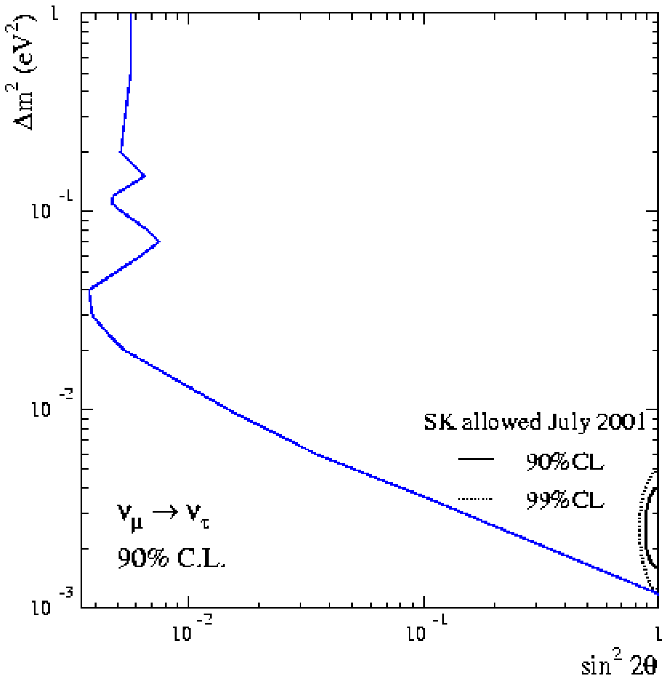

Figure 3.9: Sensitivity of the OPERA experiment (2 kt mass) at 90% C.L. to $\nu_\mu - \nu_\tau$ oscillations after a five years run. The recent (July 2001) allowed regions from Super-Kamiokande are also shown.

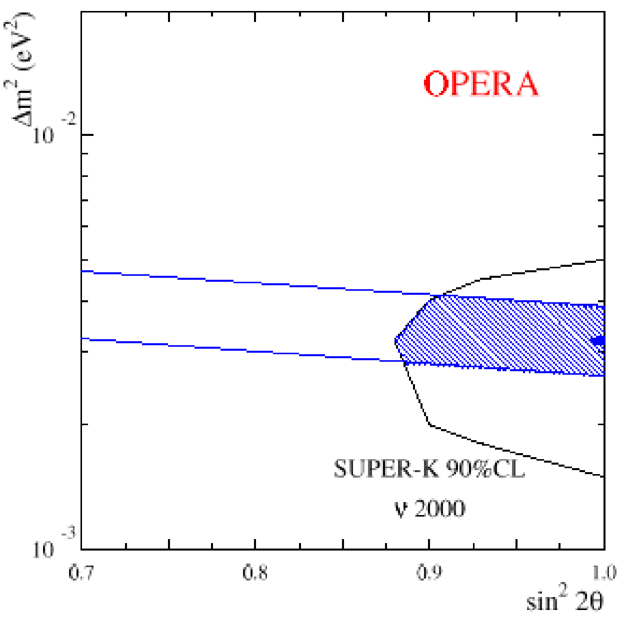

Figure 3.10: The band gives the 90% C.L. allowed region of the oscillation parameters as determined by OPERA observing a number of events corresponding to what is expected for full mixing and $\Delta m^2 = 3.2\ 10^{-3}$

Table 3.2: Expected numbers of τ and background events collected by OPERA in five years of data taking ($2.25 \times 10^{20} pot$). Signal events are given for full mixing and for three values of Δm^2: the most recent best fit by Super-Kamiokande and the two 90% CL limits.

Signal: $\Delta m^2 = 1.2\ 10^{-3}$	Signal: $\Delta m^2 = 2.4\ 10^{-3}$	Signal: $\Delta m^2 = 5.4\ 10^{-3}$	Bkgnd.
2.7	10.8	53.5	0.75

events, but, due to the fact that the oscillation pattern is not fully explored, it is not possible to disantangle the two parameters (Δm^2 and $sin^2(2\theta)$) and the result is the allowed band shown in figure 3.10.

Icarus

The approved Icarus experiment is a 600 *ton* liquid argon TPC and it is forseen to be installed at the end of 2002 in the Gran Sasso laboratory. The collaboration propose to install a detector constituted by an array of five 600 *ton* modules (one module per year).
In this configuration, the number of ν_τ events detected after 5 year of data taking with the nominal CNGS beam ($2.25 \times 10^{20} pot$) is shown in table 3.3 , giving results similar to the OPERA ones and so similar excluded regions and oscillation parameter measurements.

Table 3.3: Expected numbers of τ and background events collected by ICARUS in five years of data taking ($2.25 \times 10^{20} pot$). Signal events are given for full mixing and for four values of Δm^2

Signal: $\Delta m^2 = 1.6\ 10^{-3}$	$\Delta m^2 = 2.5\ 10^{-3}$	$\Delta m^2 = 3.0\ 10^{-3}$	$\Delta m^2 = 4.0\ 10^{-3}$	Bkgnd.
4.9	11.9	17.2	30.5	0.75

3.4.4 JHF

The JHF 50 GeV-PS beam (start operation in 2007) will provide neutrino beams which are two orders of magnitude more intense than the K2K one. While the accelerator has to be newly built, the Super-Kamiokande detector will act, in a first stage, as far detector, while an improvement in the detector dimensions is considered for a possible future stage. The primary physics goals shall be the measurement of the neutrino oscillation parameter Δm^2 with an accuracy of $2\times10^{-4}\ eV^2$ and $\sin^2\theta$ with an accuracy of 0.04. It will observe the clear pattern of neutrino oscillation in the region of Δm^2 above $2\times10^{-3}\ eV^2$. By searching for the appearance of electron neutrinos, it could reach the sensitivity of $sin^2 2\theta_e (\equiv sin^2 2\theta_{13} \times sin^2\theta_{23})$ down to 0.03.

3.4.5 Neutrino Factory

Among widely discussed future projects are neutrino factories [14] – muon storage rings producing intense beams of high energy neutrinos. In addition to high statistics studies of neutrino interactions, experiments at neutrino factories should be capable of measuring neutrino oscillation parameters with high precision and probing the subdominant neutrino oscillation channels, matter effects and CP violation effects in neutrino oscillations.
We will widely discuss this topic in chapter 7.

3.5 Atmospheric neutrinos

Atmospheric neutrinos are electron and muon neutrinos and their antineutrinos which are produced in the hadronic showers induced by primary cosmic rays in the earth's atmosphere. The main mechanism of production of the atmospheric neutrinos is given by the following chain of reactions:

$$\begin{array}{rcl} p(\alpha, ...) + Air & \rightarrow & \pi^{\pm}(K^{\pm}) \quad + \quad X \\ & & \pi^{\pm}(K^{\pm}) \quad \rightarrow \quad \mu^{\pm} + \nu_{\mu}(\bar{\nu}_{\mu}) \\ & & \qquad\qquad\qquad\quad \mu^{\pm} \rightarrow e^{\pm} + \nu_e(\bar{\nu}_e) + \bar{\nu}_{\mu}(\nu_{\mu}) \end{array} \tag{3.8}$$

Atmospheric neutrinos can be observed directly in large mass underground detectors predominantly by means of their charged current (CC) interactions:

$$\begin{aligned} \nu_e(\bar{\nu}_e) + A \rightarrow e^-(e^+) + X \,, \\ \nu_{\mu}(\bar{\nu}_{\mu}) + A \rightarrow \mu^-(\mu^+) + X \,. \end{aligned} \tag{3.9}$$

Calculations of the atmospheric neutrino fluxes predict the ν_{μ}/ν_e ratio that depends on neutrino energy and the zenith angle of neutrino trajectory, approaching 2 for low energy neutrinos and horizontal trajectories but exceeding this value for higher energy neutrinos and for trajectories close to vertical. The overall uncertainty of the calculated atmospheric neutrino fluxes is rather large, and the total fluxes calculated by different authors differ by as much as 20 – 30%. At the same time, the ratio of the muon to electron neutrino fluxes is fairly insensitive to this uncertainty, and different calculations yield the ratios of muon-like to electron-like contained events which agree to about 5%. This ratio has been measured in a number of experiments, and the Kamiokande and IMB Collaborations reported smaller than expected ratio in their contained events, with the double ratio $R(\mu/e) \equiv [(\nu_{\mu}+\bar{\nu}_{\mu})/(\nu_e+\bar{\nu}_e]_{data}/[(\nu_{\mu}+\bar{\nu}_{\mu})/(\nu_e+\bar{\nu}_e)]_{MC} \simeq 0.6$ where MC stands for Monte Carlo simulations. The discrepancy between the observed and predicted atmospheric neutrino fluxes was called the atmospheric neutrino anomaly. The existence of this anomaly was subsequently confirmed by Soudan 2 [53], MACRO [54] and Super-Kamiokande experiments. Most remarkably, the Super-Kamiokande (SK) Collaboration obtained a very convincing evidence for the up-down asymmetry and zenith-angle dependent deficiency of the flux of muon neutrinos, which has been interpreted as an evidence for neutrino oscillations. We shall now discuss the SK data and their interpretation.

3.5.1 Super-Kamiokande detector

The SK detector is a 50 kt water Cherenkov detector (22.5 kt fiducial volume) equipped with more than 13,000 photomultiplier tubes. The charged leptons from CC neutrino interactions are detected by the photomultipliers as Cherenkov light rings. Muons can be distinguished from electrons since their Cherenkov rings are sharp whereas those produced by electrons are diffuse. The SK Collaboration subdivided their atmospheric neutrino events into several groups, depending on the energy of the charged leptons produced:

- Fully contained (FC) events are those for which the neutrino interaction vertex is located inside the detector and all final state particles do not get out of it. FC events are further subdivided into:

  - sub-GeV (visible energy < 1.33 GeV) and
  - multi-GeV (visible energy > 1.33 GeV) events.

- Partially contained (PC) events are those for which the produced muon exits the inner detector volume (only muons are penetrating enough).

The average energy of a neutrino producing a PC event in SK is ~ 15 GeV. Muon neutrinos can also be detected indirectly by observing the muons that they have produced in the material surrounding the detector. To reduce the background from atmospheric muons, only upward–going neutrino-induced muons are usually considered. A rough estimate of the energy spectrum of the upward–going muons has been obtained dividing them in two categories, passing (or through-going) and stopping muons. The latter, which stop inside the detector, correspond to the average parent neutrino energy ~ 10 GeV, whereas for the through-going muons the average neutrino energy is ~ 100 GeV.

The measurements of the double ratio $R(\mu/e)$ for contained events at SK (1144 live days) give [55, 56]

$$\begin{aligned} R &= 0.652 \pm 0.019\,(stat.) \pm 0.051\,(syst.) \quad \text{(sub-GeV)}\,, \\ R &= 0.668 \pm 0.034\,(stat.) \pm 0.079\,(syst.) \quad \text{(multi-GeV)}\,. \end{aligned} \tag{3.10}$$

The value of R for sub-GeV events is different from unity (to which it should be equal in no-oscillation case) by more than 6σ.

3.5.2 Zenith angle distributions

The zenith angle distributions of charged leptons which are experimentally measured do not coincide with those of their parent neutrinos: for multi-GeV neutrinos the average angle between the momenta of neutrinos and charged leptons is about $17°$, whereas for sub-GeV neutrinos it is close to $60°$. For PC events and upward going muons the correlation between the directions of momenta of muons and parent neutrinos is much better. The distances L traveled by neutrinos before they reach the detector vary in a wide range: for vertically downward going neutrinos (neutrino zenith angle $\Theta_\nu = 0$) $L \sim 15$ km; for horizontal neutrino trajectories ($\Theta_\nu = 90°$) $L \sim 500$ km; the vertically up-going neutrinos ($\Theta_\nu = 180°$) cross the earth along its diameter and for them $L \sim 13,000$ km.

The Super-Kamiokande experiment finds an anomaly in the neutrino zenith angle distribution. In fig. 3.11 the zenith angle distributions of the SK e-like and μ-like events are shown separately for sub-GeV and multi-GeV contained events. One can see that for e-like events, the measured zenith angle distributions agree very well with the MC predictions (shown by bars), both in the sub-GeV and multi-GeV samples, while for μ-like events both samples show zenith-angle dependent deficiency of event numbers compared to expectations. The deficit of muon neutrinos is stronger for upward going neutrinos which have larger pathlengths. In the multi-GeV sample, there is practically no deficit of events caused by muon neutrinos coming from the upper hemisphere ($\cos\Theta > 0$), whereas in the sub-GeV sample, all μ-like events exhibit a deficit which decreases with $\cos\Theta$.

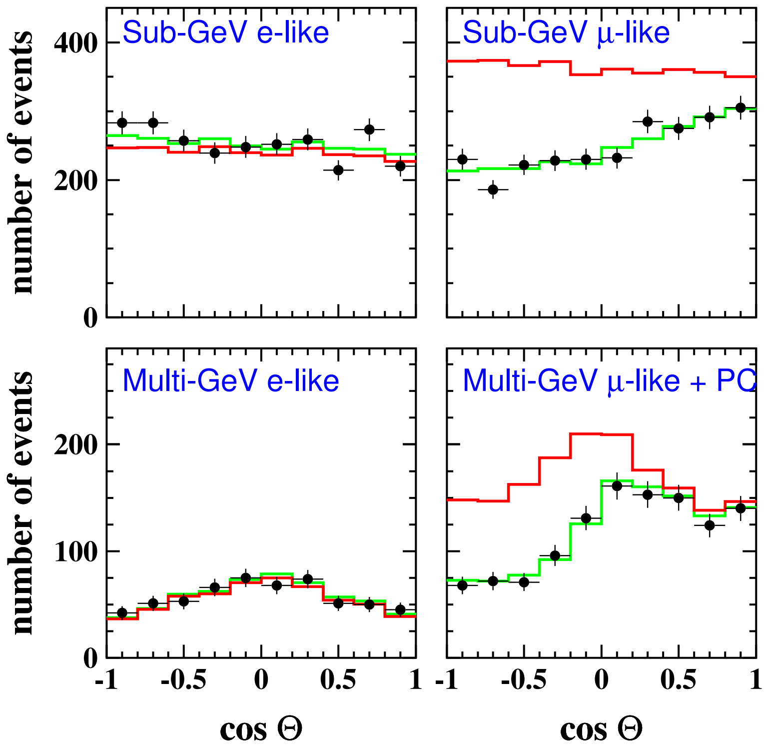

Figure 3.11: Zenith angle distributions for sub-GeV and multi-GeV e-like and μ-like events at SK (1144 live days). The red lines show the (no-oscillations) Monte Carlo predictions; green lines show the predictions for $\nu_\mu \leftrightarrow \nu_\tau$ oscillations with the best-fit parameters $\Delta m^2 = 2.4 \times 10^{-3}$ eV^2, $\sin^2 2\theta = 1.0$. From [55].

This pattern is consistent with oscillations $\nu_\mu \leftrightarrow \nu_\tau$ or $\nu_\mu \leftrightarrow \nu_s$ where ν_s is a sterile neutrino. Muon neutrinos responsible for the multi-GeV sample are depleted by the oscillations when their pathlength is large enough; the depletion becomes less pronounced as the pathlength decreases ($\cos\Theta$ increases); for neutrinos coming from the upper hemisphere, the pathlengths are too short and there are practically no oscillations. Neutrinos responsible for the sub-GeV μ-like events have smaller energies, and so their oscillation lengths are smaller; therefore even neutrinos coming from the upper hemisphere experience sizeable depletion due to the oscillations. For up-going sub-GeV neutrinos the oscillation length is much smaller than the pathlength and they experience averaged oscillations. The solid line in fig. 3.11 obtained with the $\nu_\mu \leftrightarrow \nu_\tau$ oscillation parameters in the 2-flavour scheme $\Delta m^2 = 2.4 \times 10^{-3}$ eV^2, $\sin^2 2\theta = 1.0$ fits the data very well.

3.5.3 Up/Down asymmetry

An informative parameter characterizing the distortion of the zenith angle distribution is the up-down event ratio U/D, where up corresponds to the events with $\cos\Theta < -0.2$ and down to those with $\cos\Theta > 0.2$. The flux of atmospheric neutrinos is expected to be nearly up-down symmetric for neutrino energies $E \geq 1$ GeV. Any significant deviation of the up-down asymmetry of neutrino induced events from 1 is an indication of some new neutrino physics. The U/D ratio measured for the SK multi-GeV μ-like events is [55, 56]

$$U/D = 0.54 \pm 0.04\,(stat.) \pm 0.01\,(syst.)\,, \tag{3.11}$$

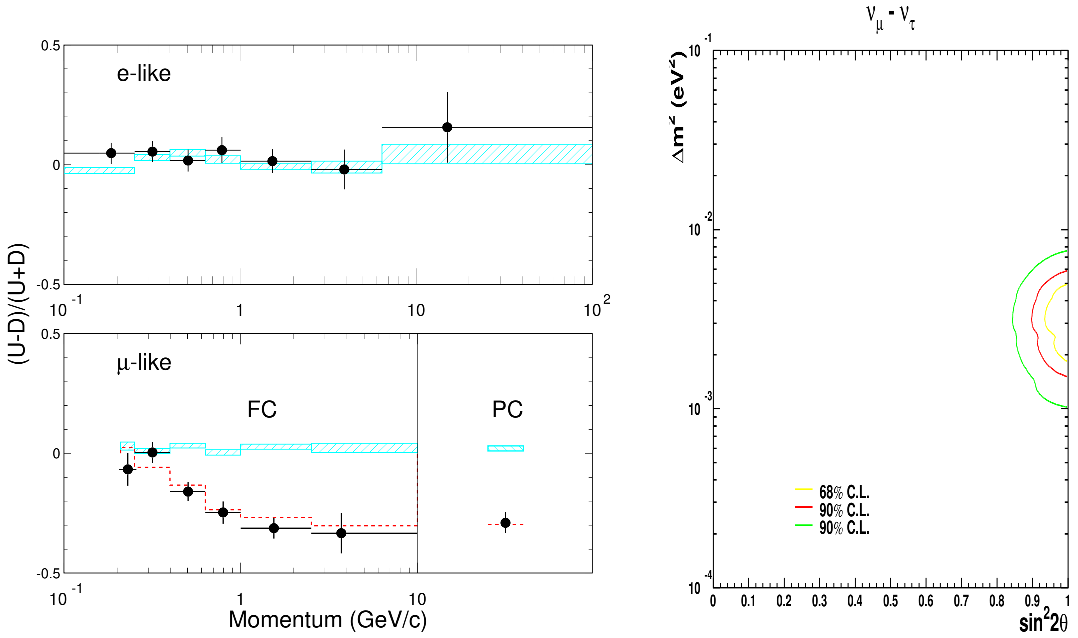

Figure 3.12: Left panel: up-down asymmetry vs event momentum for single ring e-like and μ-like events in SK (1144 live days). Blue hatched boxes define no oscillation expectation, while dashed line corresponds to $\nu_\mu \leftrightarrow \nu_\tau$ oscillations with $\Delta m^2 = 2.4 \times 10^{-3}$ eV^2, $\sin^2 2\theta = 1$. Right panel: SK allowed regions of oscillations parameters for $\nu_\mu \leftrightarrow \nu_\tau$ channel in 2-flavour scheme (FC + PC events) [18].

i.e. is below unity by about 9σ!

The dependence of the asymmetries for e-like FC and μ-like FC+PC events on the event momentum is shown in fig. 3.12 (left panel). One can see that for e-like events the asymmetry $A \equiv (U - D)/(U + D) \simeq 0$ for all momenta. At the same time, for μ-like events the asymmetry is close to zero at low momenta and decreases with momentum. This could be understood in terms of the ν_μ oscillations. For very small momenta, the oscillation length is small and both up-going and down-going neutrino fluxes are depleted by oscillations to about the same extent; in addition, loose correlation between the directions of the momenta of the charged lepton and of its parent neutrino tends to smear out the asymmetry at low energies. With increasing momentum the oscillation length increases, and the pathlength of down-going neutrinos becomes too small for oscillations to develop.

3.5.4 Neutrino oscillation hypothesis

If we assume that the observed anomaly is due to 2-flavour neutrino oscillation, the combined analysis of the SK FC, PC and upward muon event data yields the best-fit values $\Delta m^2 = 2.4 \times 10^{-3}$ eV^2 and $\sin^2 2\theta = 1.0$, with the very high quality of the fit: $\chi^2/d.o.f. = 135.4/152$ (right panel of fig. 3.12). The upper and lower 90% C.L. of the Δm^2 are respectively 5.4×10^{-3} eV^2 and 1.2×10^{-3} eV^2. The $\chi^2/d.o.f.$ value has to be compared with that of the no-oscillation hypothesis: $\chi^2/d.o.f. = 316.2/154$, which is a very poor fit.

Are neutrino oscillations that are responsible for the depletion of the ν_μ flux $\nu_\mu \leftrightarrow \nu_\tau$ or $\nu_\mu \leftrightarrow \nu_s$? For contained events, the oscillation probabilities in these two channels are nearly the same and the data can be fitted equally well in both cases, with very similar allowed ranges of the oscillation parameters. However, for higher energy PC and upward going events there are important differences between these two cases. In the 2-flavour scheme, $\nu_\mu \leftrightarrow \nu_\tau$ oscillations are not affected by matter because the interactions of ν_μ and ν_τ with matter are identical. However, sterile neutrinos do not interact with matter at all, and therefore the $\nu_\mu \leftrightarrow \nu_s$ oscillations are affected by the matter-induced potential $V_\mu - V_s = V_\mu$. At low energies, the kinetic energy difference $\Delta m^2/2E$ dominates over V_μ, and the earth's matter effects are unimportant. They become important at higher energies, when $\Delta m^2/2E \sim V_\mu$; at very high energies, when $\Delta m^2/2E \ll V_\mu$, matter strongly suppresses neutrino oscillations both in $\nu_\mu \leftrightarrow \nu_s$ and $\bar{\nu}_\mu \leftrightarrow \bar{\nu}_s$ channels. Therefore the oscillations of high energy neutrinos traveling significant distances in the earth should be strongly suppressed in this case. Such a suppression was searched for in PC and upward trough-going event samples, but has not been observed. This fact together with the analysis of the neutral current enriched multi-ring events allowed the SK Collaboration to exclude pure $\nu_\mu \to \nu_s$ oscillations at the 99% c.l. [55, 56, 57]. The oscillations into sterile neutrinos are, however, allowed in the 4-neutrino framework, with the weight that can be as large as about 50% [58]

Can $\nu_\mu \leftrightarrow \nu_e$ oscillations be responsible for the observed anomalies in the atmospheric neutrino data? The answer is no, at least not as the dominant channel. Explaining the data requires oscillations with large mixing equal or close to the maximal one; $\nu_\mu \leftrightarrow \nu_e$ oscillations would then certainly lead to a significant distortion of the zenith angle distributions of the e-like contained events, contrary to observations. In addition, for Δm^2 in the range $\sim 10^{-3}$ eV^2 which is required by the atmospheric neutrino data, $\nu_\mu \leftrightarrow \nu_e$ oscillations are severely restricted by the CHOOZ reactor antineutrino experiment [38], which excludes these oscillations as the main channel of the atmospheric neutrino oscillations.

However, $\nu_\mu \leftrightarrow \nu_e$ and $\nu_e \leftrightarrow \nu_\tau$ can be present as subdominant channels of the oscillations of atmospheric neutrinos. This may lead to interesting matter effects on oscillations of neutrinos crossing the earth on their way to the detector. Matter can strongly affect $\nu_e \leftrightarrow \nu_{\mu,\tau}$ and $\bar{\nu}_e \leftrightarrow \bar{\nu}_{\mu,\tau}$ oscillations leading to an enhancement of the oscillation probabilities for neutrinos and suppression for antineutrinos or vice versa, depending on the sign of the corresponding mass squared difference.

Since three neutrino flavours are known to exist, oscillations of atmospheric neutrinos should in general be considered in the full 3-flavour framework (assuming that no sterile neutrinos take part in these oscillations). Three flavour analyses [55, 56, 59, 30] only slightly modify the 2-flavour results, which is a consequence of the smallness of the leptonic mixing parameter U_{e3}.

3.5.5 Hypothesis outside oscillation

Are the standard neutrino oscillations the sole possible explanation of the observed atmospheric neutrino anomalies? In principle, other explanations are possible [9]:

- exotic types of neutrino oscillations
- matter-induced oscillations due to flavour-changing interactions of neutrinos with medium
- oscillations due to small violations of the Lorentz or CPT invariance or of the gravitational equivalence principle
- potential decoherence effects

- influence of large extra dimensions
- neutrino decay.

The neutrino decay mechanism fits the SK data quite well, the quality of the fit being as good as the one for the standard neutrino oscillations [60] (see figure 3.13 - left panel). The reason for this is that the oscillations and decay lead to very similar averaged survival probabilities for ν_μ and the poor L/E resolution of the SK detector does not allow to discriminate between the two hypothesis. One could discriminate between the two solutions in the experiments like the massive magnetized calorimeter called MONOLITH. The MONOLITH detector will have a much better L/E resolution than that of the SK, and therefore will be able to clearly detect the full first oscillation swing of the ν_μ survival probability (i.e. not only disappearance but also reappearance of ν_μ) in the case of the neutrino oscillation solution of the atmospheric neutrino anomaly (see figure 3.13 - right panel). We will focus on the MONOLITH characteristics and performances as a main topic of this thesis.

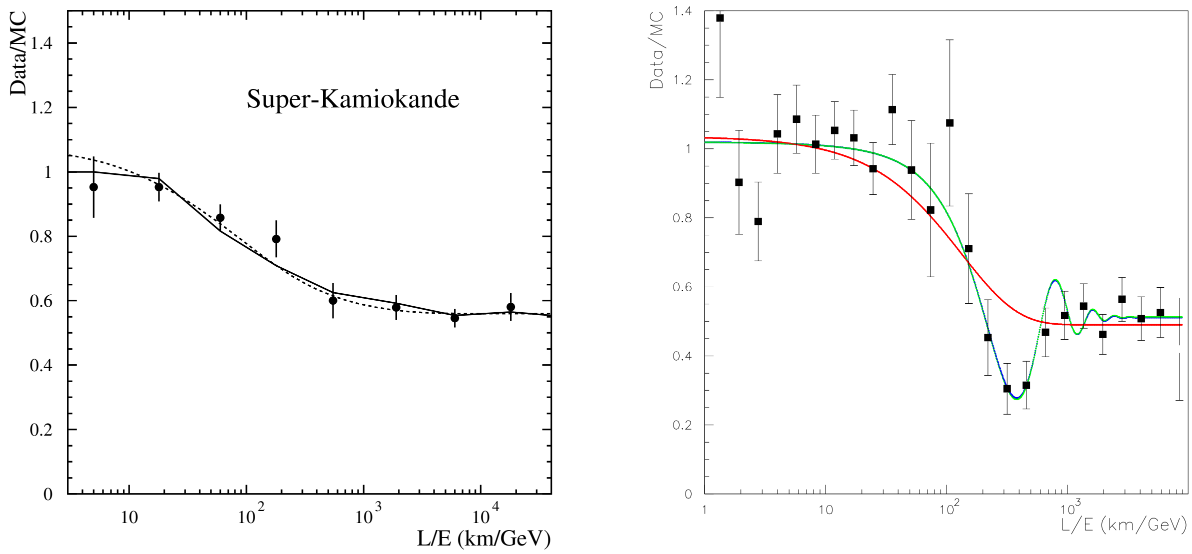

Figure 3.13: *Left*: L/E distribution from Super-Kamiokande [3, 46] compared to the best fit oscillation hypothesis (continous line), and to a parametrization corresponding to the neutrino decay model of ref. [10] (dashed line). The oscillations are smoothed out by detector resolution. *Right*: L/E distribution to be expected from MONOLITH for $\Delta m^2 = 3 \times 10^{-3}$ eV^2 compared to the best fit oscillation hypothesis (oscillating line) and to the corresponding best fit of the neutrino decay model of ref. [10] (smooth threshold effect).

Chapter 4

The MONOLITH detector

4.1 Introduction

To explicitly detect an oscillation pattern in the L/E spectrum of atmospheric muon neutrinos, the energy E and direction θ of the incoming neutrino have to be measured in each event. The latter can be estimated, in the simplest experimental approach, from the direction of the muon produced from the ν_μ charged-current interaction. The neutrino energy E can be obtained by means of energy measurements of the muon and of the hadrons produced in the interaction. In order to make the oscillation pattern detectable, the ratio of the neutrino path-length to its energy L/E have to be measured with a FWHM error smaller than half of the modulation period. The energy and angular resolutions of the detector or, more generally, the experimental approach are constrained by this condition. The L/E resolution improves at high energies, mostly because the muon direction gives a better estimation of the neutrino direction. Thus the ability to measure high momentum muons (in the multi-GeV range), which is rather limited in the on-going atmospheric neutrino experiments, is particularly rewarding.

These arguments previously led to consider as a suitable detector a large mass and high-density tracking calorimeter [62]. A large mass is necessary to provide the necessary number of neutrino interactions at high energy, while the high density allows high energy muon containment (i.e. muon momentum determined by range). A sizeable increase in sensitivity for Δm^2 larger than 3×10^{-3} eV^2 can be achieved with the addition of a magnetic field. This improves the efficiency at small L/E as a consequence of the increased muon acceptance at high momenta. Moreover a high-density detector allows to select a pure ν_μ-CC sample providing good π/μ separation. The measurement of the muon energy and direction can be obtained with good precision. On the other hand the overall low energy neutrino sample L/E resolution can be controlled, even with a coarse resolution to hadrons, by selecting interactions of limited inelasticity. This is shown in the expression of the relative L/E resolution:

$$\frac{\sigma^2_{L/E}}{(L/E)^2} = \frac{\sigma^2_E}{E^2} + \frac{\sigma^2_L}{L^2} \tag{4.1}$$

$$\simeq \frac{\sigma^2_{E_\mu}}{E^2_\mu}(1-y)^2 + \frac{\sigma^2_{E_h}}{E^2_h}y^2 + \tan^2\theta\sigma^2_\theta; \tag{4.2}$$

where E, E_μ and E_h are the neutrino, muon and hadronic energies respectively, $y = E_h/E$ is the inelasticity of the interaction and θ is the zenith angle of the incoming neutrino. Events of limited inelasticity have both a good resolution on the neutrino energy, dominated by the resolution on the muon energy, and on the neutrino direction estimate from the muon direction. As shown in equation (4.2) the acceptance at small L/E can only be achieved by recovering events of high energy, since near the horizontal (at small L) the L/E resolution is intrinsically limited by the knowledge of the neutrino direction. Therefore the detector does not need to be fully isotropic. Improvement of the L/E resolution through better hadron reconstruction would only be possible by using a calorimeter of much higher granularity, which increases cost, reduces muon containment and conflicts with the requirement of a large mass.

In addition to these requirements on the L/E resolution, the experimental apparatus should guarantee the identification of the neutrino flight direction. In case the interaction vertex is not identified, this condition turns out to be very stringent and requires the identification of the muon flight direction with high efficiency. Different techniques based on the increase of curvature along the track in the magnetic field, on multiple scattering along the track or on time-of-flight measurements can be used. The latter technique is more effective and allows almost perfect up/down discrimination of the relevant ν_μ-CC events for timing resolution of the order of 1 ns. A precise time-of-flight along the muon track will be also of utmost importance in the rejection of the cosmic muon background in the sample of partially contained ν_μ-CC events.

In summary, a detector performing the measurements discussed in the previous chapter has to provide NC/CC discrimination, muon momentum and charge measurement, some hadronic energy reconstruction capability, and up/down discrimination for muons above 1 GeV. Moreover it has to provide an event sample, with the requested L/E resolution, large enough to observe the modulation produced by ν_μ oscillations. A rejection power against incoming stopping muons better than 10^{-5} is needed in the Gran Sasso underground laboratory. Finally the detector has to fit into an existing hall of the LNGS and it must have a reasonable cost.

It should be noted that all this can be achieved by choosing a high-mass tracking detector with a coarse structure and magnetic field. This final design of the massive magnetized calorimeter, called MONOLITH, was officially proposed in August 2000 [61].

4.2 Detector structure

A large modular structure has been chosen for the detector (figure 4.1). One module consists in a stack of 125 horizontal 8 cm thick iron planes with a surface area of 15.0×14.5 m^2, interleaved with 2.2 cm gaps housing sensitive elements. The height of the detector is thus 13.1 m including anti-seismic mechanical supports. Thinner planes, 2 and 4 cm thick, were also considered in the past. However, the 8 cm plane thickness resulted to be the best compromise between physics results and detector cost. The magnetic field configuration is also shown in figure 4.1; iron planes are magnetized at a magnetic induction of ≈ 1.3 T.

The detector consists of two modules. Optionally, the downstream module could be complemented by an end cap of vertical planes (see figure 4.2) to improve the performance for non-contained muons from the CNGS beam (see section 6). The total mass of the detector exceeds 34 kt. The sensitive elements provide two coordinates with a pitch of 2.8 cm, and a time resolution of 2 ns.

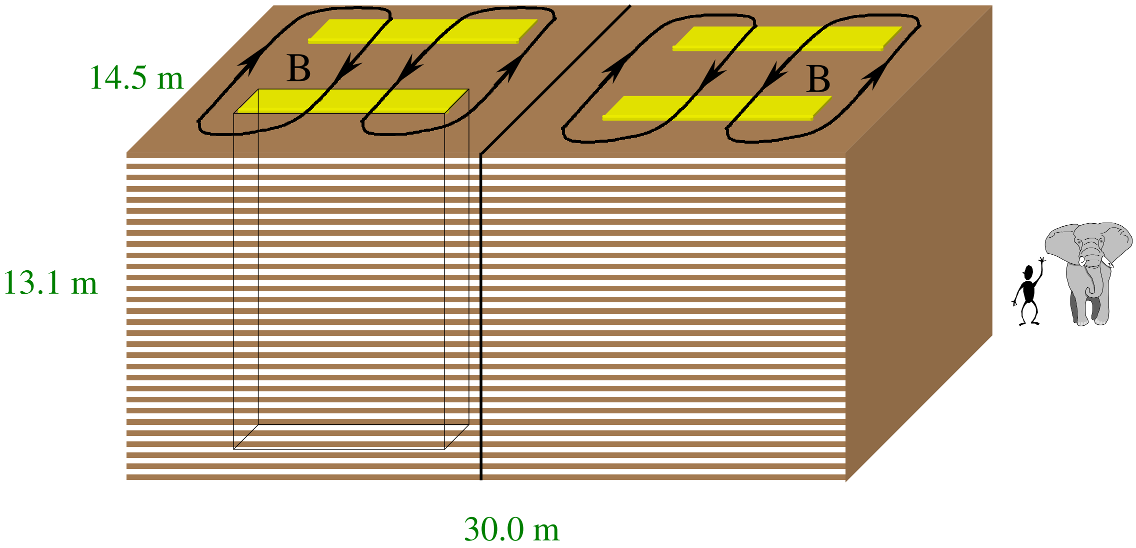

Figure 4.1: Schematic view of the MONOLITH Detector. The arrangement of the magnetic field is also shown.

A detector option with only vertical planes had also been considered, yielding similar performance (see section 5.6). The horizontal plane option was chosen because it was both technically easier to realize and more efficient in rejecting the background from downward going cosmic ray muons. Nevertheless, an additional external veto made of scintillator planes has recently been added to the design (see section 4.3). It will provide redundancy in this background rejection, and might eventually be used to increase the effective fiducial volume.

Extensive studies, including power consumption and cost, have been performed for iron magnetization. A magnetic induction of about 1.2–1.4 T turned out to be affordable at reasonable cost and power consumption.

Glass Spark Counters (i.e. Glass RPC) have been chosen as active detector elements.

Their performance and feasibility will be discussed in section 4.5.

The alternative option of scintillator bars with wave length shifter (WLS) read-out [63] was not pursued further due to the difficulty to achieve the required timing performance for 12 or 15 m long scintillator bars at reasonable cost.

The full detector is 30.0 m long, 14.5 m wide and 13.1 m high, which is consistent with construction and operation in the Gran Sasso Hall C. It is also possible to configure the detector for installation in Hall B. Specific studies will be performed if requested by committees. With the envisaged modular structure, we anticipate that the first module could be ready for operation 4 years after experiment approval.

4.3 External veto counters

The whole MONOLITH detector, as described in section 4.2, is foreseen to be surrounded by an external layer of scintillation counters. The function of these external "veto"-counters is twofold:

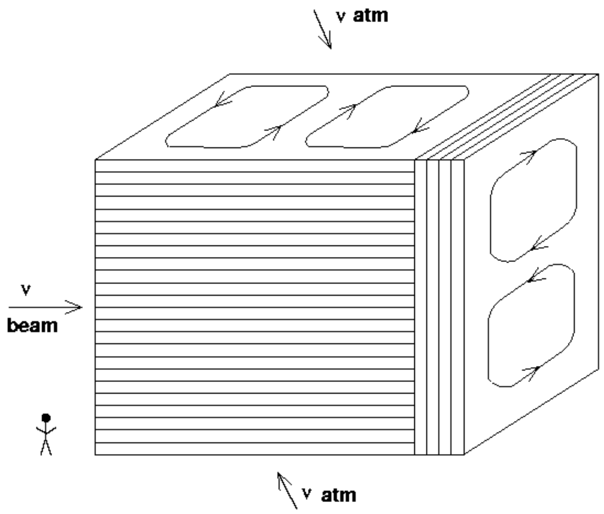

Figure 4.2: Sketch of the MONOLITH downstream module. The arrangement of the end cap option is shown.

- to recognize muons that enter from outside the detector to reduce the corresponding background of muons of cosmic radiation and/or increase the useful fiducial volume.
- to contribute to the distinction of the contained and semi-contained event samples, and therefore to the optimization of the corresponding cuts.

The counters will therefore be used as a veto device for contained events and as an additional detection device for semi-contained events. The front and back faces can also be used to obtain an online measurement of the CNGS beam intensity via the rate of muons from both MONOLITH and the preceding rock.

Unless explicitly stated otherwise, all physics analyses presented in this document have been performed *without* using the veto information. The veto therefore provides partially redundant *additional* information which allows to further reduce the background, cross-check detector efficiencies, and increase the useful fiducial mass.

Most of the events recorded in MONOLITH will be caused by cosmic ray muons. The large majority of these muons cross the complete detector, or at least a large part of it, and are effortlessly identified using the tracking and timing information of the GSC's. Occasionally, some muons enter the detector without being recognized by the outmost GSC layers due to the non-perfect efficiency and because of geometrical gaps. Such muons travel a certain distance in the detector before they are detected and could be mistaken for downward neutrino-events. This background can be reduced to an almost negligible level by imposing certain fiducial cuts.

As an alternative way to eliminate this remaining background, the whole detector (except some part of the floor) is surrounded by a hermetic layer of scintillation counters. These counters have to fulfill the following requirements:

- detection probability of more than 99% for minimum-ionizing particles (including geometrical efficiency).

- random coincidences with neutrino events (spatial and temporal misassignment) at most in the per mille range.
- a direct contribution to the time-of-flight measurement is not necessary (upward/downward event discrimination is obtained from the GSC's).

In addition to its good performance concerning efficiency and hermeticity, the scintillator technology has been chosen to allow independent cross-checks of detector efficiencies.

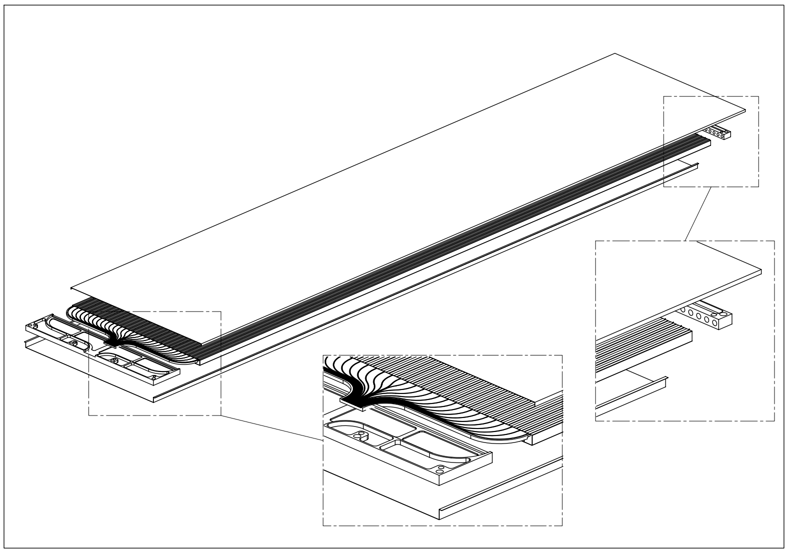

Figure 4.3: Basic scintillation counter element [64].

The corresponding detector design is not yet fully completed. The current preliminary design is based on scintillator elements similar to the ones which have been developed by the I216/P311 collaboration [64] (figure 4.3). Each basic element (extruded scintillator) of 51×4 m^2 is read out by 32 wavelength-shifting fibers, whose light is bundled and fed into a single photo-tube. The time resolution is of order 10 ns. In contrast to I216, the scintillator plane can be continuous. About 750 of such elements and the same number of TDC channels are necessary to cover the whole detector, including an overlap of neighboring counters in critical detector regions. To allow access to the GSC electronics, the counters are foreseen to be mounted on mobile supports on the long sides of the detector.

4.4 Magnetization of the iron planes

A layout in which each field line lays entirely inside an individual iron plane has been chosen in order to avoid huge power consumption and stray field. As shown in figure 4.1, to obtain this, a *vertical* slot crossing all the stack is needed, through which the currents generating the field have to pass. This layout allows to create a field of the order of $1.2 \div 1.4$ T, with a power consumption not exceeding 200 kW and a cost of the windings not exceeding 500 kEuro. Other layout which were also considered in [63] did not offer any significant advantages over the chosen option.

4.5 Glass Spark Counters

4.5.1 Basic structure and operation

Taking into account the overall dimensions of the apparatus outlined in section 4.2 (125 planes 30.0 m long and 14.5 m wide) the total active detector area is $\sim$ 54000 m^2. The large active area requires a low cost detector, suitable for a fast mass production.

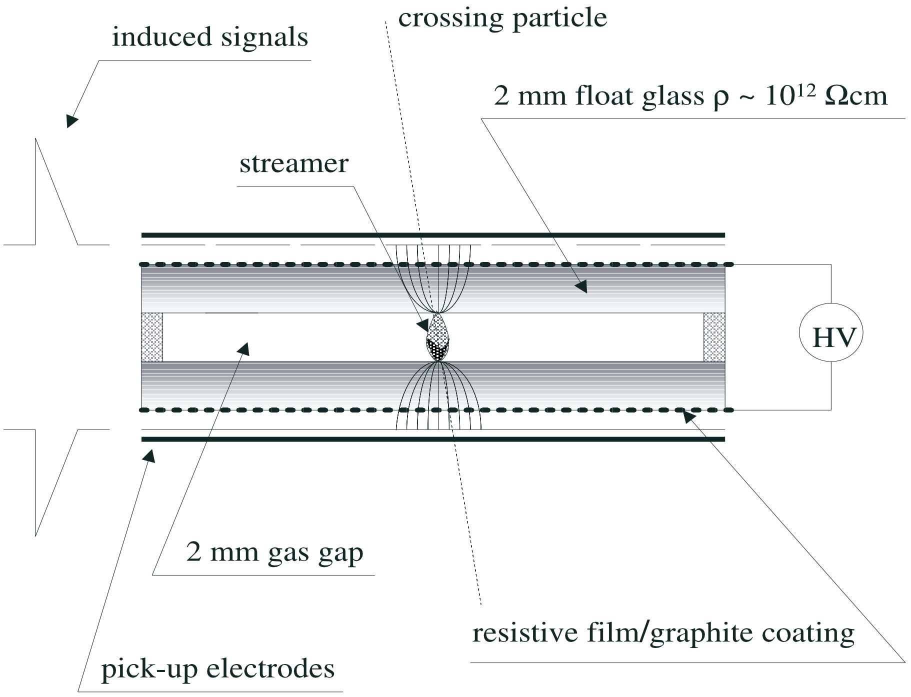

Figure 4.4: GSC: principle of operation.

For these reasons Glass Spark Counters (GSC) [65, 66, 67, 68, 69, 70, 71] have been chosen as active elements. They are derived from resistive-plate chambers by substituting the bakalite by commercial float glass of high resistivity (10^{12} Ωcm); for this reason they are sometimes called Glass RPC. Moreover they provide a timing of the order of 1-2 ns, and therefore excellent up-down discrimination of muons.

The GSC (figure 4.4) is a gaseous detector composed by two parallel electrodes made of glass with a volume resistivity of about 10^{12} Ωcm. The two electrodes, 2 mm thick, are kept 2 mm apart by means of suitable spacers. The gap between the two glass electrodes defines the gas volume where the particle detection occurs. Under particular gas mixture and electric field configurations (typically $\sim$48% Argon + $\sim$4% isobutane + $\sim$48% R134A and $\sim$4$\div$5 kV/mm) the detector is operated in spark mode. Typical signal amplitudes of the order of 100$\div$200 mV/50 Ω are observed, corresponding to a charge of about 100$\div$200 pC (depending on the intensity of the applied electric field).

The use of highly resistive material as electrodes ensures that the spark discharges just a limited area around the spark location. The time to recover the electric field, depending on the electrode resistivity ($\tau \sim \rho\varepsilon$, where ρ is the glass volume resistivity and ε is its dielectric constant), avoids self-sustaining sparking.

The read-out of the detector is performed with external pick-up electrodes, allowing a bi-dimensional localization of the crossing particles together with time information.

The details of the current GSC design and the proposed arrangement for the apparatus plane will be discussed in the next section.

4.5.2 GSC and apparatus design

A sketch of the GSC design is shown in figure 4.5 [70]. It consists of a couple of float glass

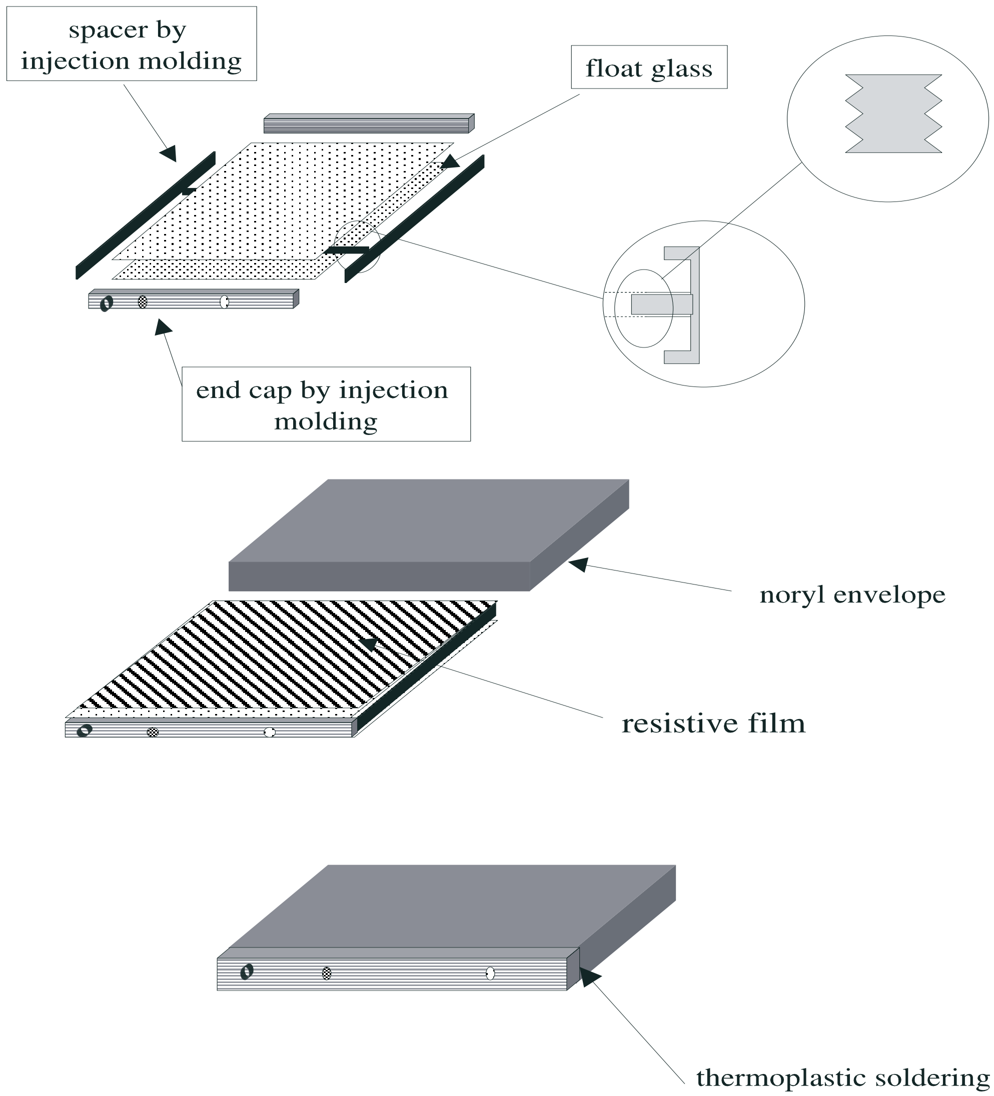

Figure 4.5: Schematic view of the GSC.

electrodes. The 2 mm distance between the electrodes is ensured by NORYL spacers clamping the edges of the glass plates. These spacers sustain both electrodes, ensuring a gap tolerance at the level of a few microns, for uniform working conditions in a such large apparatus. The high voltage is applied to the electrodes by means of resistive adhesive film with a surface resistivity of about 200 kΩ/square. The detector is inserted into an extruded NORYL envelope, that ensures the gas containment. In such a way a possible variation of gas pressure does not change the distance between the electrodes. The HV connections to the resistive film are located in one of the two end caps that close the GSC module. External pick-up strips (not shown in figure 4.5) are used to detect the induced pulses. All the materials used are commercially available, while the manpower is essentially due to film application on the glass surface and to the detector module assembling. This detector is conceived for the use in a underground laboratory. In fact all the materials are halogen free (PVC has been replaced by NORYL), the gas mixture is ecological and not flammable (Freon has been replaced by R134A, the isobutane percentage is well below the flammability level). During the last 10 years the performance, life-time and reliability of the GSC detector has been extensively studied. GSCs have been successfully employed in the K_L and muon detection subsystem (KLM) of the BELLE experiment. [71].

Further detailed studies have been also performed on the glass properties [68], [69] and on the detector design optimization and engineering in order to make its construction easy and fast [70].

Extended GSC performance tests have been performed using an 8 t prototype. The corresponding results are reported in section 4.8.

For the MONOLITH apparatus (figure 4.6) the GSCs will be equipped with X and Y pick-up strip electrodes, both with a pitch of $\sim$ 3 cm (2.8 cm), mounted on the opposite side of the detector planes. The pulses are induced on the strips and then discriminated by the electronics directly connected on the strip ends. The electronics should also provide a fast discriminated signal for timing purposes.

This type of readout system will provide a three-dimensional tracking of particles inside the apparatus with a time resolution of $\sim$ 1 ns and a spatial accuracy of $\sim$ 1 cm on both views.

In figure 4.6 the GSC plane arrangement is shown. The detector plane insertion is along the Y direction. The mechanical construction of the iron structure should not interfere with the detector installation. The dimension of the underground hall permits a maximal length of the detector module of $\sim$ 1.8 m to allow module insertion. In this case, each detector plane is composed by 16 *roads*, 1.80 m wide and 14.4 m long, realized with 8 *plate units* 1.80 m long (figure 4.6).

4.6 Gas System

The gas distribution system will be a recycling system that must ensure a flux corresponding to two detector volumes per day, i.e. 216,000 liters/day. The premixed gas (Argon 48%, Isobutane 4%, Freon R134A 48%), will circulate inside stainless steel tubes electrically cleaned. The whole apparatus will be divided into 16 x 10 = 160 detector groups, each of them being fluxed separately. The gas flow velocity is controlled for each group by means of a mass flow meter. The pressure difference of 1.8 bar between inlet and outlet manifold necessary to ensure a regular flow in each detector group will be ensured with a gas turbine. All systems will be controlled via

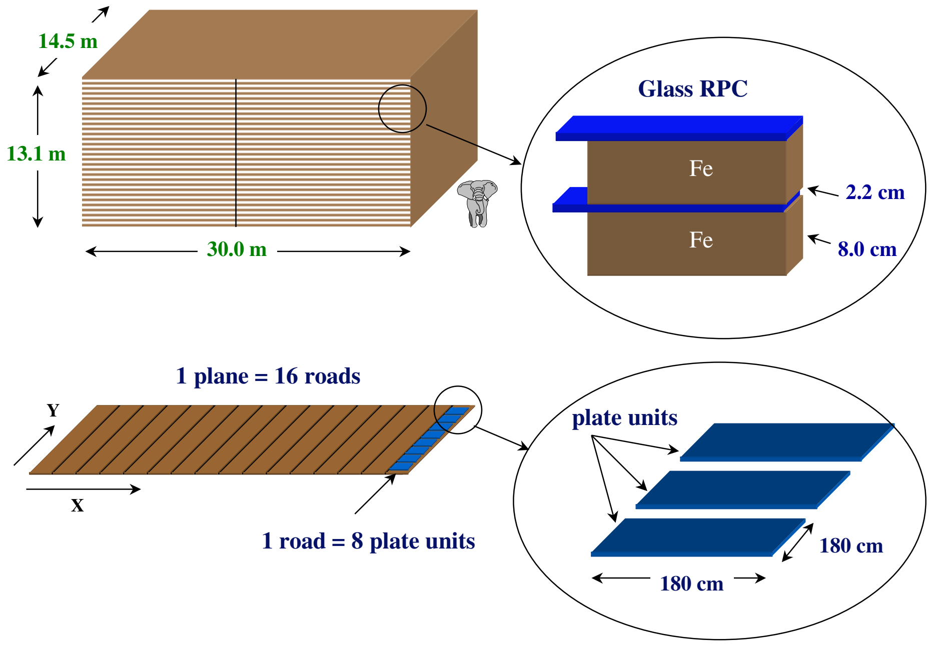

Figure 4.6: Schematic view of the MONOLITH apparatus.

a PC computer. The gas mixture will be fixed in the inlet stage by means of mass flow meters, and checked in the outlet stage by means of isobutane and freon gas analyzers. Humidity will also be measured. At the start of operations the air will be removed from each detector group and compressed into bottles to be emptied in open air.

4.7 The trigger and the DAQ system

The GSC signals are read out digitally. In addition, the signals of 16 or more channels are summed and sent to a TDC via a discriminator. These discriminator signals are also available for trigger purposes. As every spark provides both an x- and y-coordinate, the processing of only one coordinate is sufficient for triggering. This leads to about 9000 trigger channels for the flat cable design. A VME trigger board processes groups of 120 of these trigger channels with a programmable local trigger logic. This results in 76 VME boards for all trigger channels.

The logic allows to trigger on certain track patterns, such as 2 or 3 hit layers out of 5 consecutive layers. This results in a trigger efficiency near 100% for the relevant atmospheric neutrino events (energy $>$ 1.5 GeV). Through a combination of signals from different trigger boards on an additional logic level, a global multiplicity trigger is also possible. The signals of the veto counters are read out by TDC's and are also available for trigger purposes.

The expected trigger rate (mainly originating from cosmic ray muons and random coincidences of radioactive decays) is expected to be much less than 1 Hz. The trigger initiates the readout of the digital and TDC information, which is collected and further processed via VME

CPU modules. The complete events are then fed into an online computer, which performs a preliminary event reconstruction. At this "2nd level trigger" stage, events can be filtered and/or distributed to several output streams.

The MONOLITH DAQ system will be VME based.

DAQ electronics will be located on the top of the detector, along the hall axis in 4 points (spaced $\sim$ 7.5 m), two for each detector module.

Since VME crates and their read-out are the major DAQ cost, a big effort has to be done to minimize their number: STAS (control and readout) units serving 32 digital chains will be developed (the current commercial STASs serve 8 digital chains) and 64 chs/unit TDC modules will be used.

In this way every DAQ station will provide the readout of 4 roads (16 digital chains and 32 TDC channels) for all the 120 detector layers. The 60 STAS and TDC modules needed will be stored in 6 crates (3 9U and 3 6U). Every crate will serve 40 layers. In every DAQ point 2 VME crates devoted to trigger and slow control systems are foreseen.

Front end data read-out will be performed using Motorola MVME CPUs. To minimize software cost, the Linux option, as operating system of VME embedded CPUs, will be investigated.

Disk-less CPU booting, event building and monitoring will be performed using a Linux PC for each DAQ station.

4.8 Detector performance

The measurements reported here have been performed with a prototype made of 20 iron planes (100×100 cm^2) 5 cm thick, 2 cm apart, interleaved with 20 detector planes.

The readout system, developed at the LNGS, is based on the use of halogen-free flat cables acting as pick-up strips. The strips are coupled to the detector plane and are referred to ground by means of a 100×100 cm^2 FR4 vetronite foil acting as a shield. The other side of the detector plane faces a 100×100 cm^2 aluminum sheet referred to ground. The digital readout system of the ALEPH hadron calorimeter has been used for the event pattern in one view. The flat cables are connected on one side to the front end discriminators to obtain 96 1 cm wide strips. The other side is connected to cards developed at LNGS that perform charge and time measurements. The Glass RPCs are operated with an Argon + isobutane + R134A $=$ 48% $+$ 4% $+$ 48% gas mixture and the applied voltage is 8.2 kV. The above described prototype module has been exposed on CERN PS T7 beam and used for a test on up/down discrimination. Results are reported in the following sections and in ref. [72], [73].

4.8.1 The CERN PS beam test

A test of the MONOLITH prototype has been performed on the CERN PS T7 beam facility to study the hadronic energy resolution and the reconstruction capability of the shower direction. This beam provides particles (mainly pions) in the range between 2 and 10 GeV. Figure 4.7 shows the typical pattern for a 4 GeV pion taken from the online event display.

The shower energy can be measured by hit counting, because the hit number is proportional to the total track length and therefore to the energy released. The mean number of hits produced

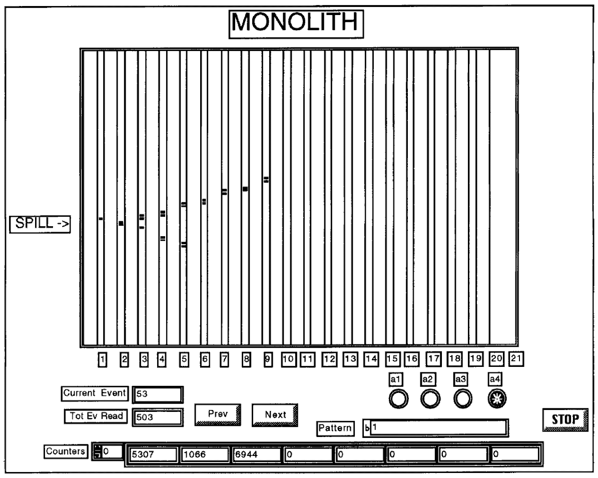

Figure 4.7: 4 GeV pion interacting in the 8 ton calorimeter prototype.

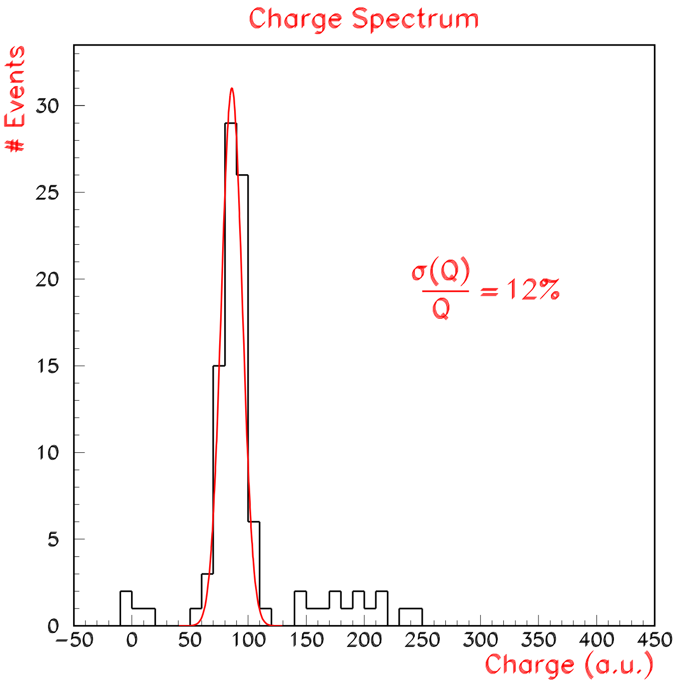

Figure 4.8: Induced charge distribution for 10 GeV muons crossing a plane.

by pions as a function of the energy is given in figure 4.9; no saturation effects were found in the investigated energy range and a calibration value of 4.4 hits/GeV was obtained. As shown in figure 4.10 the energy resolution can be parameterized as $68\%/\sqrt{\mathrm{E(GeV)}} + 2\%$. The shower resolution for different sampling densities was obtained offline by appropriately selecting the detector planes. Figure 4.11 shows that the resolution is better than $100\%/\sqrt{\mathrm{E(GeV)}}$ up to a shower sampling of 20 cm of iron. In the MONOLITH detector, 20 cm sampling corresponds to

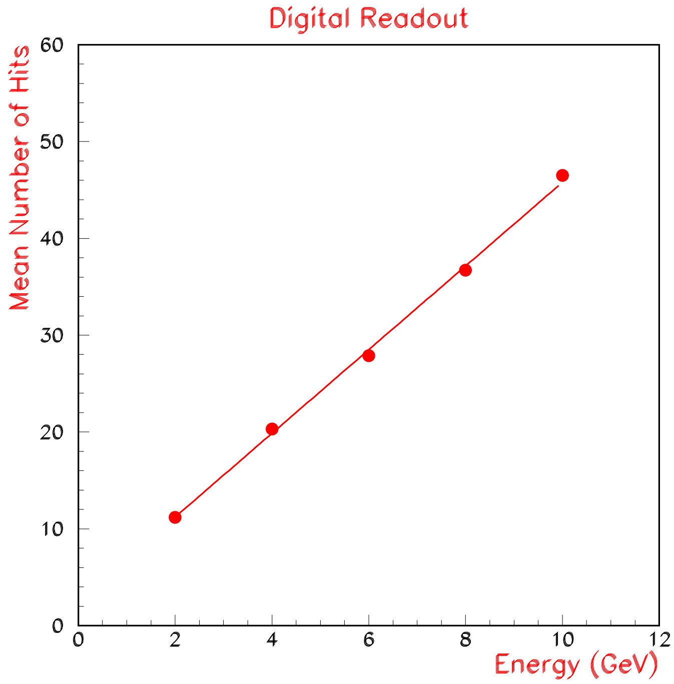

Figure 4.9: Digital response for pions.

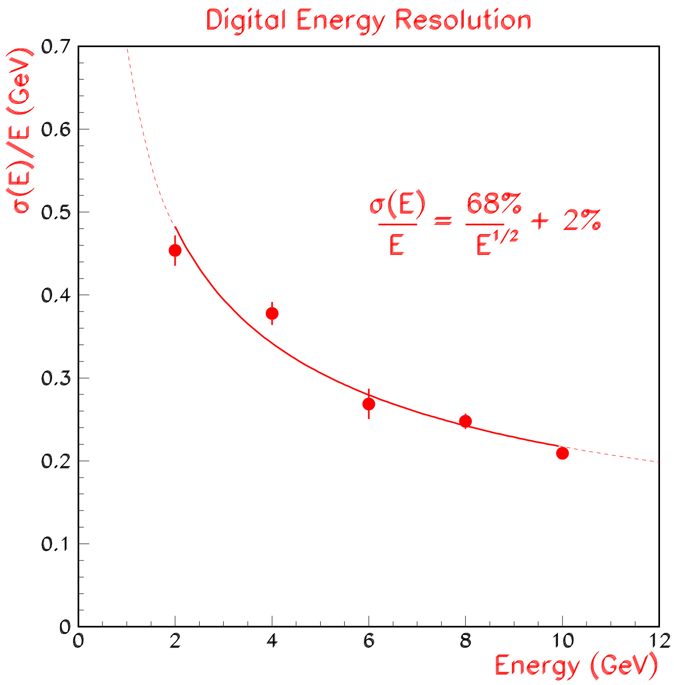

Figure 4.10: Digital resolution for pions.

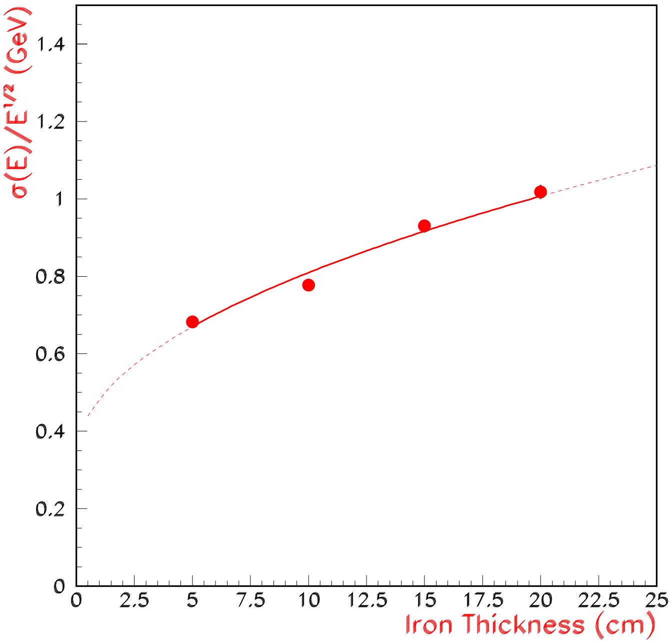

Figure 4.11: Digital hadronic resolution as a function of the iron thickness.

showers developing at a 66^0 zenith angle.

It is worth observing that, in a digital calorimeter, a good linearity and resolution is possible only if the probability to have more than one track on the same strip is negligible. A high track density (due to high energy and/or e.m showers) determines a loss of linearity with the worsening of the resolution. The same effect occurs when using wide pick-up strips.
For what concerns the analog readout, the total charge is proportional to the total number of streamers and therefore to the total track length. Thus the charge collected can be used to measure the energy released by the shower. The energy resolution obtained with the analog readout follows a $96\%/\sqrt{\mathrm{E(GeV)}}$ law. It is worse than expected mainly because the analog method strongly depends on the precision of the coupling between pick-up and detector planes, while the intrinsic charge spread of the single streamer (see figure 4.8) gives a negligible effect on the resolution.
In conclusion, the digital readout is weakly dependent on the working conditions, but it suffers effects of saturation at high track density. On the contrary, the analog readout is linear up to higher energies, but presents more difficulties when used in a large apparatus (gas mixture stability, precision in construction, etc.).

4.8.2 The test for up/down discrimination

A second test was performed on the prototype at the Laboratori Nazionali del Gran Sasso to study its time of flight performances. Vertical through-going muons are selected with two

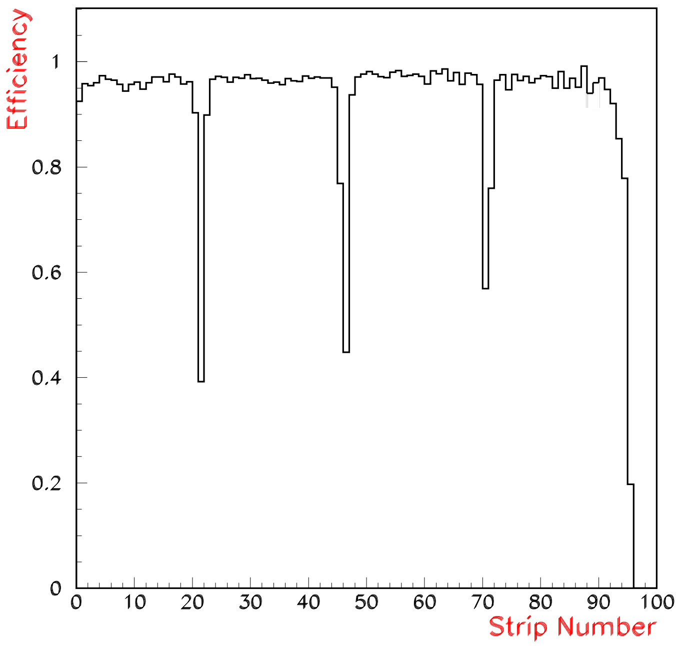

Figure 4.12: Efficiency of a plane as a function of the strip number.

scintillators defining the acquisition trigger. Events are reconstructed in one view by using 1 cm pick up strips. The prompt signal of the even planes is recorded for the time-of-flight measurement, while all planes are used for tracking the crossing particles. Results of one month of data taking are reported.

The efficiency of one plane as a function of the strip position, measured with the digital cards, is shown in figure 4.12. The efficiency along the muon tracks has been calculated considering hits within 3 cm from the straight line fit. The drop every 25 cm is due to the geometrical dead zone between adjacent detectors. The dead area inferred from the plot is about 7 mm wide, in agreement with the mechanical characteristics of the Glass RPC prototypes (glass width is 243 mm, while the envelope one is 250 mm). Far from the chamber edges, the measured efficiency is about 97%, including the $\approx$ 1% geometrical inefficiency due to the spacer sticks. The average plane efficiency is thus 94%. We are confident that this value can be increased by improving the mechanical tolerance of detector components and readout electronics. To measure the spatial resolution we used the distance between the hit position (e.g. the center of the cluster) and the muon impact point reconstructed with a straight line fit. The resolution has been calculated for even planes, while odd planes are used for track reconstruction. The obtained distribution is reported in figure 4.13; the Gaussian fit has a σ resolution of 3 mm. The tails are mainly due to multiple scattering of the crossing cosmic ray muons.

Figure 4.14 shows the time difference distribution of the signals coming from two planes crossed by the same particle. Assuming that the two planes have the same time resolution, the RMS of each plane turns out to be 1.3 ns. The distribution is not Gaussian because of the tails due

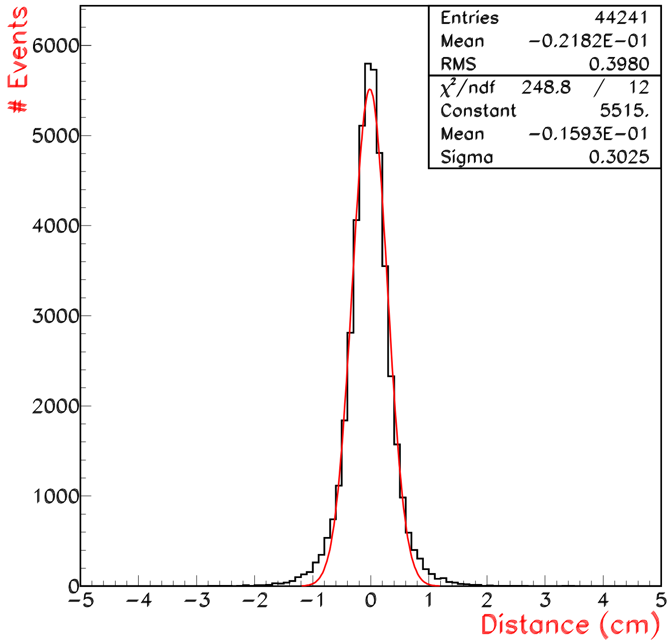

Figure 4.13: Distribution of the distance between the center of the cluster in the even planes and the track reconstructed with the odd planes.

to the delayed signals, which make up about 10% of the total events. All planes show the same time resolution, stable over one month measurement period. Measurements to test long term stability are in progress.

During the test a first estimate of the up/down discrimination on 4 m long tracks (the minimum length required for partly-contained muons in the physics analysis) was obtained as follows. An algorithm was developed which discards *bad hits* and fits the time measurements of each plane with a straight line in the t-z plane:

$$t(z) = \frac{1}{\beta}z + c \qquad z = \textit{vertical coordinate of plane}, \qquad \beta = v/c$$

With our sample of about 30000 cosmic rays crossing the whole prototype for a total length of 1.4 m, we obtained a $1/\beta$ distribution with 0.28 % of the events in the negative region. The extrapolation to a track length of 4.0 m produces no events in the negative $1/\beta$ region, as shown in figure 4.15.

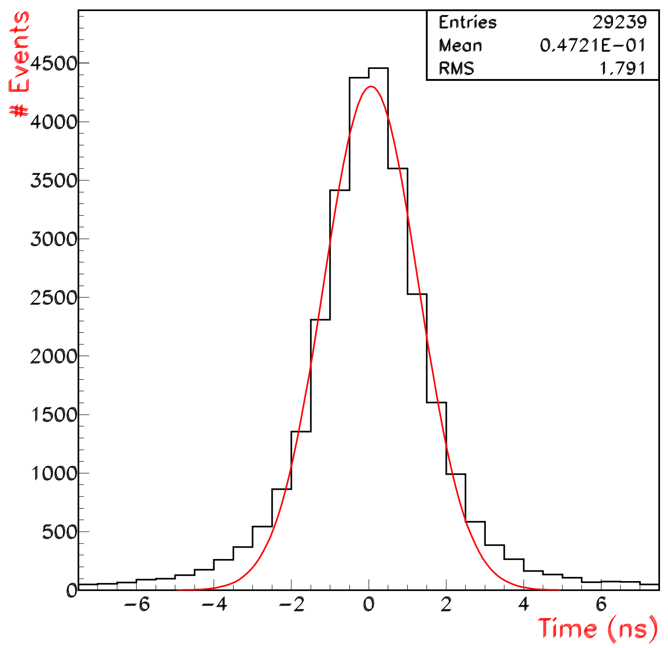

Figure 4.14: Distribution of the time difference between two planes.

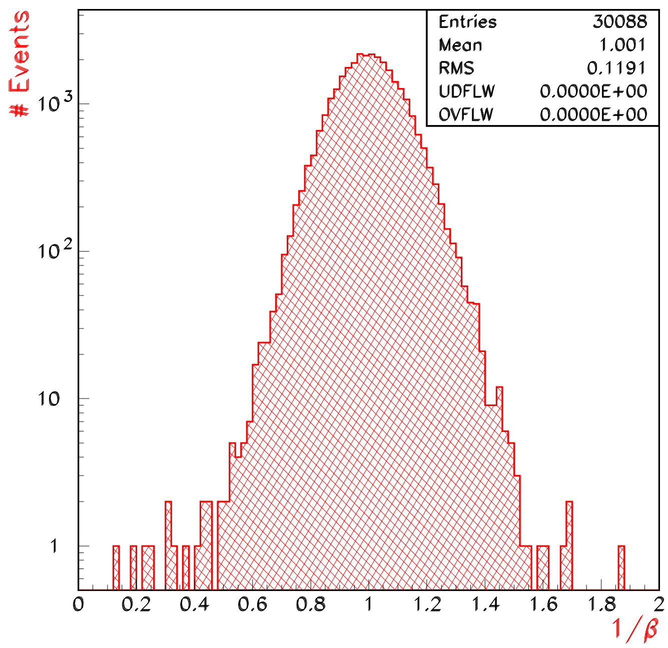

Figure 4.15: $1/\beta$ distribution for tracks 4.0 m long.

Chapter 5

Physics with atmospheric neutrinos

5.1 Introduction

In this Chapter, the sensitivity of MONOLITH to oscillations using atmospheric neutrinos is discussed. We shall give results on the MONOLITH capability to detect an oscillation pattern, discriminate alternative hypotheses to oscillations and measure oscillation parameters. Alternative detector geometry, based on vertical iron planes, is considered as well as a staged approach to the final detector. Performances of an initial 12 kt module are presented.

5.2 Detector simulation

The simulations described in this chapter were performed before some of the technical details of the detector were finally adjusted (changes at the level of a few %, e.g. exact external dimensions). The simulated detector is therefore at slight variance with respect to chapter 4. These small differences result in negligible effects on the performance.

The simulation of the detector is based on the GEANT package [74]. A detailed description of the detector geometry, of the detector media and of the the magnetic field configuration has been implemented. The GEANT package has then been used to follow particle propagation through and interactions with the detector media. An approximate description of the digitisation process is implemented, based on the present knowledge of the behaviour of the active elements of the detector (Glass Spark Chambers). In the experiment simulation, the detector consists of a stack of 121 horizontal iron planes 8 cm thick and 15×30 m^2 surface, interleaved by 120 planes of sensitive elements. The detector is divided in two super-modules of 15×15 m^2 surface, resulting in a mass of about 17 kt each. The iron planes of each super-module are magnetised as shown schematically in figure 5.1. A detailed description of the field map is implemented in the simulation. Simulations at different field strength have been performed. The results discussed hereafter are referred to an average magnetic induction of 1.3 T.

The sensitive elements for tracking and timing (Glass Spark Chambers) are assumed to be housed in a 20 mm gap between the iron planes. The GSC are described as made of 18 mm of material with an average density of 1 g/cm^3 (water) and a gas gap of 2 mm (active element) in their center. Orthogonal readout strips of 30 mm pitch placed on both sides of the chambers provide the X and Y coordinates of the event, the Z coordinate being identified by the layer

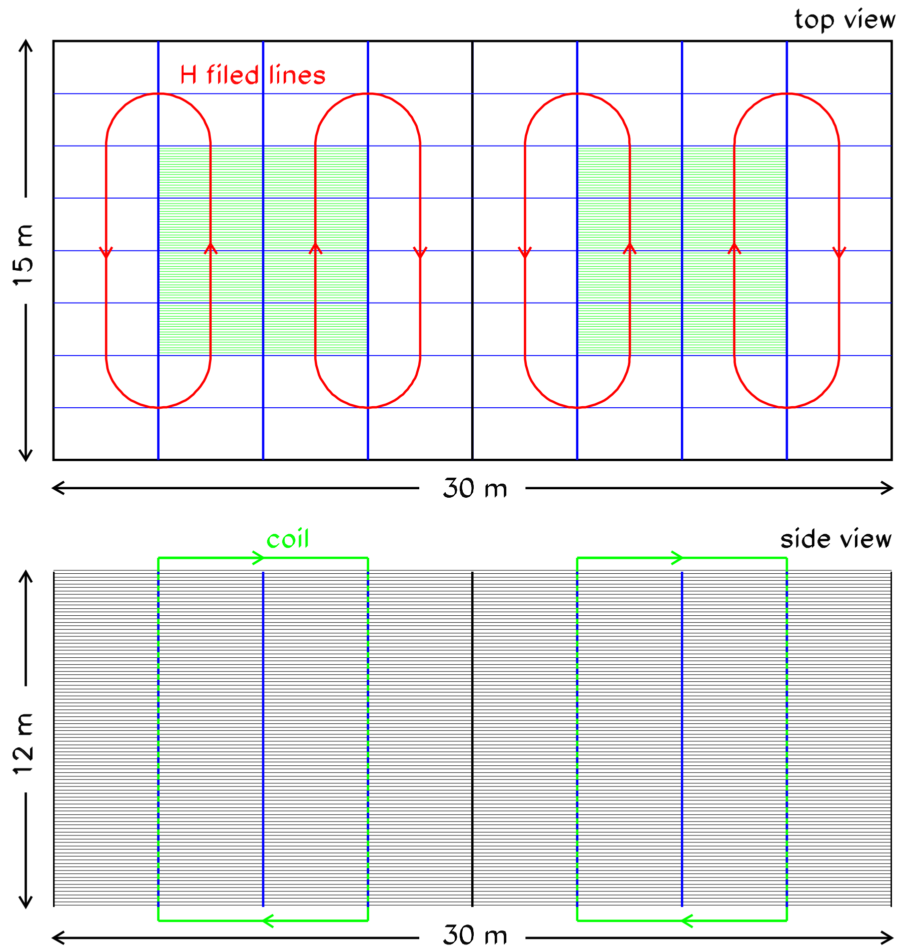

Figure 5.1: Simplified view of MONOLITH showing the magnetisation scheme: the shaded area in the top view represents the coil and lines represent dead zones due to iron supports of layers, coil housings and chamber modularity (see text).

number[1]. The X and Y strips are supposed to be continuous in each super-module all along the X (15 m) and Y (15+15 m) directions, without any longitudinal segmentation. This choice corresponds to the most conservative option among the ones considered for signal readout.

The GSC are assumed to be evenly efficient. They are described by a lattice of 3×3 cm^2 elementary cells, corresponding to the readout pitch of the detector, in which sparks can be generated by ionising tracks. The signal induced on the readout strips by these sparks is collected assuming, as a rough approximation, that only the strips in front of the spark are fired and that there is no induction on the nearby strips. A digital readout of the strips is considered.

No pattern recognition is applied yet and muon hits are distinguished from the hadronic ones according to the simulation truth.

The time response of the detector is simulated as follows: the arrival time of each individual spark is smeared according to a set of resolution functions, giving a conservative representation of the results obtained in the test of the Baby-Monolith prototype on cosmic rays (see figure 5.2). These resolution functions have been measured in Baby-Monolith after selection of almost vertical muons and are therefore suited to describe the time spread of single sparks. The time distribution sampled is randomly chosen and the relative offset between the different TDC channels is calibrated to zero in the simulation. This is achievable in MONOLITH using cosmic muons crossing the detector. It is moreover assumed that only the time information relative to the hit with the earliest arrival time (including resolution effects) is recorded in each layer, i.e. only one TDC channel per layer is assumed in the simulation (120 TDC channels in total).

5.3 Event reconstruction

5.3.1 Muon reconstruction

A new routine for the momentum fit from track curvature, based on the GEANE package, has been adopted in the analysis of atmospheric neutrino simulated data. This routine is somewhat more efficient, while having comparable resolutions with respect to the one used in the Proposal [61]. It allows also an improvement in the reconstruction of the muon direction, both for contained and partially-contained events. No pattern recognition is applied yet and muon hits are taken from the simulation truth. At the reconstruction stage, the muon direction is obtained by a best fit procedure to the muon track, which accounts for effects of detector resolution, multiple scattering, energy loss along the track and magnetic field. The muon energy is mainly determined by range for stopping muons and by track curvature for outgoing muons. The muon direction, used to estimate the neutrino direction and pathlenght, is determined by the track fit both for contained and semi-contained events.

The procedure is based on the Kalman fiter technique [75]. The Kalman Filter is an algorithm used to analyze discrete linear dynamic systems and it has been proposed as an optimal track fitting method [76]. The first stage of the reconstruction of muon momentum in the magnetic field, is to define a *candidate track*, that is a collection of hits in the two projections xz and yz ordered along the z-axis (vertical). Each projection is modeled through a polinomial fit of order n, with $1 < n < 7$ depending on the number of hits in the projection. This track model is used

[1] In the reference system adopted here, Y is along the Hall axis.

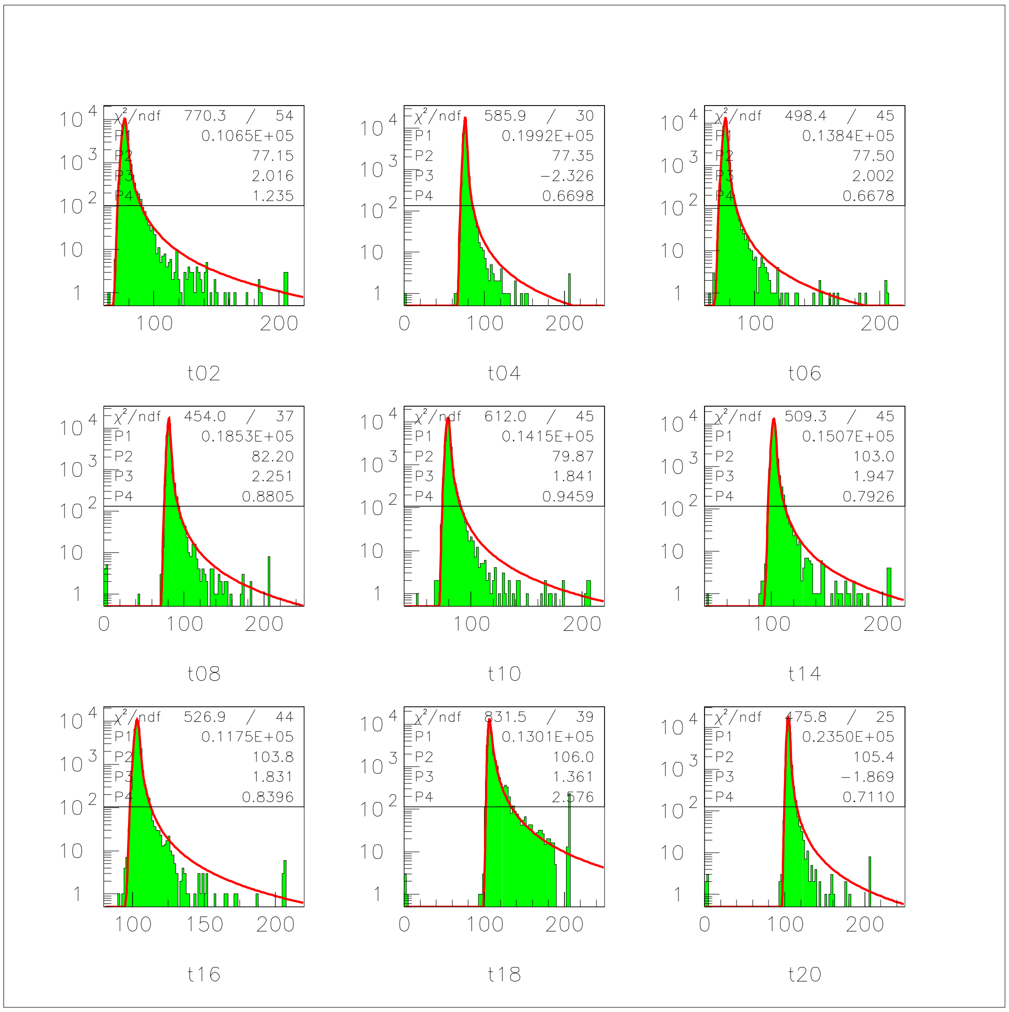

Figure 5.2: Resolution functions measured with the Baby-Monolith prototype (histograms) and sampled in the simulation (continuous lines). The continuous lines are best-fits to data assuming a Gauss distribution on the left sideof the peak and a Cauchy on the right side: P3 (P4) is the sigma (HWHM) of the Gauss (Cauchy) distribution in nanoseconds. The relative offset in the TDC was calibrated to zero in the simulation.

to get the initial starting track directions dx/dz and dy/dz. These, together with the first hit x and y coordinates and a rough momentum estimate using the range, are the input to the track fit. Two tracking are performed on a candidate track: the first starts from the muon hit closer to the interaction point and follows the track up the last hit. The track parameters fitted at the end track point are then used as new starting values for a backtracking, which now proceeds to the muon hit closer to the vertex. The fit parameters (the two coordinates x and y, the two derivatives dx/dz and dy/dz and the signed inverse momentum $K = q/P$, with q = ±1) are therefore provided in the innermost point, closer to the interaction vertex. The average tracking in the magnetic field and covariance error matrix propagation are done using GEANE [93], a tool that allows an interface with the GEANT description of the geometry and the properties of the media and materials of the apparatus.

The optimisation of the track-fitting procedure is still in progress. In particular, no special treatment is yet implemented for tracks bent by the magnetic field to cross more than once the same layer. This mainly occurs for low-energy muons near the horizon, which have their momentum underestimated by the present track-fitting procedure. However, these muons are of marginal interest in the measurement of the oscillation pattern – and indeed mostly rejected in the anlysis of atmospheric neutrino events – since near the horizon and at small energies the L resolution is poor (see discussion in section 4.1). On the other hand, events induced by neutrinos from the CNGS beam are mainly developed along the horizontal direction and requires a special treatment. On these events, an approach to the track fitting similar to the one discussed here, but working on the zy and xy projections, has been introduced (see chapter 6 for details).

The energy resolution on the sample of stopping muons produced by ν_μ-CC interaction is on average better than 6%, with the sole quality request that the muon track span at least seven layers. With this same selection and the additional request – explained in section 5.4.2 – that the track length inside the calorimeter be larger than 4 m, the average resolution on outgoing muons is found to be $\sigma(1/p)/(1/p) \simeq 22\%$ at H = 1.3 T, essentially limited by multiple scattering in iron. An improved resolution is achieved at higher field intensity. The dependence of the momentum resolution on the track length, the pitch angle to the field and the strength of the magnetic induction has been found to agree with expectations.

From the analysis of the track curvature, the identification of the muon charge is possible. Due to the field configuration the charge identification is best achieved near the vertical direction, perpendicular to the field lines. On average 95% of the muons with a track length of at least seven layers have their charge correctly assigned. For very long tracks, as they occur for upward throughgoing muons (typically about 12 m) charge discrimination is better, and momenta can be measured up to several hundred GeV. For specific studies, charge discrimination could be significantly improved by selecting only unambigous candidates (see chapter 7).

The direction of the muon at the vertex, from which the neutrino direction is estimated, is reconstructed with an average resolution of about 10 mrad. This has a negligible effect on the resolution on the neutrino direction, which is limited by the μ-ν scattering angle.

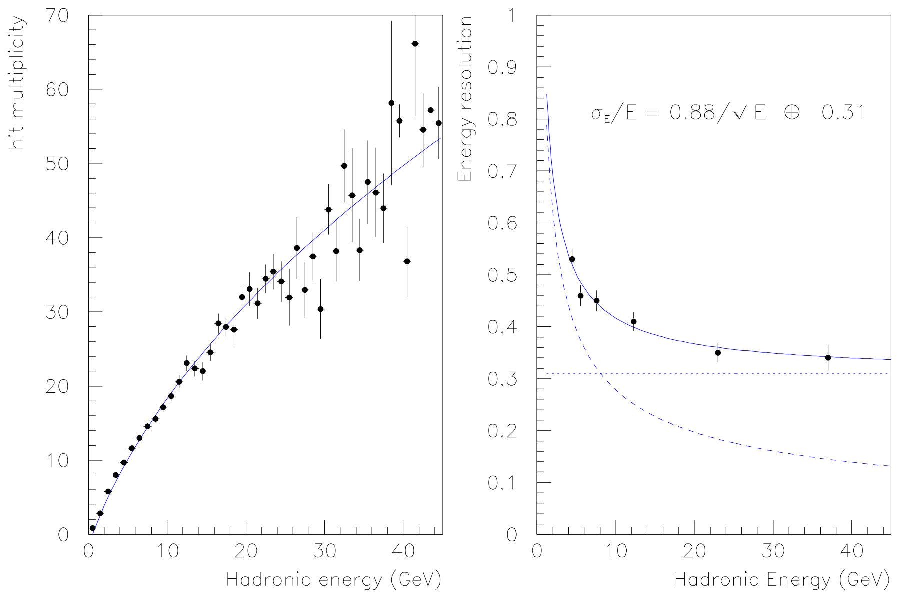

Figure 5.3: Hit multiplicity and energy resolution averaged over all shower directions as a function of the hadronic energy in atmospheric ν_μ-CC events.

5.3.2 Hadron reconstruction

The hadronic energy is estimated from the hit multiplicity in the calorimeter (digital information). The detector has a coarse hadronic energy resolution and, at low energies, a limited capability of reconstructing the hadronic energy flow. According to the simulation the dependence of the energy resolution on the hadronic energy can be parametrised as $\sigma(E)/E = 90\%/\sqrt{E\ (\mathrm{GeV})} \oplus 30\%$, averaged over all shower directions. This is shown in figure 5.3, together with the calibration curve of the hadronic energy response obtained form a sample of simulated neutrino events. As explained by equation (4.2) of Chapter 4 and discussed in the next section, the overall resolution on the neutrino energy, which enters in the measurement of the L/E and is generally dominated by the fluctuations in the hadronic shower, can be controlled by proper selection criteria, related to the in-elasticity of the event.

The reliability of this simulation of the MONOLITH response to hadrons depends on the description of hadronic interactions embodied in the GEANT package and on the assumption made in the description of the digitisation at the readout stage. This is being studied by comparing the results on hadronic energy resolution obtained with the MONOLITH prototype (Baby-Monolith) exposed to test beams during July/August 1999 (see section 4.8 and ref. [72]) to the results of a GEANT simulation of Baby-Monolith. A direct comparison to MONOLITH has not been possible since Baby-Monolith had a geometry somewhat different from MONOLITH: the 20 iron planes were 5 cm thick, the readout strip were only on one side of the chambers and had a pitch of 1 cm. A part form these differences in the detector layout, the simulation is run under the same assumptions adopted in the description of MONOLITH: a digital readout of the fired strips is considered, without induction on adjacent strips. Preliminary results show that the simulation of Baby-Monolith predicts a lower average multiplicity and a worse resolution than the ones measured with test beam data. These differences can be ascribed to the simplified model adopted, since induction on nearby strips is expected to linearise the detector response and improve resolution. An extrapolation to MONOLITH of the results of this comparison is not straightforward, due to the different geometries and readout-strip pitch of the two detectors. Nonetheless, this study corroborates our expectation that our neglecting of induction results in a conservative description of the energy response of MONOLITH to hadrons.

5.4 Atmospheric neutrino event studies

In this section, only the reconstruction and performance on ν_μ-CC events induced by atmospheric muon neutrinos inside MONOLITH is addressed. The MONOLITH capability to detect a clear oscillation pattern will rely on these events. The performance on the CNGS beam is addressed in Chapter 6, while the analysis on the ν-factory events is shown in Chapter 7.

5.4.1 Event generator

Neutrino interactions in iron have been kindly provided by G. Battistoni and P. Lipari: the differential distribution of the atmospheric neutrino fluxes at Gran Sasso is described by the Bartol model [77]; neutrino interactions are calculated with GRV94 parton distributions [78] with explicit inclusion of the contribution of quasi-elastic scattering and of single pion production to the neutrino cross-sections [79]. The height of production of neutrinos in the atmosphere, relevant in the evaluation of the L/E resolution is parameterised according to Bartol model calculation as in ref. [80].

The Bartol model, similarly to the simulation of Honda et al. [81] used by the SK collaboration, assumes that atmospheric neutrinos produced in the cascade process are collinear with the parent cosmic ray particle. This 1-D approach is expected to be valid in the limit of high energies. Recently, efforts in improving the calculations of atmospheric neutrino fluxes have been made by several authors, in particular introducing full 3-D calculations of the neutrino fluxes [82, 83]. These simulations show that the main features of the neutrino fluxes at high energy are reproduced by the collinear approximation. All the differences are mainly located near the horizon and below 3 GeV [84], where the acceptance of MONOLITH is purposely limited (see discussion in sections 4.1 and 5.4.2).

Besides these computational approximations, uncertainties on the neutrino fluxes are related to our ignorance of the hadronic interactions and of the spectra and compositions of primary cosmic rays. However, as we shall discuss in the next chapter, an up/down symmetry in the high-energy neutrino fluxes follows from geometry and isotropy of flux of parent cosmic rays [85, 86]. This is exploited by MONOLITH to perform measurements with the *near* and *far* source comparison technique, which is therefore to a large extent independent of predictions atmospheric neutrinos event rates.

5.4.2 ν_μ-CC interactions: selections and performance

The selection of a pure and "high resolution" sample of ν_μ-CC events induced by atmospheric neutrinos is crucial to enable MONOLITH to detect a clear oscillation pattern. Moreover, since oscillation parameters are not precisely known *a priori*, a unique set of event selections and a unique analysis method have been defined in order to make the oscillation pattern detectable for every possible experimental outcome.

In order to select a pure ν_μ charged current sample, only events with a reconstructed track corresponding to a muon of at least 1.5 GeV are retained in the analysis. This energy cut also ensures a good up/down symmetry in absence of oscillations. In order to reject – in a real experiment – the background due to incoming cosmic ray muons, a further selection requires the events to be either fully contained in a fiducial volume, corresponding to about 87% of the detector and defined by requiring no hits in the first/last 4 layers and no hits in the first/last 10 strips in X and Y, or to have a single outgoing track (muon) with a reconstructed range greater than 4 metres. For partially contained events, the requirement of a track length of at least 4 m corresponds to an up/down separation of about 10^{-6} for 2 ns timing resolution, which should be sufficient to guarantee the rejection of the residual cosmic muon background in the Gran Sasso laboratory. The combination of these selections results in efficiency of about 75% and practically energy independent, corresponding to an effective fiducial mass of about 26 kt. It reduces the contamination of ν_e and ν_μ-NC events in the sample of ν_μ-CC events below 1% and removes the bulk of cosmic muon background events. The remaining background is due to muons entering MONOLITH through detector dead zones and can be suppressed by specific selections based on the event topology and/or by an external veto.

In addition, in both fully and partially contained samples, the muon is required to hit at least seven layers. This selection has been optimised to guarantee a good performance of the reconstruction programme and remove muons very near to the horizon, whose L/E resolution is poor.

Further selections, based on the quality of the muon track fit and on event kinematics, are then applied in order to guarantee that the final sample has the required L/E resolution (better than 50% Full Width Half Maximum (FWHM)) over the whole L/E range. These selections have been tuned according to the discussion given in Chapter 4 (see equation 4.2) and essentially consist in a tight requirement on the estimated precision in the reconstruction of the incoming neutrino direction. At low muon energies only events of small in-elasticity and far from the horizon are retained, while for large muon energies deep-inelastic events even rather near to the horizon can be selected. For contained events, and given the detector characteristics, this is achieved by requiring $y \tan^2\theta_\nu < 0.75 E_\nu$, where $y = E_h/E_\nu$, θ_ν and E_ν are the interaction in-elasticity, the zenith angle and the energy of the neutrino. The sample of events with outgoing muons is populated by events of high energy, thus the only requirement is that the energy of the muon be estimated from the track fit with a relative error smaller than 30%. The MONOLITH performance on the events surviving these selections is shown in figure 5.4. The average angular resolution on the neutrino direction is about 11 (3.5) degrees for contained (semi-contained) events and is dominated by the μ–ν scattering angle; the energy resolution is around 20% (24%) for contained (semi-contained) events. The resulting L/E resolution is about 50% FWHM

FC events		PC events		Total
Event in the fiducial volume		Vertex in the fiducial volume		
.AND. $E_\mu > 1.5$ GeV	1317	*.AND.* muon range > 4 m	384	1701
Number of layers ≥ 7	1023	Number of layers ≥ 7	331	1354
$y \tan^2 \theta_\nu < 0.75 E_\nu$	931	$\Delta p/p \leq 30\%$	259	1190

Table 5.1: Expected number of downgoing ("un-oscillated") ν_μ-CC events in four years of MONOLITH exposure to atmospheric neutrinos. Event selections are discussed in the text.

in both samples, with an asymmetric tail, which should be ascribed to the nonlinear relation between L and θ_ν.

Altogether, these selections reduce the charged-current interaction rate of "unoscillated" down-going muon neutrinos to around 7.8 per kt y, about 20% of which is due to partially contained neutrino events. The impact of the magnetisation of MONOLITH, which allows to reconstruct events with an outgoing muon, is best evaluated from figure 5.5, showing the overall selection efficiency as a function of L/E. The gain in acceptance at small L/E is noteworthy: the magnetic field increases the MONOLITH efficiency by more than 50% in the region where the first semi-period of the oscillation is expected, according to the most recent Super-Kamiokande reports. The detection of the oscillation minimum and the precision on Δm^2 mainly rely on the available statistics in this region.

The event rate expected in MONOLITH and the effect of the selection criteria discussed are summarised in table 5.1 . A summary of the efficiencies and resolutions as a function of the neutrino energy is given in figure 5.6. MONOLITH will have an effective threshold on atmospheric ν_μ charged current events around 3 GeV and a practically constant efficiency of about 50% (including selection and fiducial cuts) up to high energies. The L/E resolution is independent of the neutrino energy and is dominated by the angular resolution on the neutrino direction at small neutrino energies and by the energy resolution at high energies.

By taking advantage of the timing capabilities of the sensitive detectors, the flight direction is determined in each event from a least-square fit of the timing in each layer versus the layer number. The up/down discrimination capability mostly rely on the muon hits and improves in events with long muon tracks. No attempt to filter hits not belonging to the muon track has been made, nor has the identification of the event vertex from the hadronic activity been tried yet. The up/down discrimination of this method is in excess of 95% at all neutrino energies, the residual confusion being due to events of low energy and near the horizon in which the muon track has a vertical extension comparable to the one of the hadronic shower. These latter events are easily resolved by hand scanning. Advances in pattern recognition will probably achieve this by automatic means. If not, the event sample is relatively small and it can be done by hand scanning. In the discussion of the MONOLITH sensitivity (see next chapter) a perfect up/down discrimination is assumed.

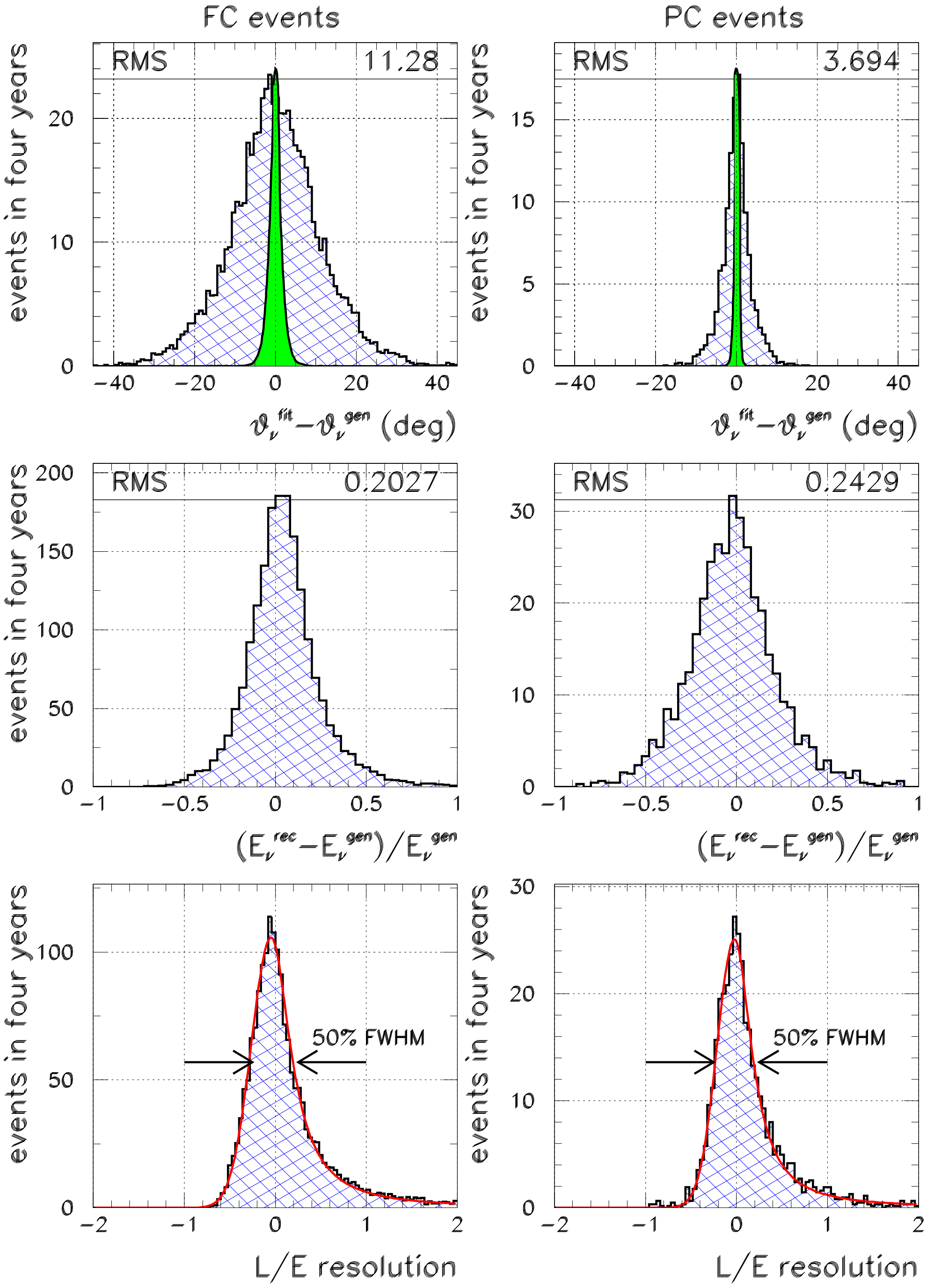

Figure 5.4: *Top:* Resolution on the neutrino zenith angle for contained (left) and partially contained (right) events after the selections discussed in the text. The dark histogram superimposed shows the contribution to the resolution on the neutrino zenith angle due to the precision of the muon track fit: the precision on the neutrino angle is dominated by kinematic effects. *Middle:* Neutrino energy resolution on contained (left) and partially contained (right) events selected. *Bottom:* L/E resolution for contained (left) and partially contained (right) events.

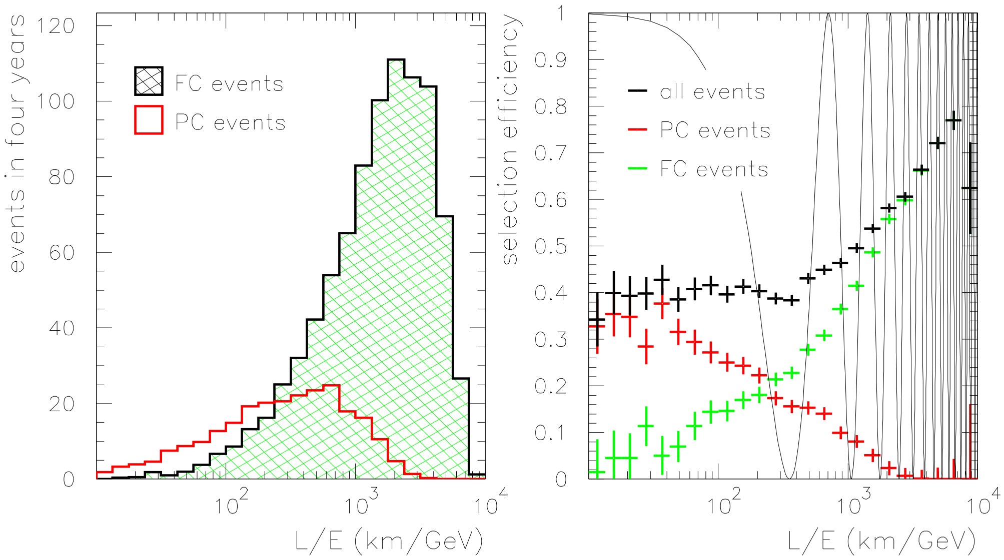

Figure 5.5: *Left:* L/E spectra of fully contained (FC) and partially contained (PC) events surviving the selection discussed in the text. *Right:* Overall selection efficiency and selection efficiency to fully contained and partially contained events as a function of L/E. The ν_μ survival probability for $\Delta m^2 = 3.5 \times 10^{-3}$ eV^2, is superimposed.

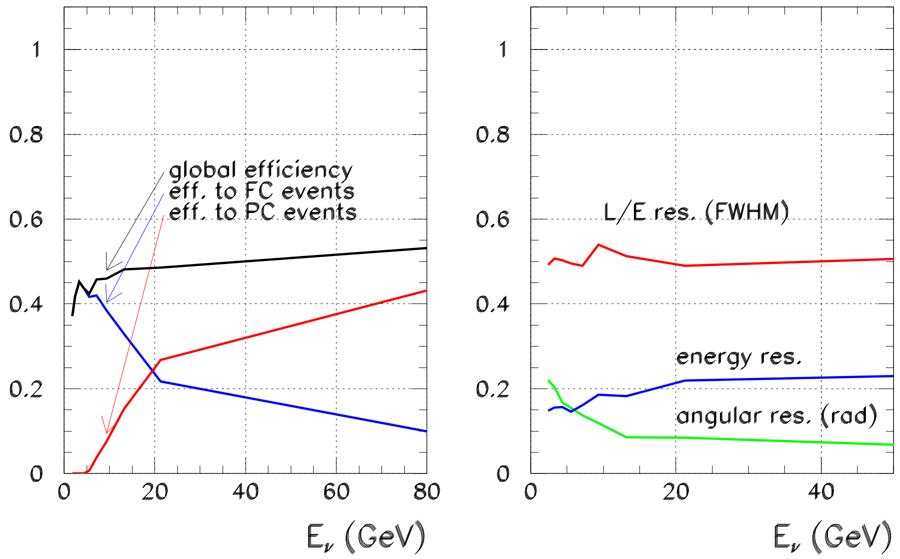

Figure 5.6: *Left:* Overall selection efficiency (black) and selection efficiency to fully contained (green) and partially contained (red) events as a function of E_ν. The up/down discrimination and charge identification in neutrino events are also shown. *Right:* Neutrino zenith angle, energy and L/E resolution as a function of the energy.

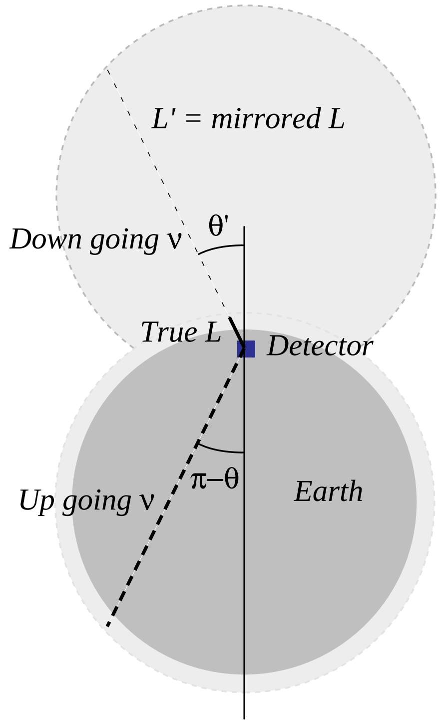

Figure 5.7: Artist's view of the mirror neutrino path length: downward going neutrinos (zenith angle $\theta < \pi/2$) are assigned the distance they would have travelled if $\theta = \pi - \theta$.

5.5 Disappearance of muon neutrinos

5.5.1 Far/Near sources comparison

Atmospheric neutrino fluxes are not in general up/down symmetric. However, the up/down asymmetry, which is mainly due to geomagnetic effects, is reduced to the percent level for neutrino energies above 1.5 GeV [85, 86] [2]. At these energies, for $\Delta m^2 < 10^{-2}$ eV^2, as indicated by Super-Kamiokande results, downward muon neutrinos are almost unaffected by oscillations. Thus, they may constitute a *near* reference source. Upward neutrinos are instead affected by oscillations, since the L/E ratio of their path length over the energy ranges up to 10^4 km/GeV. Atmospheric neutrinos therefore represent an ideal case for a disappearance experiment, since one may study oscillations with a single detector and two sources: a *near* and a *far* one. The effects of oscillations are then searched comparing the L/E distribution for the upward neutrinos, which should be modulated by oscillations, with a reference distribution obtained from the downward neutrinos. For upward neutrinos the path length L is determined by their zenith angle as $L(\theta)$, while the reference distribution is obtained replacing the actual path length of downward neutrinos with the mirror-distance $L'(\theta) = L(\pi - \theta)$ (see Fig. 5.5.1).

According to the figure and given symmetry properties of the cosine, the neutrino path-length

[2] As discussed in section 5.4.2, MONOLITH has an effective threshold around 3 GeV on ν_μ-CC events.

can therefore be estimated as

$$L(\theta) = R_{Earth}(\sqrt{1-k^2\sin^2\theta} - k|\cos\theta|)$$

, where $k = R_{Earth}/(R_{Earth}+\Delta R) \simeq 0.995$ and ΔR represents an average neutrino production height in the atmosphere. The ratio $N_{up}(L/E)/N_{down}(L'/E)$ will then correspond to the survival probability given, in case of oscillations, by

$$P(L/E) \;=\; 1 \;-\; sin^2(2\Theta)\; sin^2(1.27\;\Delta m^2\; L/E)$$

A smearing of the modulation is introduced by the finite L/E resolution of the detection method as discussed in the following.

Some remarks are in order:

i) results obtained by this method (known as Picchi & Pietropaolo's [87]) are to a large extent insensitive to systematic effects arising from uncertainties in the knowledge of atmospheric fluxes, neutrino cross sections and detector inefficiencies.

ii) this method does not work with neutrinos at angles near to the horizontal ($|\cos\theta| < 0.07$), since the path lengths corresponding to a direction and its mirror-direction are of the same order.

We also notice that if Δm^2 were larger than 10^{-2} eV^2 (Kamiokande region), upward neutrinos would be in almost complete oscillation, while the oscillation pattern would become detectable in the downward sample. In this limit, a mirror-distance $L'(\theta) = L(\pi - \theta)$ can be assigned to upward neutrinos, which can be used as a reference L/E distribution for downward neutrinos. In this case, due to the uncertain estimate of the neutrino path-length for downgoing neutrinos related to our ignorance of their production height in the atmosphere, there would be some model dependence in the determination of the oscillation parameters. Nonetheless, the observation of an oscillation pattern would still firmly test the oscillation hypothesis.

Data have been generated for several different values of oscillation parameters and processed through the MONOLITH full simulation and reconstruction programme. A unique set of selection criteria, outlined in Section 5.4.2, has been applied to all the samples of simulated data, independently of the values of oscillation parameters. These criteria have been defined to enable the selection of a pure sample of ν_μ-CC events of high resolution. In total, about 10^3 downgoing (reference) ν_μ-CC events will be selected in four years (for a 34 kt detector), with an L/E resolution of 50% FWHM over the entire L/E range (see table 5.1).

The analysis of the resulting L/E spectra has been based on a binned maximum-likelihood procedure. Similarly to the definition of event selections, the bin boundaries of the L/E distributions have been fixed without prior knowledge of the oscillation parameters. An equal bin-size on a logarithmic scale, corresponding to a constant relative L/E sampling resolution, has been adopted. It can be shown that, in order to keep sensitivity to the oscillation pattern for every possible (yet unknown) value of Δm^2, the bin-size should satisfy $\Delta\log(L/E) \leq 0.5$ [89]. As for the requirement of an L/E resolution better than 50% FWHM, the upper limit at 0.5 on the bin-size is set by the requirement that the oscillation be sampled at twice its frequency at least over the first modulation period.

The likelihood function compares the observed rates of upgoing to downgoing events as a function of L/E and is defined as:

$$\mathcal{L} = \prod_{i=1}^{N_{bins}} \frac{\mu_i^{D_i} e^{-\mu_i}}{D_i!} \left[\mu_i P_i(\Theta, \Delta m^2)\right]^{U_i} \frac{\exp\left[-\mu_i P_i(\Theta, \Delta m^2)\right]}{U_i!} \tag{5.1}$$

where the first term accounts for the Poisson probability that an expectation value of μ_i events would have produced the D_i downgoing events actually observed, while the second term gives the Poisson probability to observe U_i upgoing events when $\mu_i P_i(\Theta, \Delta m^2)$ are expected. $P_i(\Theta, \Delta m^2)$ represent the ν_μ survival probability for the *i-th* bin for given values of oscillation parameters and is parametrised as:

$$P(L/E; \Theta, \Delta m^2) = 1 - \frac{\sin^2(2\Theta)}{2}\left[1 - R(\Delta m^2, L/E)\cos(2.54\Delta m^2 L/E)\right], \tag{5.2}$$

where $R(\Delta m^2, L/E)$ folds in the experimental resolution and is taken as the Fourier transform of the resolution function. This parametrisation of the survival probability is valid under the assumption that the L/E resolution function be symmetric and that the L/E spectra of upgoing and downgoing neutrinos be (practically) flat [90]. Both these assumptions are reasonably satisfied. In particular, in the region where the first oscillation would manifest itself for any value of Δm^2 allowed by the Super-Kamiokande results, the L/E spectrum of selected events exhibits a variation of order 10% over a range where the resolution function changes by a factor 2. According to the MONOLITH simulation, and neglecting the small asymmetry in the L/E resolution function (see figure 5.4), $R(\Delta m^2, L/E)$ is best parameterised by an exponential damping term $R(\Delta m^2, L/E) = \exp(-0.25\ \Delta m^2\ L/E)$, corresponding to a Cauchy resolution function of 50% FWHM. Studies of systematic effects related to the knowledge of the resolution function are in progress.

The evaluation of the MONOLITH sensitivity has been based on the following statistical analysis. High statistics data samples have been simulated (corresponding to 25 y of exposure) and normalised to four years. Then the likelihood function (5.1) has been maximised with respect to all the parameters: μ_i ($i = 1,\ldots\ N_{bins}$), Δm^2 and $\sin^2(2\Theta)$. This approach very conservatively assumes no prior knowledge of the atmospheric neutrino fluxes, described by the μ_i parameters. Only the up/down symmetry of fluxes in case of no-anomalies in neutrino physics is implicitly embodied in the likelihood function.

After maximisation, the allowed confidence regions in the ($\sin^2(2\Theta)$,Δm^2) space have been evaluated by exploiting the properties of the likelihood-ratio function, defined by the quotient:

$$\lambda(\Delta m^2, \sin^2(2\Theta)) = \frac{\mathcal{L}_{max}(\hat{\mu}_i, \ldots\ \hat{\mu}_{N_{bins}}, \Delta m^2, \sin^2(2\Theta))}{\mathcal{L}_{max}(\hat{\mu}_i, \ldots\ \hat{\mu}_{N_{bins}}, \widehat{\Delta m^2}, \widehat{\sin^2(2\Theta)})}, \tag{5.3}$$

which represents the ratio of the maximum of the likelihood function within the subspace specified by fixed values of the oscillation parameters ($\sin^2(2\Theta)$, Δm^2) to the maximum of the likelihood function over the entire parameter space. The statistics $-2\log(\lambda)$ behaves asymptotically like a $\chi^2(2)$ distribution, whence the confidence regions have been determined. This procedure gives results identical to the ones obtained by means of the MINOS processor of the

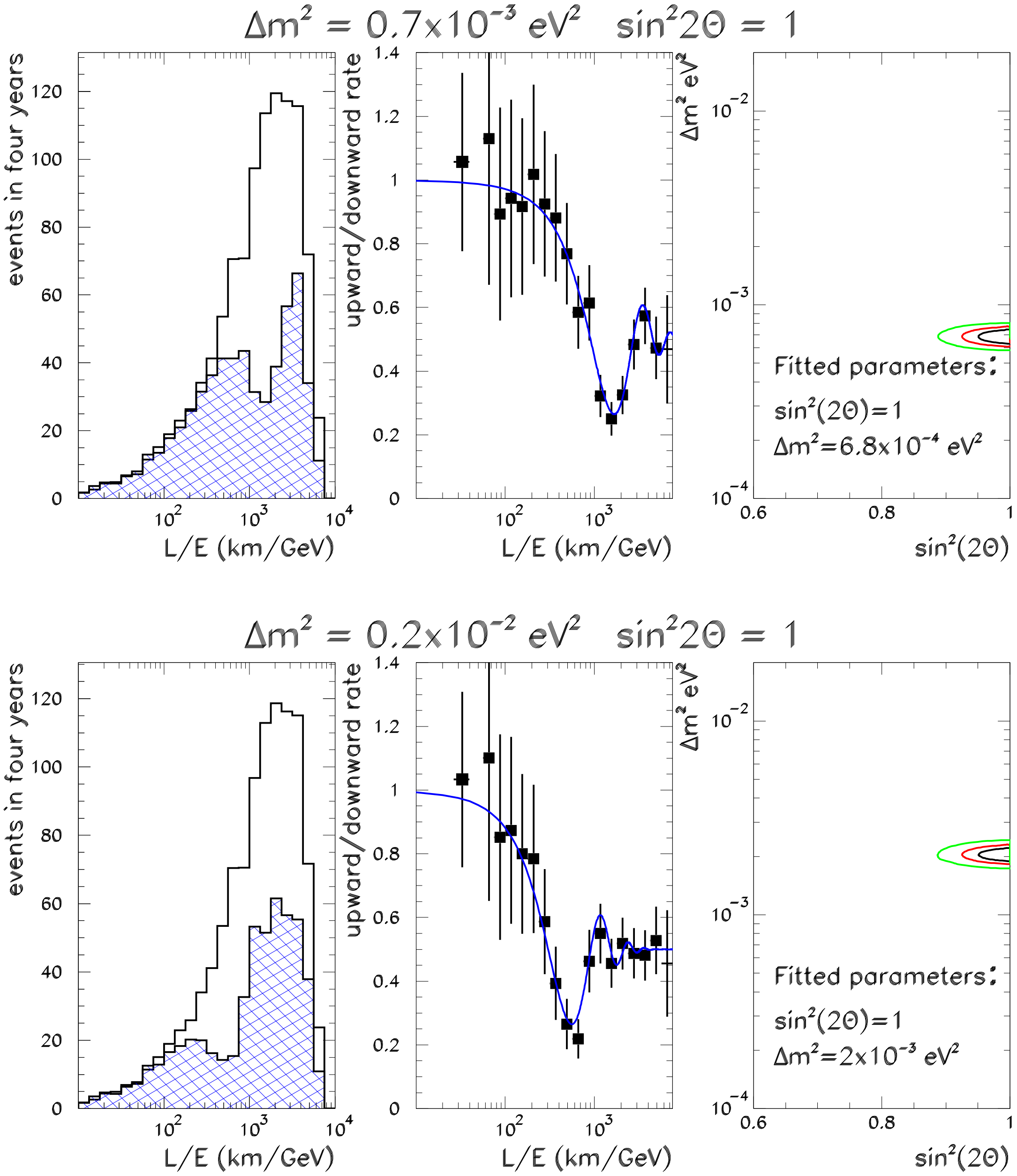

Figure 5.8: Results of the L/E analysis on a simulated sample in the presence of $\nu_\mu \to \nu_x$ oscillations, with parameters $\Delta m^2 = 7\times10^{-4}$ eV^2 and $\sin^2(2\Theta) = 1.0$ (top) and $\Delta m^2 = 2\times10^{-3}$ eV^2 and $\sin^2(2\Theta) = 1.0$. The figures show from left to right: the L/E spectrum of upward muon neutrino events (hatched area) and the L/E "mirrored" spectrum of downward muon neutrino events (open area); their ratio with the best-fit superimposed (the first point is integrated over the first six bins) and the result of the fit with the corresponding allowed regions for oscillation parameters at 68%, 90% and 99% C.L.. Simulated statistics correspond to 25 years of data taking, errors and rate normalisation entering in the best-fit procedure correspond to four years.

MINUIT library [91], which performs the computation of contours of equal likelihood with respect to two (oscillation) parameters, taking into account of all the correlations with the other (N_{bins}) parameters.

It has been checked that the procedure adopted yields a good approximation of the exact sensitivity contours. For each value of Δm^2, 10^4 experiments of four years each have been simulated, by sampling high-statistics L/E distributions shown in the figures, and the likelihood function (5.1) has been maximised with respect to all the parameters: in 93% of the cases, the maximum-likelihood estimates of the oscillation parameters are found to fall inside the 90% C.L. contours displayed.

If some prior knowledge of the atmospheric neutrino fluxes is assumed, e.g. by letting the overall normalisation of the flux vary, while fixing the shape of the neutrino spectrum (this is equivalent to the approach adopted by Super-Kamiokande), the coverage of our estimated 90% C.L. regions increases to 97% of the simulated experiments.

The L/E distributions for upward- and downward-going neutrinos obtained with the outlined procedure are shown in Figs. 5.8 to 5.10 for Δm^2 ranging from 7×10^{-4} to 8×10^{-3} eV^2 and maximal mixing. The figures also show the discovery potential (allowed regions of the oscillation parameter space) of the experiment after four years of exposure as determined from the maximisation of the likelihood function.

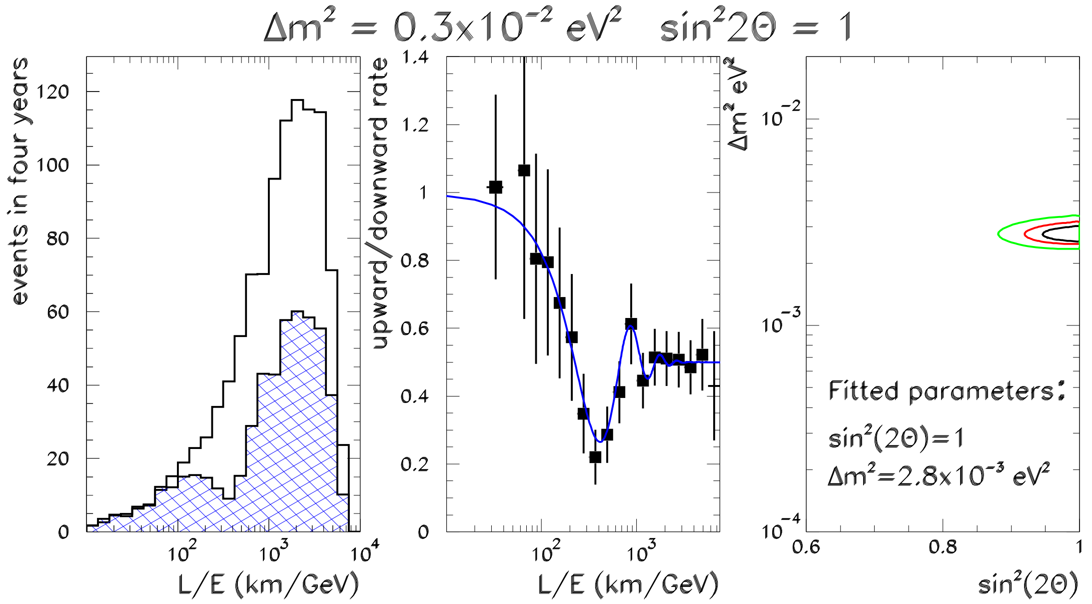

Figure 5.9: As Fig. 5.8, for $\Delta m^2 = 3 \times 10^{-3}$ eV^2 and $\sin^2(2\Theta) = 1$.

For large values of Δm^2 this approach loses sensitivity to the determination of the oscillation frequency, because of the limited statistics at small L/E. At Δm^2 around 10^{-2} eV^2 oscillation starts to manifest in the downgoing sample and the Picchi & Pietropaolo's method adopted here is not optimal. Still an up/down asymmetry will be clearly visible. Moreover, for Δm^2 larger

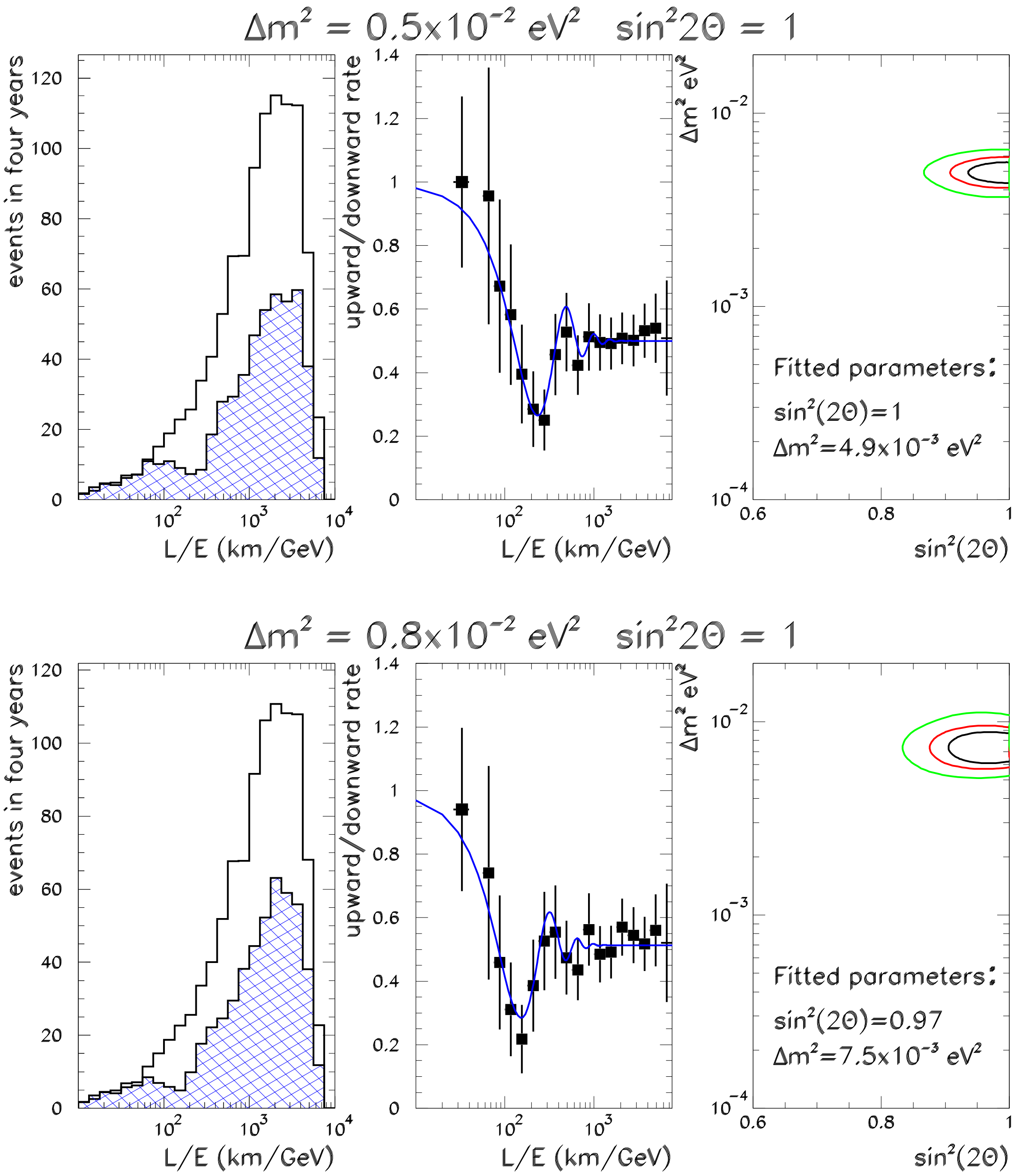

Figure 5.10: As Fig. 5.8, for $\Delta m^2 = 5 \times 10^{-3}$ eV^2 and $\sin^2(2\Theta) = 1$ (top) and $\Delta m^2 = 8 \times 10^{-3}$ eV^2 and $\sin^2(2\Theta) = 1$ (bottom).

than a few 10^{-2} eV^2, upward neutrinos – at large L/E – will be in complete oscillation, while the oscillation pattern would become detectable in the downward sample. In this limit, a mirror distance $L'(\theta) = L(\pi - \theta)$ can be assigned to upward neutrinos, which can be used as a reference L/E distribution for downward neutrinos. In this case, due to the uncertain estimate of the neutrino path-length for downgoing neutrinos related to our ignorance of their production height in the atmosphere, there would be some model dependence in the determination of oscillation parameters. Nonetheless, the observation of an oscillation pattern would still firmly test the oscillation hypothesis. An example of the L/E distribution and results obtained with this analysis was given in the MONOLITH Progress Report [63].

The results of the outlined analysis are summarised in figure 5.11. The precision on oscillation parameters (allowed regions at 90% C.L.) that can be achieved in four years of exposure is compared to the regions at 90% C.L. allowed by the Kamiokande and Super-Kamiokande results. In the absence of oscillations, the arguments presented can be used to exclude a region of oscillation parameters. The exclusion limits that this experiment will be able to set after an exposure of one year at 99% C.L. or four years at 90% and 99% C.L. are also shown in the figure.

Assuming that the oscillation hypothesis is true and for maximum mixing, MONOLITH can improve by one order of magnitude the relative accuracy in the measurement of Δm^2 over the entire range of oscillation parameters indicated by the most recent Super-Kamiokande reports. From the measurement of the oscillation pattern alone, we estimate a one standard deviation accuracy at the 5-10% level with a weak dependence on Δm^2 (see also figure 5.13 and the corresponding discussion below).

5.5.2 Clearness of the oscillation pattern

The atmospheric neutrino anomaly reported by Super-Kamiokande is believed to demonstrate the existence of neutrino oscillations. Alternative explanations, in which ν_μ neutrinos disappear without giving raise to an oscillatory pattern, are still viable and consistent with Super-Kamiokande results [10, 11, 12], though.

These unconventional interpretations of Super-Kamiokande data share the feature of the absence of a first clear dip in the L/E distribution, at clear variance with the oscillation scenario. The MONOLITH experiment is designed to have sufficient resolution to detect an oscillation pattern and discriminate between these different models.

In order to make a quantitative statement, a test statistics needs to be defined. Neither the neutrino oscillation (null hypothesis) nor the unconventional models (alternative hypothesis) are simple hypotheses, since the model parameters are not (completely) fixed a priory and must be determined from the experimental observations. Therefore a Neyman-Pearson test is not applicable.

On the other hand, a likelihood-ratio test can be designed, by describing the spectral distortion to the L/E spectrum of muon neutrinos by means of a general parametric form (*comprehensive* parametric hypotheses [92]):

$$p(x;\underline{\alpha},\underline{\beta},\theta) = \Big[(1-\theta)\; p_{H0}(x;\underline{\beta}) + \theta\; p_{H1}(x;\underline{\alpha})\Big]\,, \tag{5.4}$$

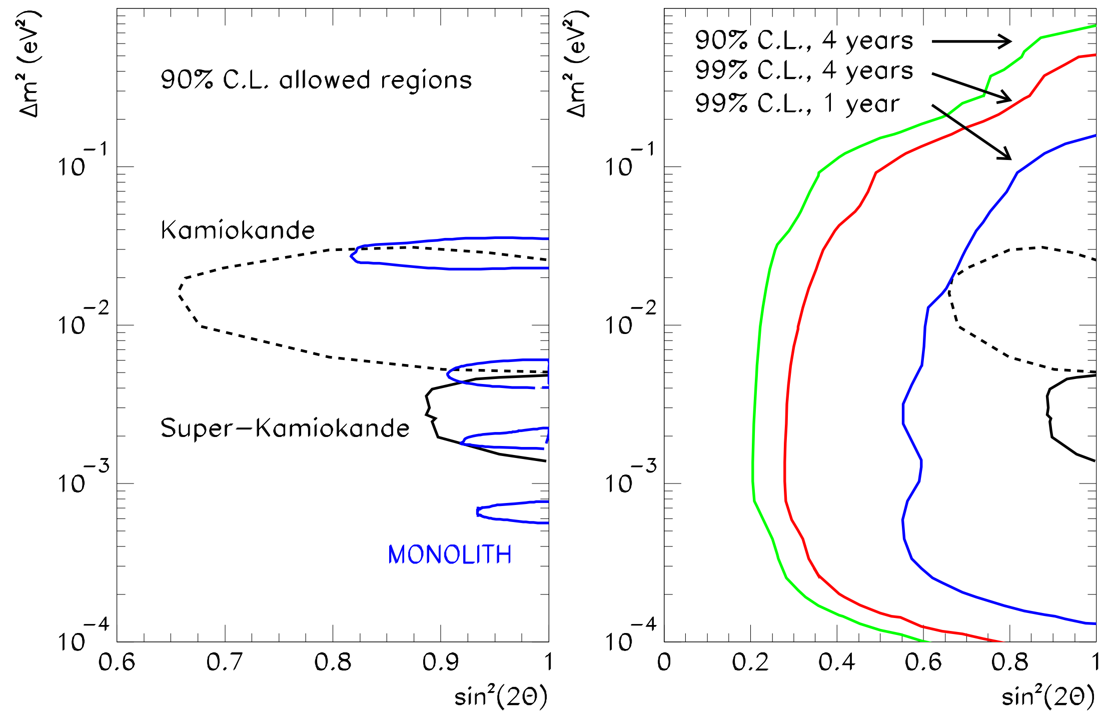

Figure 5.11: *Left*: Expected allowed regions of $\nu_\mu - \nu_\tau$ oscillation parameters for MONOLITH after four years of exposure, as obtained by the analysis described in the text: the results of the simulation for $\Delta m^2 = 0.7, 2, 5, 30 \times 10^{-3}$ eV^2 and maximal mixing are shown. *Right*: MONOLITH exclusion curves at 90% and 99% C.L. after one or 4 years of data taking assuming no oscillations. The full (dashed) black line shows the most recent results of the Super-Kamiokande [46] (Kamiokande [47]) experiment.

where $x = L/E$, the parameter θ is bound between 0 and 1, $p_{H0}(x;\underline{\beta})$ and $p_{H1}(x;\underline{\alpha})$ are the probability density functions for the null hypothesis (H0) and the alternative hypothesis (H1).

If either of the hypotheses is true, the parameters of equation (5.4) are restricted to lie in a subspace, defined by the constraints $\theta = 0$ (H0) or $\theta = 1$ (H1), of the total parameter space.

Given the observations x_1, $x_2 \ldots x_n$, a test statistics for either hypothesis can be defined by the quotient:

$$\lambda = \frac{\mathcal{L}_{max}(x_1, \ldots\ x_n; \underline{\alpha}, \underline{\beta}, \theta = 0, 1)}{\mathcal{L}_{max}(x_1, \ldots\ x_n; \underline{\alpha}, \underline{\beta}, \theta)}; \tag{5.5}$$

representing the ratio of the maximum of the likelihood function within the subspace specified by the restriction from either hypothesis to the maximum of the likelihood function over the entire parameter space. By construction, this ratio must be between 0 and 1, since the maximum of $\mathcal{L}$ over the subspace of either hypotheses cannot exceed the maximum over the entire space.

The ratio λ is a function of the observables and is intuitively a reasonable test statistics. If the maximum likelihood over the subspace of either hypothesis is close to the maximum likelihood over the full space ($\lambda \sim 1$), the hypothesis will have a large probability of being true. A small value of λ will indicate that the hypothesis is unlikely. The power of the test can be evaluated from the fact that in the asymptotic limit the statistics $-2\log(\lambda)$ approaches a $\chi^2(1)$ distribution.

The rejection power of the MONOLITH experiment against the alternative explanations to neutrino oscillations has been estimated by Monte Carlo techniques. In this study, the decay model of ref. [10] has been considered as alternative hypothesis to oscillation, since it allows for an easy parameterisation of the disappearance probability.

The best-fit of the decoherence model to Super-Kamiokande data [12] gives a parametric curve indistinguishable, for all practical purposes, from the one of the decay model, though analytically different. On the other hand, in the model proposed in [11], neutrinos transmogrify in a way which is not easy to parameterise analytically. The best-fits of this model to Super-Kamiokande data, however, again predict a disappearance probability rather similar in shape to the decay model and the results discussed hereafter should be still valid, to first approximation, also in that scenario. A detailed study is in progress.

In the decay model compatible with Super-Kamiokande data the survival probability is described by the parametric form:

$$p_{dec}(x, \underline{\alpha}) = \left(1 - \alpha_0 + \alpha_0 e^{-x/2\alpha_1}\right)^2 \tag{5.6}$$

where $x = L/E$ is the neutrino reduced path-length, α_0 is a mixing parameter and α_1 is the reduced decay length of the neutrino. This parametric form is only slightly affected by the experimental resolution, as the decay model does not have sharp structures.

On the contrary, the experimental resolution needs to be accounted for in case of neutrino oscillations. Following the discussion given in the previous section, equation (5.2) has been used to parameterise the survival probability for ν_μ–ν_τ oscillations (p_{osc}).

According to this discussion, a general parametric form for the survival probability of muon neutrinos is therefore given by equation (5.4), taking $p_{H0} = p_{osc}$ and $p_{H1} = p_{dec}$.

In the simulation of the experiments, the oscillation scenario with maximum ν_μ–ν_τ mixing has been assumed (null hypothesis). To test the rejection power against the alternative hypothesis at the 1% level, we have generated and analysed a large sample of experiments (10^4 for each value of Δm^2). To accomplish this, a simplified Monte Carlo simulation has been adopted: *i)* for each value of Δm^2 a high statistics (about 30 y of exposure) binned L/E spectrum has been obtained from the full simulation of the MONOLITH experiment after applying the selection criteria discussed in section 5.4.2; *ii)* from this set of reference L/E distributions, individual experiments of up to six years have been sampled according to Poisson statistics.

Simulated data have been compared to the L/E distribution predicted for no-oscillation and tested using the log-likelihood function defined by:

$$\log \mathcal{L} = \sum_{i=1}^{N_{bins}} (n_i \log(A\mu_i) - A\mu_i - \log n_i!) - \frac{1}{2}\left(\frac{A-1}{\sigma_A}\right)^2 . \tag{5.7}$$

The first term is the Poisson probability to observe n_i events when $A\mu_i$ are expected, where μ_i is given by the expected rate in the i-th bin in case of no oscillations times the survival probability over that bin, derived from eq. (5.4) and A is an overall normalisation factor. Similarly to the method adopted by the Super-Kamiokande collaboration, the second term in the likelihood is included to account for the prior knowledge on the atmospheric neutrino flux normalisation, which has been assumed to be known to 15%. No prior knowledge on model parameters has been assumed, instead.

For each simulated experiment, the likelihood function has been maximized over the entire space of parameters and over the subspaces defined by $\theta = 0$ (pure oscillation) and $\theta = 1$ (pure decay). As an example, four simulated MONOLITH experiments of 34×4 kt·y each, for $\Delta m^2 = 0.003$ eV^2 and maximum mixing, are shown in figure 5.12: the blue line is the best fit to data over the full parameter space, while the green (red) line is the best fit constrained to the subspace for H0 (H1).

The distribution of the test-statistics $-2\log(\lambda_{H0})$ obtained from the sample of simulated experiments has been used to define the critical regions at 95% C.L. and 99% C.L. of the null hypothesis. The distribution of $-2\log(\lambda_{H1})$ has been used to evaluate the probability that MONOLITH will reject the false hypothesis (decay) for a significance level on the true hypothesis of 95% and 99%. The test-statistics for the null hypothesis has been found to be consistent with the asymptotic $\chi^2(1)$ behaviour, hence the fraction of oscillation experiments giving $P(\chi^2 < -2\log(\lambda_{H1}), 1) \leq 0.05$ and $P(\chi^2 < -2\log(\lambda_{H1}), 1) \leq 0.01$ has been counted.

The results of the Monte Carlo calculation are shown in figure 5.13. MONOLITH has at least a 95% probability of rejection at 99% (95%) C.L. of the decay(-like) model up to $\Delta m^2 = 0.005(0.008)$ eV^2. The figure also show the precision on the determination of Δm^2 as obtained from the RMS dispersion of the likelihood fit on the simulated experiments assuming that the null hypothesis be true.

The "clearness of the oscillation pattern" can be (somewhat arbitrarily) defined as a 95% probability of rejection at 95% C.L. (or 99% C.L.) of the false (non-oscillation) hypothesis. The second and third columns of Table 5.2 summarise the statistics that MONOLITH needs to collect to demonstrate a "clear oscillation pattern" for the two definitions.

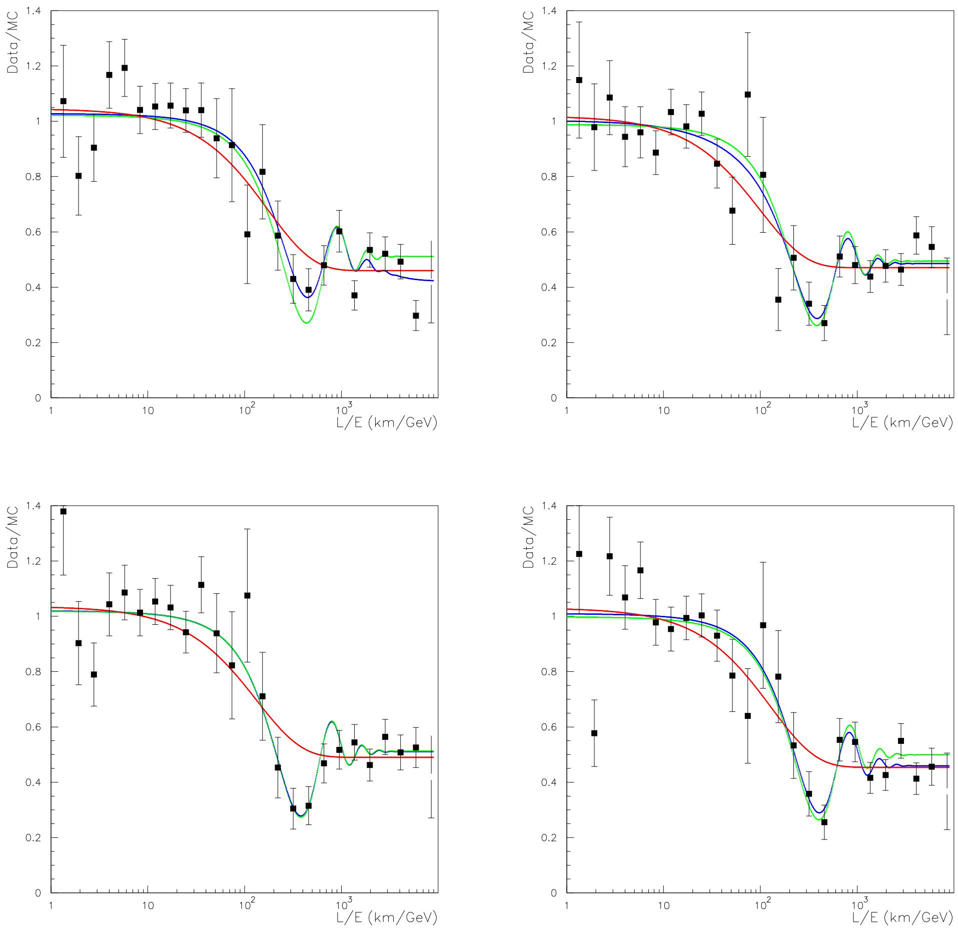

Figure 5.12: Four simulated MONOLITH experiments of 34×4 kt·y for $\Delta m^2 = 0.003$ eV^2. Experimental results are normalised to the neutrino spectrum for no oscillations. The survival probability of muon neutrinos derived from the best fit to data of the likelihood function over the full parameter space (blue), and over the subspaces for H0 (green) and H1 (red) are superimposed.

Δm^2 (10^{-3} eV^2)	statistics (kt·y) 95% prob. of rejection at 95% CL	statistics (kt·y) 95% prob. of rejection at 99% CL
1	34 x 1.6	34 x 2.7
3	34 x 2.4	34 x 3.3
5	34 x 3.0	34 x 4.1
8	34 x 4.1	34 x 5.6

Table 5.2: MONOLITH exposure needed to detect a "clear oscillation pattern" (see text).

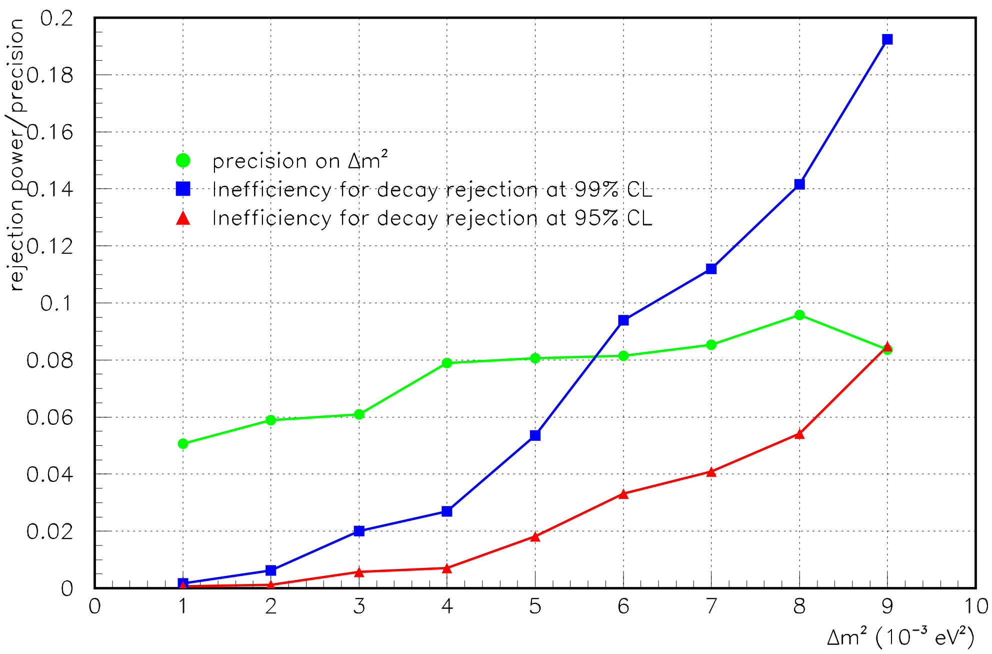

Figure 5.13: Inefficiency to decay model rejection as a function of Δm^2 for a significance level of 95% (red triangles) and 99% (blue squares) on the oscillation hypothesis. The precision on Δm^2 is also shown (see text).

5.6 Vertical planes configuration

Alternative geometries, with vertical iron planes, have also been simulated, since they offer a better acceptance to neutrino interaction induced by the CNGS beam and a better background discrimination for possible future neutrino-factory events from CERN.

As far as atmospheric neutrinos are concerned, a structure with vertical planes presents acceptance limitations along the vertical, while it offers improved reconstruction capabilities for events near the horizontal. These latter events, however, have a limited L/E resolution as discussed in section 4.1 and most of them are eliminated by the selection criteria.

The vertical layout is made of 300 vertical 8 cm iron planes 15×12 m^2 providing the same detector mass; the structure of the magnetic field is also similar to the one considered for one single module in MONOLITH, with an average magnetic induction of about 1.3 T.

Fig. 5.14 compares the samples of selected events (fully and partially contained) as a function of L/E for a structure with 8 cm iron planes oriented vertically or horizontally. The same reconstruction technique and the same set of selection criteria, along the lines discussed in section 5.4.2, has been applied in both cases. No specific selection against the cosmic muon background, which is more severe for the vertical layout, has been introduced.

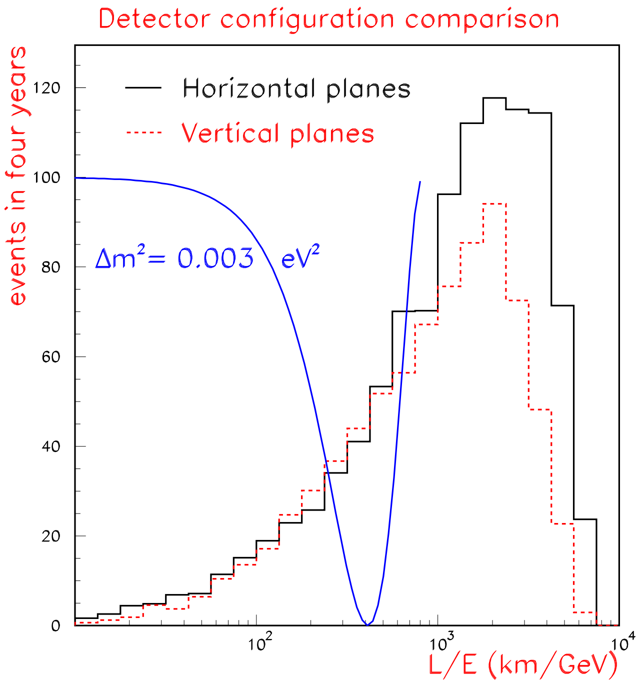

Figure 5.14: Comparison of the statistic of fully and partially contained events selected with the vertical (dotted line) and horizontal (full line) layout. The loss in efficiency at large L/E is due to lower event reconstruction capabilities along the vertical direction.

The figure shows that, in the region where the first oscillation minimum would manifest itself, for all the values of Δm^2 allowed by Super-Kamiokande results, the statistic of selected events is similar in the two geometries, while at large L/E the effect of the limited acceptance along the vertical of the vertical structure is visible. This results in a reduced sensitivity to the mixing angle, but not for the Δm^2.

We present the results of an analysis along the lines described in section 5.4, without any specific selection against the cosmic muon background, which is of particular importance when, as in this case, events with outgoing (not contained) muons are included in the selected sample. An external veto is therefore assumed. Figure 5.15 shows for the values $\Delta m^2 = 2,5\ eV^2$ the L/E distributions for up-going and down-going muons together with their ratio, the fitted parameters and the 68%, 90%, 99% C.L. contours.

The above results show that, concerning the observation of the L/E pattern, the performances obtained with the vertical layout are similar to those obtained with the baseline solution.

5.7 Staged approach: 12 kt module

In this section a study of the performance of a MONOLITH module of 13.5 m $\times$ 16 m surface and 8.5 m height, that could be possibly housed in the Hall A of the Gran Sasso Laboratory in the available space between LVD and GNO apparati, is reported.

In a running period of 4 y, this detector will collect somewhat less than 1/3 of the statistics expected for MONOLITH and its sensitivity will be correspondingly reduced. This results in a marginal improvement of the Super-Kamiokande determination of the oscillation parameters. Nonetheless this first module can provide an independent and complementary test of oscillation in atmospheric neutrinos, while the preparation of the larger detector (additional modules) will proceed in parallel.

This module could also be ready before the advent of the CNGS beam, that can be exploited for disappearance and NC/CC measurements, which can give supplementary information to atmospheric neutrino data. It has to be clear that for this reduced mass, the relative importance of CNGS beam events is increased and a re-optimization of the detector in terms of layer orientation and granularity may be required.

As a baseline approach we have simulated a detector having the same structure as the one discussed in chapter 4. The transverse dimensions almost match the ones of one single module of MONOLITH, while the detector here considered is about 3.5 m less high and consists of 85 layers of 8 cm iron interleaved by 2 cm gaps for GSC detectors. The structure of the magnetic field is also similar to the one considered for one single module in MONOLITH, with an average magnetic induction of about 1.3 T. The total mass of this detector is about 12 kt.

5.7.1 Selections and performance

The simulation and reconstruction chain adopted is the same as discussed in previous sections. The best sensitivty is achieved for the same set of event selections discussed in section 5.4.2 and aimed at the observation of an oscillation pattern in ν_μ disappearace. Events are retained if

1) $E_{muon} > 1.5$ GeV;

2.a) they are fully contained (FC) in a fiducial volume, defined by requiring no hits in the first/last 4 layers and no hits in the first/last 10 strips in X and Y;

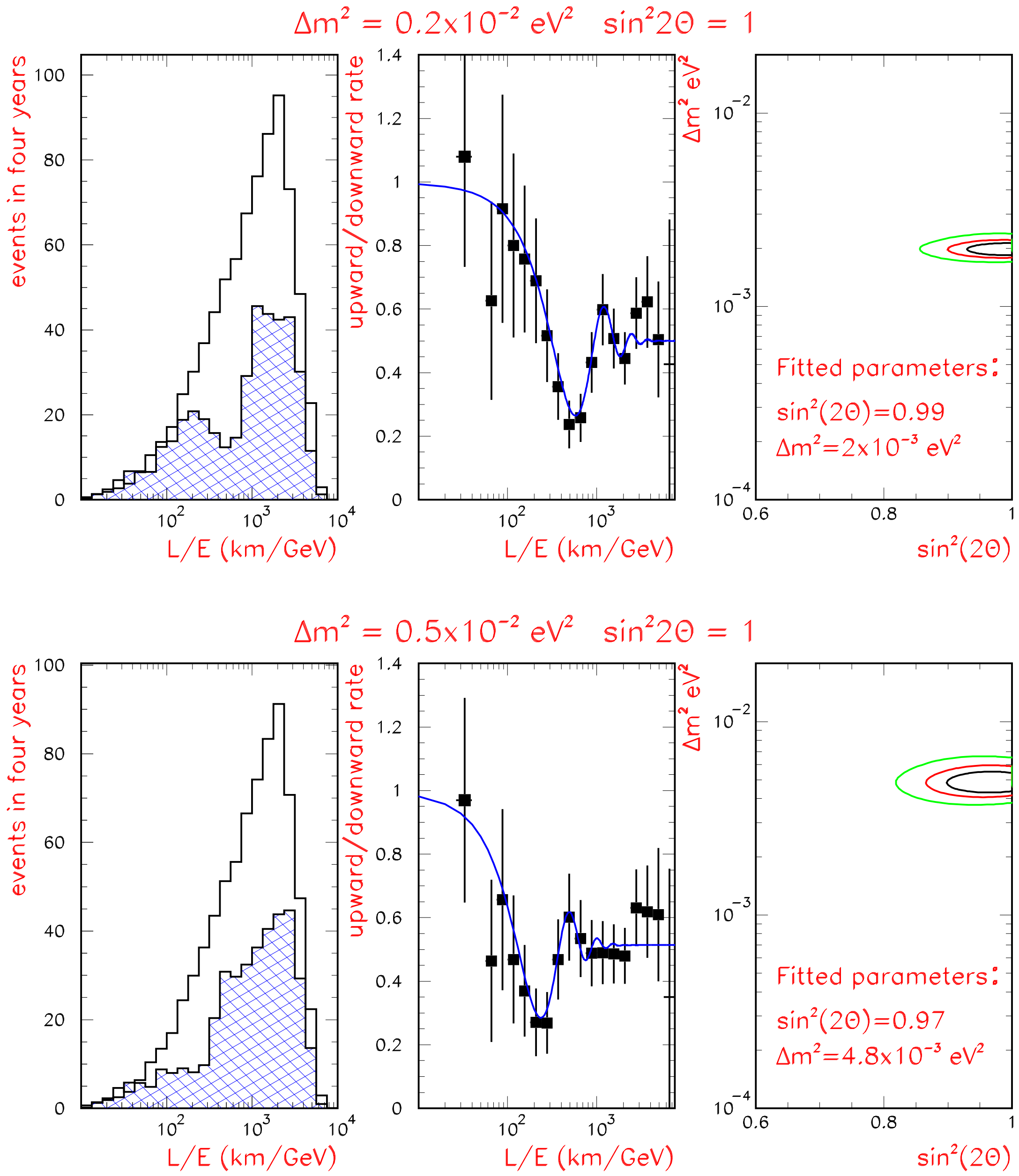

Figure 5.15: As Fig. 5.8, for $\Delta m^2 = 2 \times 10^{-3}$ eV^2 and $\sin^2(2\Theta) = 1$ (top) and $\Delta m^2 = 5 \times 10^{-3}$ eV^2 and $\sin^2(2\Theta) = 1$ (bottom) for the vertical detector layout.

2.b) they are partially contained (PC) in the same fiducial volume with a single outgoing track (muon) with a reconstructed range greater than 4 metres;

3) at least seven layers are fired by the muon candidate;

4) the expected relative L/E resolution of the event; estimated on the basis of the reconstructed muon energy, muon direction and hadron energy, is better that 50% FWHM.

These criteria select a "high resolution" and up/down symmetric sample of CC-atmospheric muon neutrino events with small contamination of internal (NC-events) and external (cosmic rays) backgrounds.

The performance of the 12 kt MONOLITH module on the events surviving these selections is shown in figure 5.16. The angular, energy and L/E resolutions are simular to the one obtained for the simulation of MONOLITH. The somewhat better energy resolution on PC events and angular resolutions on the muon direction have to be ascribed to the improved muon track fitting procedure. The resolution on the neutrino direction is about 11.5 (4.2) degrees for contained (semi-contained) events and is dominated by the μ–ν scattering angle.

A summary of the efficiencies and resolutions as a function of the neutrino energy is given in figure 5.17. Efficiency and resolutions and their dependence on the neutrino energy are similar to the one computed for the full MONOLITH detector. The effective threshold for atmospheric ν_μ-CC event reconstruction is around 3 GeV, above which value the efficiency is approximately constant around 40%. This figure is lower than the 50% plateau efficiency of the full detector, the loss being entirely due to the effect of the selections defining the fiducial volume. The effective fiducial mass of the 12 kt module is indeed about 7.3 kt.

With these selections about 6.6 "unoscillated" downgoing neutrino events/kty are expected corresponding to a sample of about 320 events in four years. This corresponds to a reduction of a factor about 3.5 in the available statistics for a reduction of 2.8 in the detector mass. Thus in the 12 kt module, each event will have an "extra-cost" of around 25%. The sensitivity to oscillations with this sample is discussed in the following.

5.7.2 Detection of an oscillation pattern

The discrimination of models implying a dynamics of ν_μ disappearance alternative to oscillations can be evaluated with the same test statistics discussed in Section 5.5.2.

Figure 5.18 compares the efficiency for decay rejection at 95% C.L. for the full detector and the 12 kt module. There is a fair chance that the statistical fluctuation of the experiment prevent the rejection of the decay model or other models with similar disappearance dynamics.

This test mostly relies on the available statistics around the minimum of the survival probability distribution and on the L/E resolution. The latter can be improved, without loss of efficiency if the hadron energy flow can be reconstructed. A gain of about 2. degrees in the neutrino angle resolution (from 11.5 to 9.5 decgrees), that seems achievable with this detector, would give a gain in rejection power equivalent to about a factor 1.5 increase in statistics. Two remarks are in order: i) the adoption of a detector of finer granularity could be advantageous; ii) the hadron energy flow reconstruction is certainly more uncertain than the measurement of the

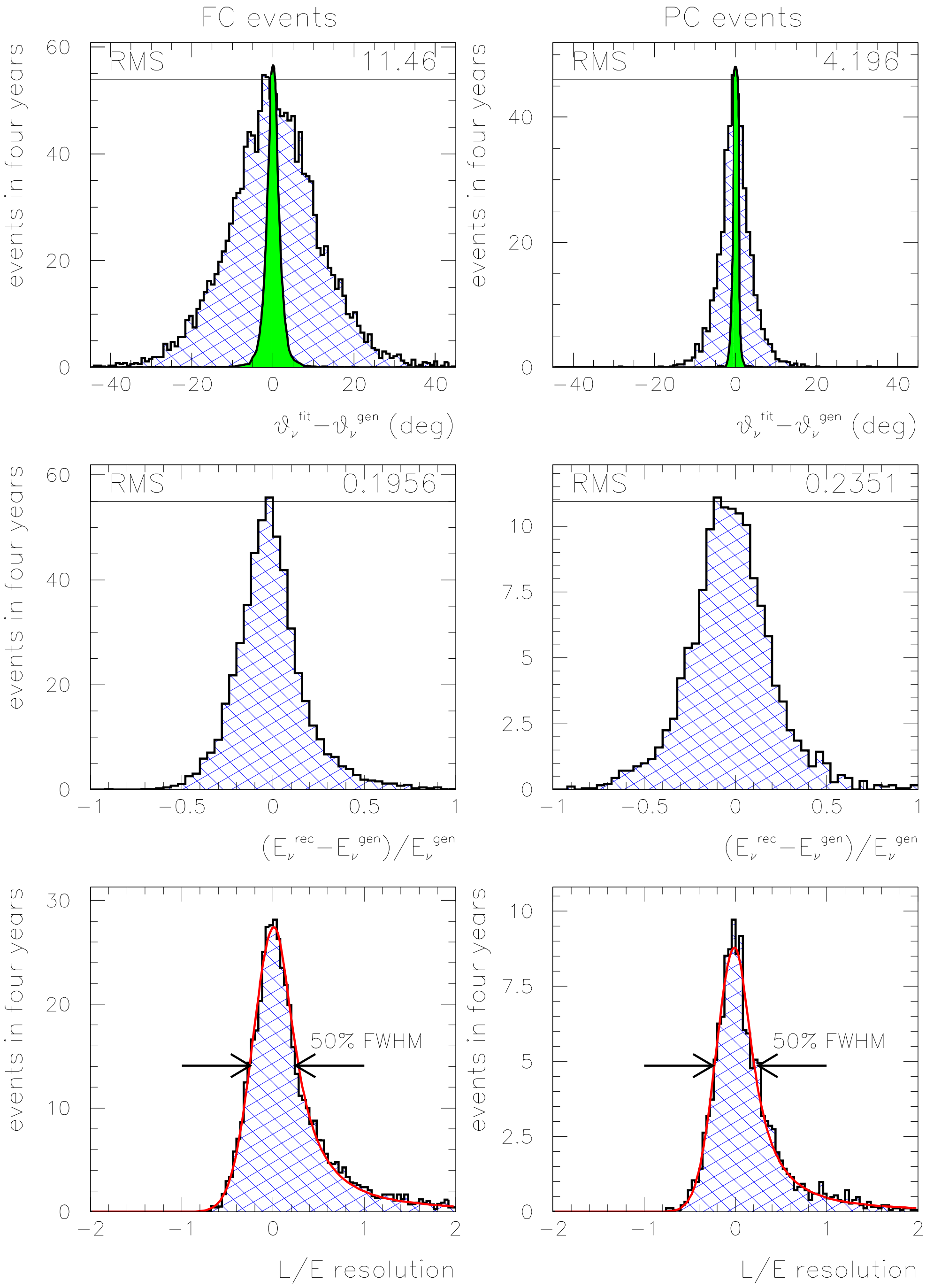

Figure 5.16: *Top:* Resolution on the neutrino zenith angle for contained (left) and partially contained (right) events after the selections discussed in the text. The dark histogram superimposed shows the contribution to the resolution on the neutrino zenith angle due to the precision of the muon track fit: the precision on the neutrino angle is dominated by kinematic effects. *Middle:* Neutrino energy resolution on contained (left) and partially contained (right) events selected. *Bottom:* L/E resolution for contained (left) and partially contained (right) events.

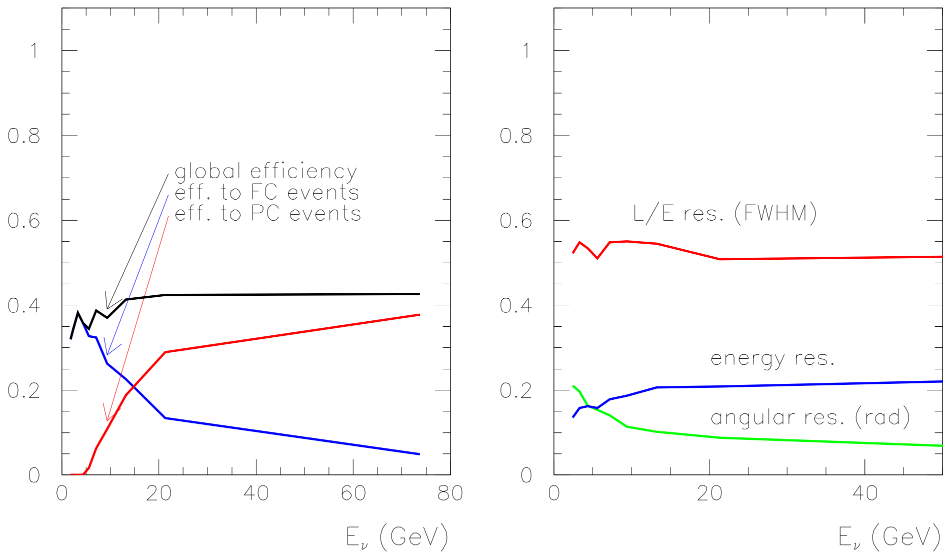

Figure 5.17: *Left:* Overall selection efficiency (black) and selection efficiency to fully contained (green) and partially contained (red) events as a function of E_ν. *Right:* Neutrino zenith angle, energy and L/E resolution as a function of the energy.

muon direction and the impact of systematic uncertainties could be non-negligible. A detailed study is necessary.

5.7.3 Measurement of oscillation parameters

The estimated precision on the measurement of oscillation parameters has been evaluated using the same procedure described in Section 5.5. The analysis of the resulting L/E spectra has been based on the binned maximum-likelihood of equation 5.1

The evaluation of the MONOLITH sensitivity has been based on the following statistical analysis. High statistics data samples have been simulated (corresponding to 70 y of exposure) and normalised to four years. Then the likelihood function of eq. (5.1) has been maximized with respect to all the parameters: μ_i ($i = 1,\dots\ N_{bins}$), Δm^2 and $\sin^2(2\Theta)$.

After maximization, the allowed confidence regions in the ($\sin^2(2\Theta)$,Δm^2) space have been evaluated by exploiting the properties of the likelihood-ratio function, defined by the quotient:

$$\lambda(\Delta m^2, \sin^2(2\Theta)) = \frac{\mathcal{L}_{max}(\hat{\mu}_i, \dots\ \hat{\mu}_{N_{bins}}, \Delta m^2, \sin^2(2\Theta))}{\mathcal{L}_{max}(\hat{\mu}_i, \dots\ \hat{\mu}_{N_{bins}}, \widehat{\Delta m^2}, \widehat{\sin^2(2\Theta)})}, \tag{5.8}$$

which represents the ratio of the maximum of the likelihood function within the subspace specified by fixed values of the oscillation parameters ($\sin^2(2\Theta)$, Δm^2) to the maximum of the likelihood function over the entire parameter space. The statistics $-2\log(\lambda)$ behaves asymptotically like a $\chi^2(2)$ distribution, whence the confidence regions have been determined.

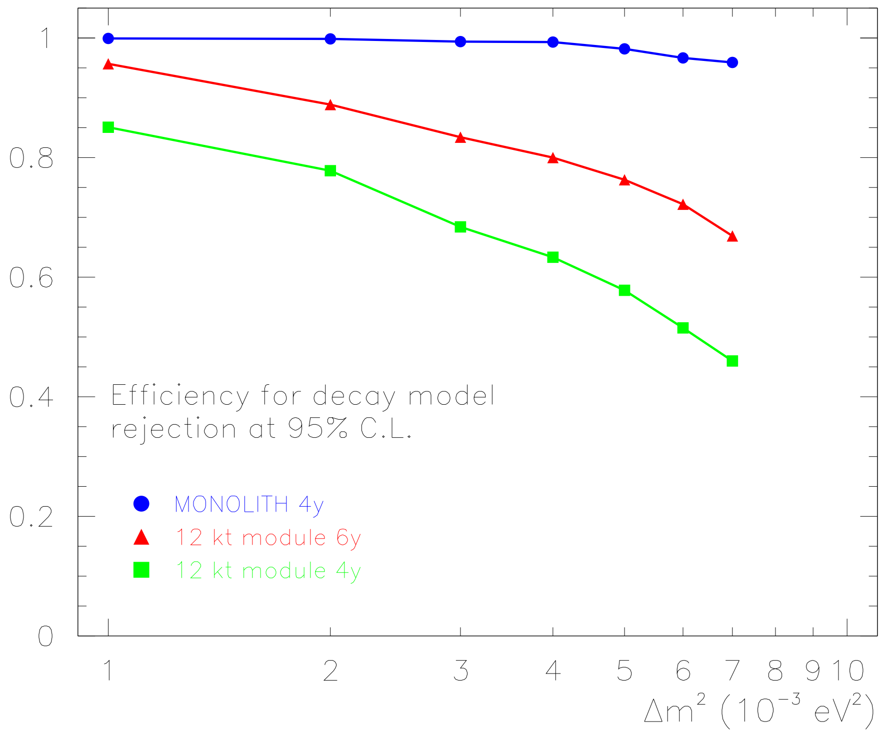

Figure 5.18: Efficiency for decay rejection at 95% C.L. assuming thet the null hypothesis be oscillation with Δm^2 as indicated in the figure and maximum mixing. The performance of a 12 kt detector are compared to the full MONOLITH performance.

This approach very conservatively assumes no prior knowledge of the atmospheric neutrino fluxes, described by the μ_i parameters. Only the up/down symmetry of fluxes in case of no-anomalies in neutrino physics is implicitly embodied in the likelihood function.

The L/E distributions for upward- and downward-going neutrinos obtained with the outlined procedure are shown in Fig. 5.19 for maximal mixing and two values of Δm^2 allowed by current Super-Kamiokande data. The figures also show the expected sensitivity on oscillation parameters (allowed regions of the oscillation parameter space) of the experiment after four years of exposure.

A 12 kt detector has the capability to improve the determination of the oscillation frequency, thanks to the improved L/E resolution. However, the precision on the mixing parameter will be limited by the available statistics.

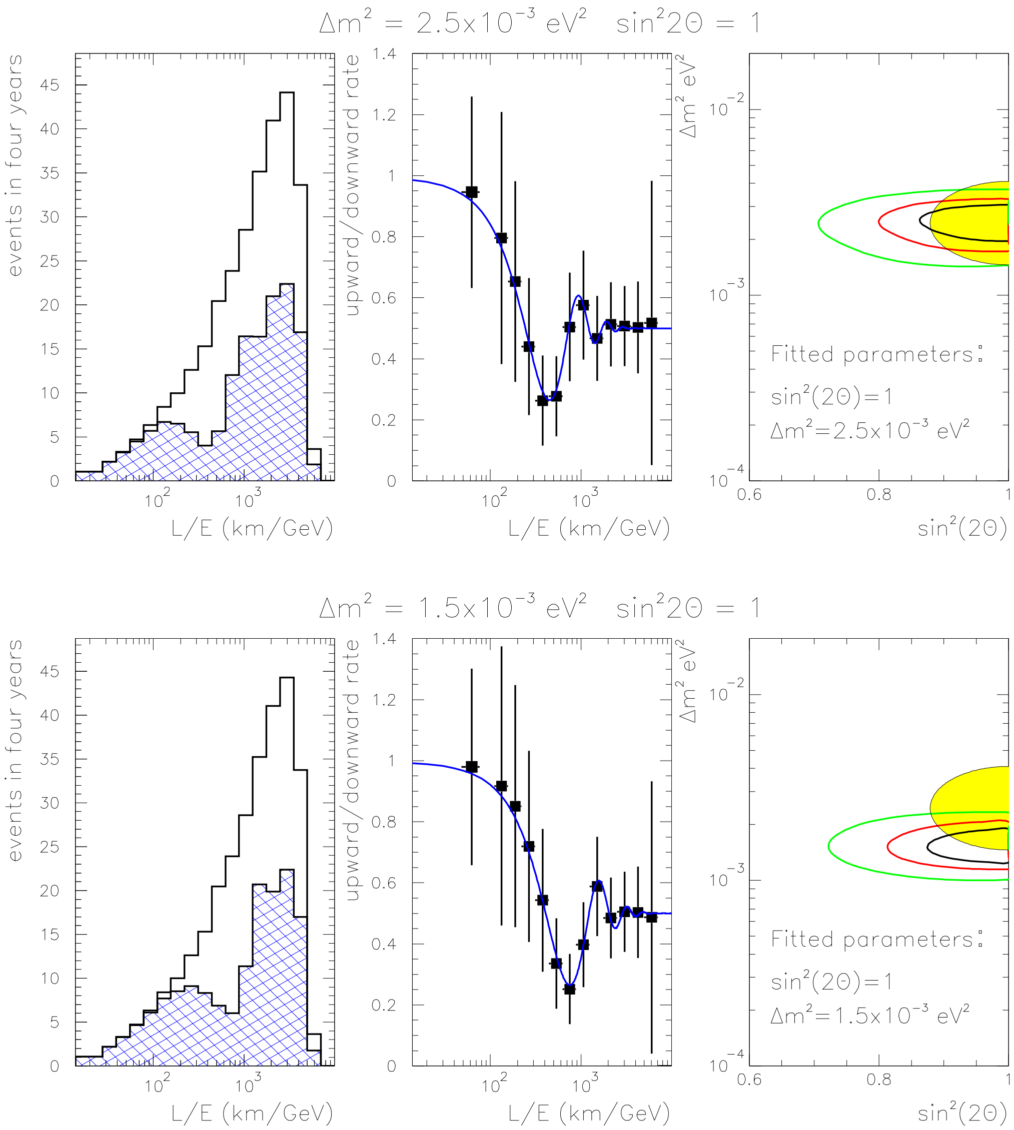

Figure 5.19: Results of the L/E analysis on a simulated sample in the presence of $\nu_\mu \rightarrow \nu_x$ oscillations, with parameters $\Delta m^2 = 1.5, 2.5 \times 10^{-3}$ eV^2 and $\sin^2(2\Theta) = 1.0$. The figures show from left to right: the L/E spectrum of upward muon neutrino events (hatched area) and the L/E reference spectrum of downward muon neutrino events (open area); their ratio with the best-fit superimposed (the first point is integrated over the first six bins) and the result of the fit with the corresponding allowed regions for oscillation parameters at 68%, 90% and 99% C.L.. Simulated statistics correspond to about 70 years of exposure, errors and rate normalisation entering in the best-fit procedure correspond to four years. Tha shaded area shows the 90% C.L. region allowed by current Super-Kamiokande results

5.8 Summary and conclusions

By exploiting the high energy component of the atmospheric muon neutrino fluxes, this experiment has the capability to detect the oscillation pattern from the comparison of L/E spectra of upgoing and downgoing neutrinos. The outlined analysis takes advantage of the up/down symmetry of the high energy atmospheric neutrino fluxes, which makes high energy atmospheric neutrinos an ideal source for disappearance experiments.

In the apparatus considered, the determination of the neutrino energy and direction relies mostly on the muon reconstruction. By means of the measurement of ν_μ disappearance, the existence of oscillations can be (dis)proved and the parameters measured over the entire range suggested by Super-Kamiokande and Kamiokande results (see fig. 5.11). Moreover, unconventional models still consistent with Super-Kamiokande data can be discriminated by the observation of the oscillation pattern.

A full simulation of a different detector geometry, based on vertical planes, has been developed and results are comparable with the horizontal option. The main difference is the lower efficiency for large L/E events (i. e. near to vertical). However, these events are in the region where the oscillation averages, out of the first oscillation dip. This results in a lower precision in the mixing angle, but does not affect the determination of the Δm^2 and the capability to see the full first oscillation swing.

A 12 kt module shows resolution similar to the full detector and efficiency lowered just by the minor fiducial volume. The collected statistics is therefore reduced by a factor 3.5. Taking data for four years allows to confirm the SK results with different systematics and to improve the precision of the Δm^2 parameter, but the discrimination between different physics mechanisms is not under reach.

Chapter 6

Physics with the CERN to Gran Sasso neutrino beam

In addition to atmospheric neutrinos, for which it has been optimized, MONOLITH will also detect more than 100000 events (CC+NC) per year from the CERN to Gran Sasso (CNGS) neutrino beam, which is scheduled to start operations in 2005. In this chapter, we present a qualitative study of the MONOLITH performance in this beam. A full quantitative study needs a detailed understanding of the beam systematics, which is not yet completed.

Beam neutrinos arrive at an angle of 4° (upward) from the horizontal direction, almost parallel to the "long" axis of the MONOLITH detector. Despite its optimized design for atmospheric neutrinos, the MONOLITH detector in its uniformly horizontal option can reconstruct $\sim 46\%$ of the CC events with optimal energy resolution. In terms of events, this result makes MONOLITH the detector which will monitor the CNGS beam with highest statistical precision and good energy resolution ($\sim$ 41000 events/year expected to be reconstructed with energy resolution $\leq 22\%$). This huge sample can complement the MONOLITH atmospheric neutrino analysis of the L/E distribution in the region (20-200) km/GeV. The remaining part of the data is reconstructed with less precision, but can still be used for flux monitoring purposes.

To further improve the beam performance, the detector can be equipped with vertical end caps. The performance of this end-cap option is also investigated and the gain in terms of efficiency with respect to the uniform detector option is discussed.

6.1 Detector and beam simulations

The reference detector layout considered in the simulation ("uniform detector option") has been already discussed in Chapter 4 and is shown in Fig. 5.1. At variance with the baseline option considered in the MONOLITH Progress Report [63], in this layout the field lines are perpendicular to the CNGS beam direction, bending tracks out of the iron planes. This feature is very helpful for the reconstruction of events from the CNGS beam.

Charged current interaction of neutrinos from the CNGS beam have been simulated using the same generator adopted to describe atmospheric neutrino interactions [78, 79] (see section 4.3.1). The neutrino energy has been sampled from the reference CNGS beam spectrum [48]. To estimate the number of events we assumed 5×10^{19} pot/year. The input cross-section weigthed spectrum is shown in Fig. 6.1. The events have then been processed by the GEANT3 simulation of the MONOLITH detector.

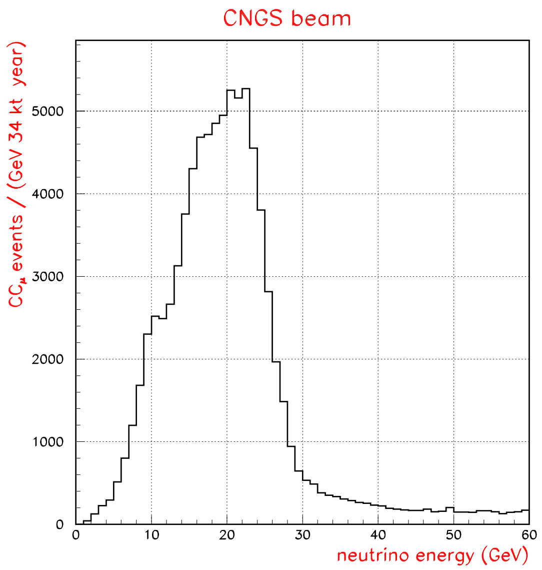

Figure 6.1: Number of charged current ν_μ interactions in MONOLITH from CNGS beam in 1 year

As an example we show in Fig. 6.2 a 39.6 GeV event interaction inside MONOLITH, where the reference system is also shown: the Y-axis is along the Hall axis and parallel to the beam.

6.2 Reconstruction and event selection

Muons produced by ν_μ-CC interactions of CNGS beam neutrinos develop along the iron layers and may travel a sizeable distance inside them before they are bent out by the magnetic field. A precise measurement of their momentum can be obtained either from range of from track curvature, provided a good estimate of the vertex position is available. Therefore, events have been required to have at least one hadronic hit (i.e. not belonging to the muon). Taking the first y-hit as the vertex position, we obtain the vertex resolution shown in Fig. 6.3. Despite the coarse granularity of the detector, resolutions of the order of 5 cm on the vertex position are achievable on each coordinate. Small systematic errors on Y and Z, due to the beam direction (neutrinos are emerging with an angle of 4^o from the horizon) have been *a posteriori* corrected for.

For the analysis, the ν_μ-CC events have been divided in partially contained (PC) or fully contained (FC) depending if the muon track is exiting the detector or not. In Fig. 6.4 the fraction of FC events as a function of neutrino energy is shown. For the full detector (Y-length 30 m) the fraction of FC events is larger than 50% till $E_\nu \sim 35$ GeV.

As for atmospheric CC ν_μ interaction, for FC events the muon energy reconstruction is based on the range technique. Requiring at least 7 hits to belong to the muon track, the

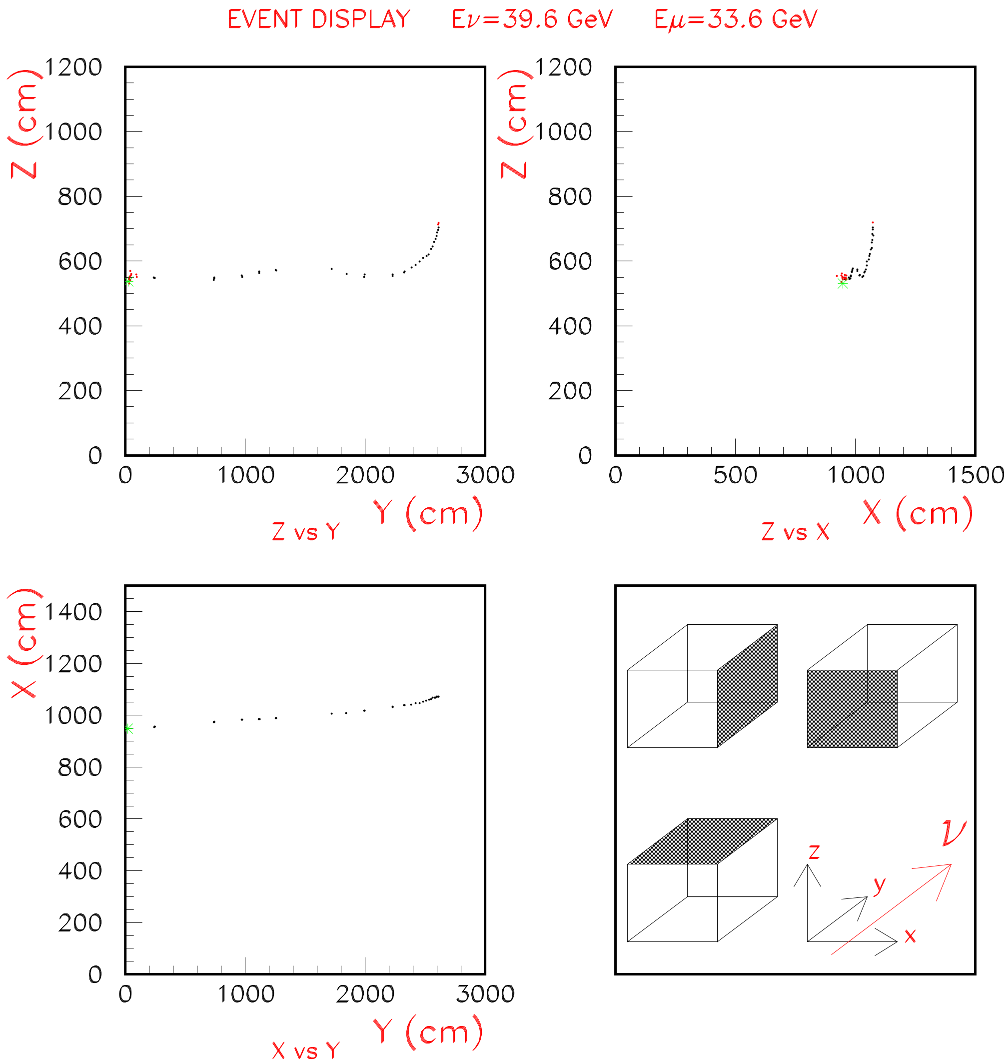

Figure 6.2: A 39.6 GeV charged current ν_μ interaction from CNGS beam inside MONOLITH.

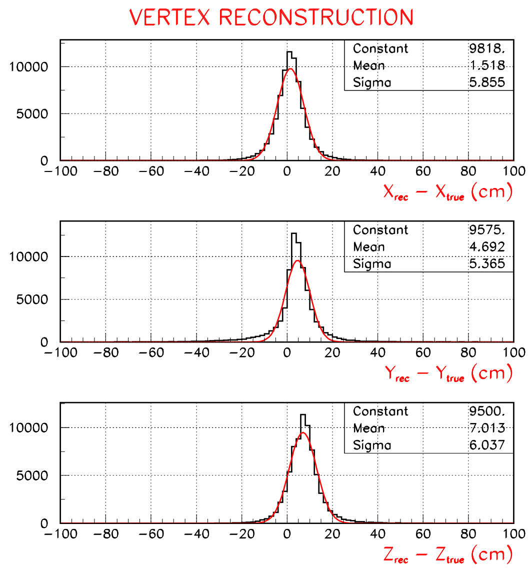

Figure 6.3: Errors on reconstructed vertex position.

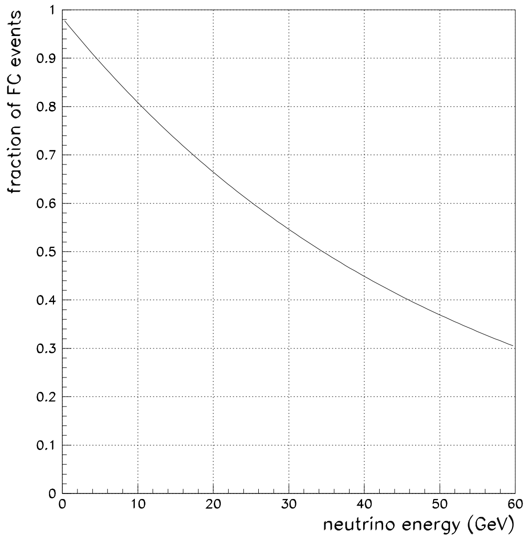

Figure 6.4: Fraction of FC charged current ν_μ interactions from CNGS beam as a function of neutrino energy.

muon momentum is reconstructed with an average resolution near 8% as shown in Fig. 6.5, nearly constant with the energy. Some pathological bad reconstructed events (see tails on the distribution, at some % level) still need to be fixed.

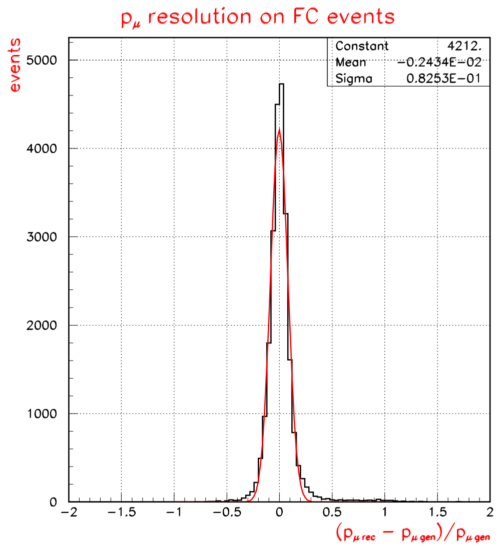

Figure 6.5: Resolution on reconstructed muon energy for FC events.

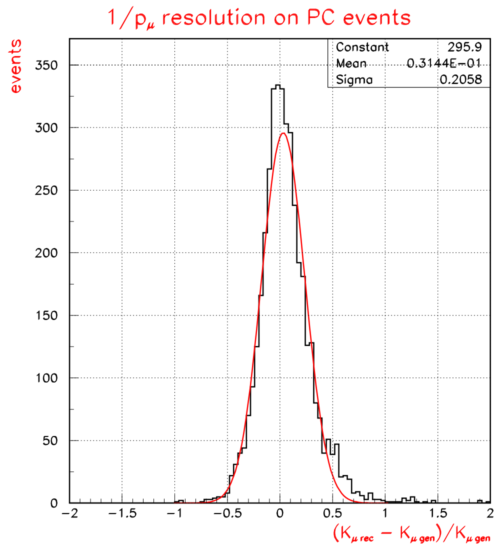

Figure 6.6: Resolution on reconstructed $K_\mu = 1/p_\mu$. (p_μ: muon momentum for PC events)

For partially contained (PC) events with an outgoing muon track, the muon momentum has been reconstructed fitting the track curvature in the magnetic field.

Due to the fact that event directions are near the horizontal and along the Y-axis of the detector, an optimised reordering of recorded hits have been implemented. In practice, the two selected views to analyze the events are the ZY and XY ones, no more (as for atmospheric neutrino) XZ and YZ, after suitable rearranging of hits.

The first stage of the reconstruction of muon momentum in the magnetic field, is to define a *candidate track*, that is a collection of hits in the two projections ordered along the y-axis. Each projection is modeled through a polinomial fit of order n, with $1 < n < 7$ depending on the number of hits in the projection. This track model is used to get the initial starting track directions dx/dy and dx/dy. These, together with the first hit x and z coordinates and a rough momentum estimate using the range, are the input to the track fit, based on a Kalman-filtering technique. Two tracking are performed on a candidate track: the first starts from the muon hit closer to the interaction point and follows the track up the last hit. The track parameters fitted at the end track point are then used as new starting values for a backtracking, which now proceeds to the muon hit closer to the vertex. The fit parameters (the two coordinates x and z, the two derivatives dx/dy and dz/dy and the signed inverse momentum K=q/P, with q $= \pm 1$) are therefore provided in the innermost point, closer to the interaction vertex. The average tracking in the magnetic field and covariance error matrix propagation are done using GEANE [93]. More details are given in ref. [94].

The fitting procedure provides, for each event, an estimate of the error σ_K on the reconstructed $K = 1/p$. For PC events, we select events with a $\sigma_K/K \leq 30\%$: the resolution reached for the uniform detector option on the PC sample is shown in Fig. 6.6. No explicit request on the number of hits have been made: however we checked that for selected tracks events with less than 7 hits are less than 8%.

On the PC sample selected, the resulting muon momentum resolution in the range of interest (0.- 60 GeV) is shown in Fig. 6.12 with full points for the uniform detector option. The resolution improves with muon energy because, due to the beam orientation with respect to the main detector axis, the selection of outgoing muons of increasing energy corresponds to an increasing number of hit collected and a larger integrated magnetic field by the track.

An hadronic energy reconstruction has been derived from the number of hits released by hadrons produced in neutrino interactions using MONOLITH as a digital calorimeter. A calibration curve optimised for the beam, slightly different from the one used, for atmospheric neutrino interaction has been developed. The hadronic energy resolution is found to agree with the parameterisation of the hadronic energy resolution estimated on atmospheric neutrinos events (see section 5.3.2).

On long-baseline events the resolution on L/E will be determined by the neutrino energy resolution. As for atmospheric neutrino analysis even with a coarse resolution to hadrons, the overall L/E resolution can be controlled by selection of neutrino interactions of limited inelasticity for small neutrino energies. From the expression of the relative L/E resolution (4.2), we have

$$\frac{\sigma(L/E)^2_{beam}}{(L/E)^2} = \frac{\sigma_E^2}{E^2} \simeq \frac{\sigma_{E_\mu}^2}{E_\mu^2}(1-y)^2 + \frac{\sigma_{E_h}^2}{E_h^2}y^2 \tag{6.1}$$

where E, E_μ and E_h are the neutrino, muon and hadronic energies, $y = E_h/E$ is the inelasticity of the interaction. So, for each event selected, we have estimated E_μ, E_h and y. Using eq. (6.1), and parametrisations of $\sigma(E_\mu)$ and $\sigma(E_h)$, we evaluate the relative $\sigma(L/E)$ on an event by event basis. We select the events for the analysis requiring $\sigma^2(E) \leq k^2E^2$, where we choose $k = 0.3$ as a compromise to mantain a global neutrino energy resolution less than 22% and good selection efficiency.

Summarizing, we select a sample for the analysis using three cuts:

1. the request of an hadronic hit to fix the vertex;

2. a request of at least 7 hits for the muon track for FC events or a request of good fit of the track for PC events;

3. the above discussed cut on the expected neutrino energy resolution.

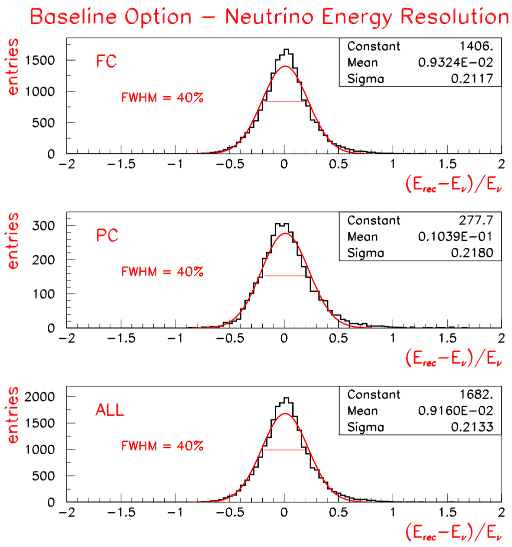

Figure 6.7: Resolution on reconstructed neutrino energy for the MONOLITH uniform detector option.

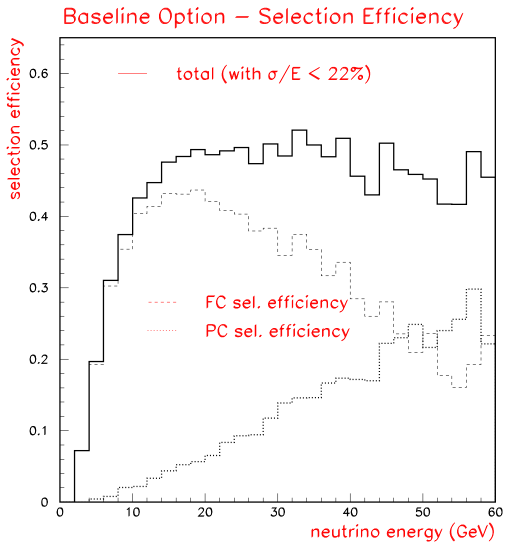

Figure 6.8: Selection efficiency for the MONOLITH uniform detector option for the discussed cuts.

6.2.1 Results for the uniform detector option

For the uniform detector option the neutrino energy resolution for PC, FC and the whole set are shown in Fig. 6.7. A neutrino energy resolution $\leq 22\%$ is achieved (an analysis of the FWHM due to the not perfect gaussian shape gives something better around 17%). The selection efficiency for the range 0-60 GeV is plotted in Fig. 6.8. It is defined as the ratio between the number of selected events and the generated one in a given bin of energy. From 16 GeV to 40 GeV nearly constant selection efficiency around 50% is obtained.

6.2.2 Results for the vertical end-caps option

We have also studied the configuration with the addition of some vertical iron planes to the MONOLITH uniform detector option to increase the efficiency on the CNGS beam.

To maintain a symmetric detector (taking into account that vertical planes can be also used successfully for atmospheric neutrinos as shown in 5.6), we investigated the performance of the setup shown in Fig. 6.9. Basically the horizontal plane dimensions are reduced to (26x15) m^2 and two 2 m long end caps are added at the beginning and at the end of the Y axis, made by vertical iron planes and GSC's. Assuming the "standard" MONOLITH spacing (e.g. 8 cm of iron, 2 cm to host GSCs) every endcap gives 20 active layers. In this configuration we have exactly the same total mass of the uniform detector option. We assume also the same design of the magnetic field for the iron plane of the uniform detector option.

The resolution and efficiencies achievable with this configuration are shown in Figg. 6.10 and 6.11. Of course the main gain is due to the increased efficiency for PC events, where outgoing track are best reconstructed due to the contribution of the last 20 vertical layers.

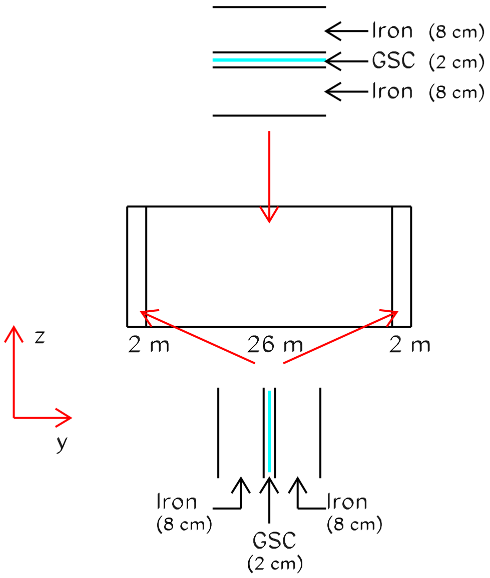

Figure 6.9: Side view of MONOLITH with the end-caps option.

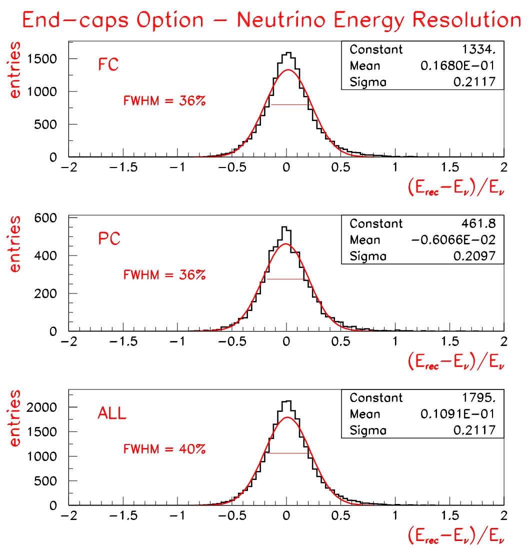

Figure 6.10: Resolution on reconstructed neutrino energy for the MONOLITH end-caps option.

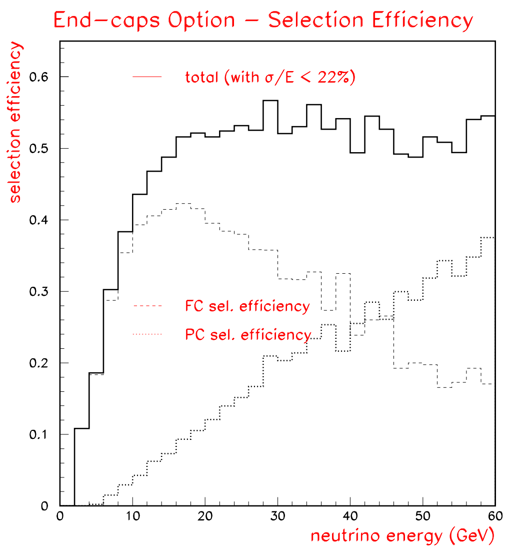

Figure 6.11: Selection efficiency for the MONOLITH end cap option for the discussed cuts.

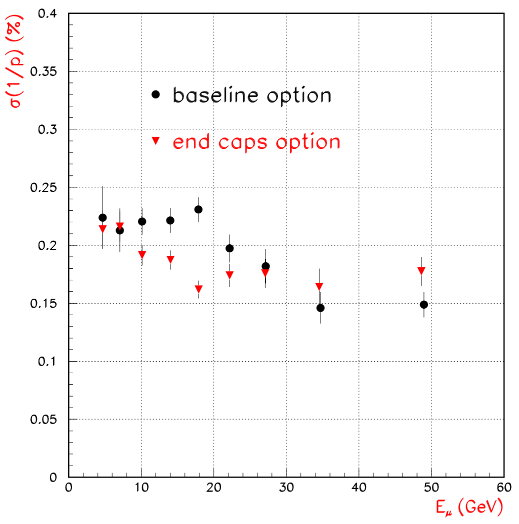

Figure 6.12: Resolution on reconstructed 1/p muon momentum as a function of muon energy for PC events in the two options.

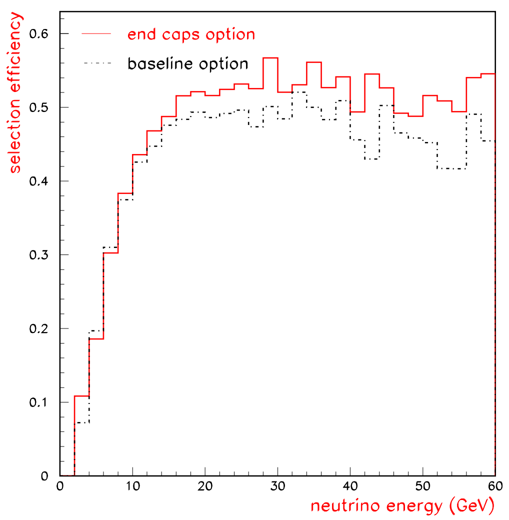

Figure 6.13: Comparison of the selection efficiency for the two options.

6.2.3 Comparison of the two set-ups

In Fig. 6.12 with full triangles the σ_K resolution is reported compared with the uniform detector option (full circles). Better resolution at smaller energies for outgoing tracks is obtained with the end caps.

In Fig. 6.13 the selection efficiency for the two setup is compared. As can be seen the vertical planes add efficiency and give a more flat behaviour at higher ($E > 40$ GeV) energies. A 10% increase of the selection efficiency with respect to the uniform detector option is obtained at 30 GeV. At higher energies (see Fig. 6.1) the beam intensity is rapidly decreasing, but we point out that this region is relevant to select an unoscillated sample of data, needed to normalize correctly the total luminosity of the beam.

6.3 Study of the oscillation pattern

In Fig. 6.14 we present the L/E distribution (no oscillation) measurable from the CNGS beam by MONOLITH in 1 year of data taking. The hatched area is the statistics that MONOLITH will collect from atmospheric neutrinos in 4 years of data taking (values of L for downgoing neutrinos have been mirrored).

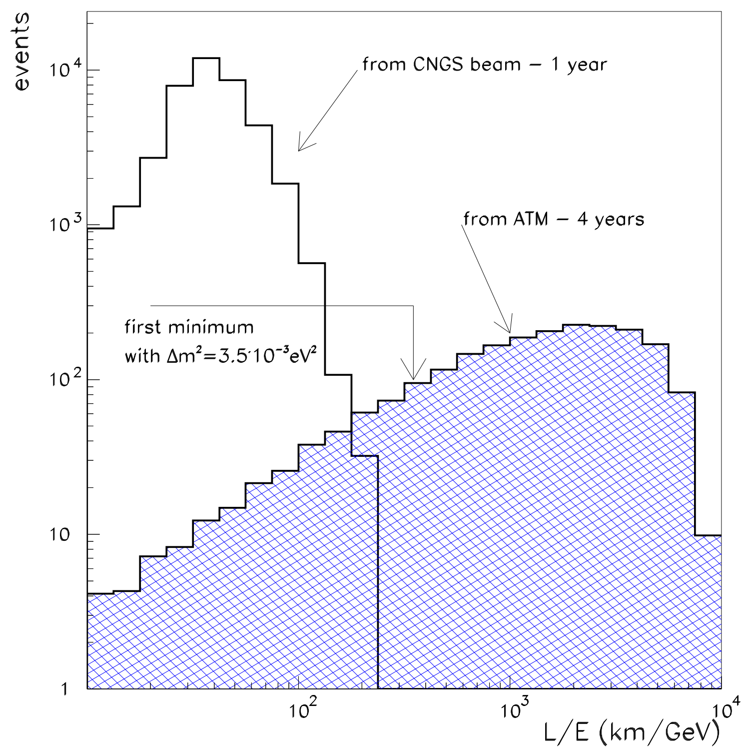

Figure 6.14: Number of events selected for the analysis by MONOLITH in 1 year of data taking from the CNGS beam. The statistics from atmospheric neutrinos is also shown.

Considering the most probable value of the first minimum of the oscillation pattern, according to current Super Kamiokande best fit, the complementarity of the two measurements becomes clear: the L/E data obtained by the CNGS beam will provide many events in the L/E region before the oscillation minimum, and can help to constrain the oscillation pattern in this region.

In Fig. 6.15 the measurable L/E distributions with respect to the expectations have been plotted for five different values of Δm^2 and maximal mixing. The survival probability convolved with the resolution function is also superimposed. To obtain the unoscillated expected distribution, after correction for the selection efficiency and the energy resolution smearing, we used the events from the CNGS beam with energy between 35 and 50 GeV, expected to be nearly completely unoscillated. The errors shown are computed assuming the *relative* beam shape and detector efficiency to be known at the 8% level.

A preliminar estimation of the impact of some systematic uncertainties has been performed.

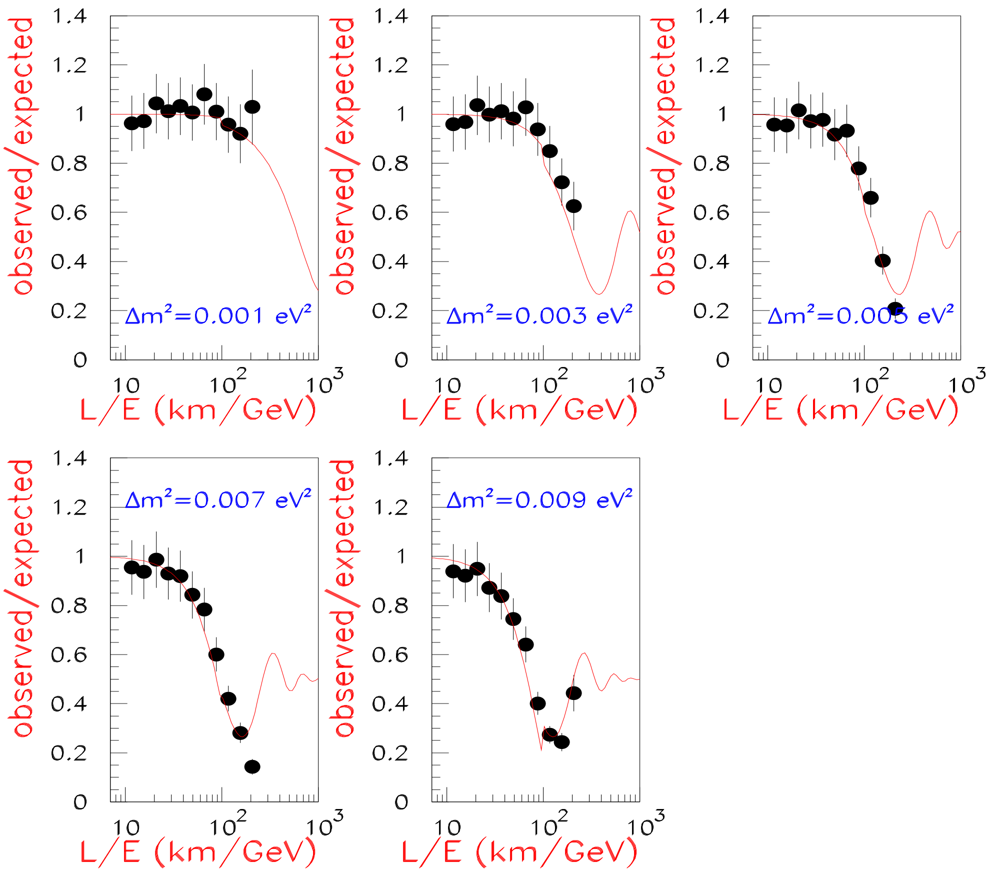

Figure 6.15: L/E distribution from the CNGS beam for five different values of Δm^2. To help following the shape, the survival probability is also superimposed.

The main sources of systematic error are related to the knowledge of the neutrino fluxes in the CNGS beam. The shape of the CNGS beam was changed according to the prediction of the beam parameterization of [95] in the simulated sample used as "data", while leaving the original shape [96] for the prediction in the absence of oscillation. The difference between the two spectra is within $\sim 10\%$ in almost all the energy bin, as shown in figure 6.16.

Finally, these measurements can be merged with atmospheric neutrino measurements to yield combined spectra like the one shown in fig. 6.17, which is obtained for $\Delta m^2 = 7\ 10^{-3}\ eV^2$. Four years of atmospheric data are combined with one year of CNGS data, assuming 10 % of systematic uncertainties. The improved statistic at low L/E values allow to better constrain the Δm^2, while the uncertainties does not permit to improve the $sin^2(2\theta)$ parameter.

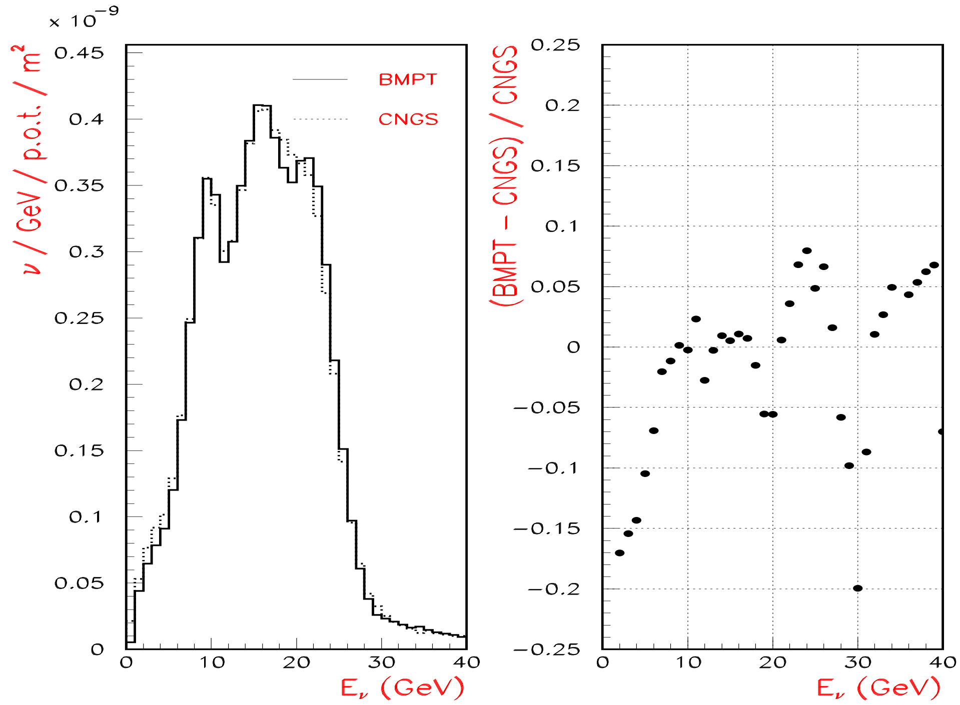

Figure 6.16: *Left:* Comparison between CNGS Geant/Fluka simulation (the dotted line) and the BMPT parametrized simulation (continuous line). *Right:* Percentage difference between the two calculations.

6.4 Summary and conclusions

We studied the performances of the detector in the analysis of the events produced by the CERN to Gran Sasso neutrino beam.

- Despite its design being optimised for atmospheric neutrinos, even the uniform detector option will allow to collect a huge amount of events from the beam with good resolution. An addition of vertical planes can increase the selection efficiency, in particular for $E_\nu \geq 15$ GeV.

- Depending on Δm^2 and assuming a 10% systematic uncertainty in beam shape, a deficit of events as a function of L/E can be seen in 1 year of data taking.

- The up/down analysis of MONOLITH from atmospheric neutrinos can be complemented by a big sample of data from the CNGS beam at small L/E to reduce statistical errors. Although this will make the analysis dependent on Monte Carlo and beam systematics, it will yield a useful complement, especially if Δm^2 lays in the upper part of the Super-Kamiokande allowed region. However, the systematic uncertainty due to the beam shape knowledge needs to be further investigated. The CNGS events also act as redundant consistency check for the first years of data taking.

- Given the high interaction rate ($\sim$ 40000 selected events per year), the MONOLITH experiment can act as a good quality monitor of the CNGS beam.

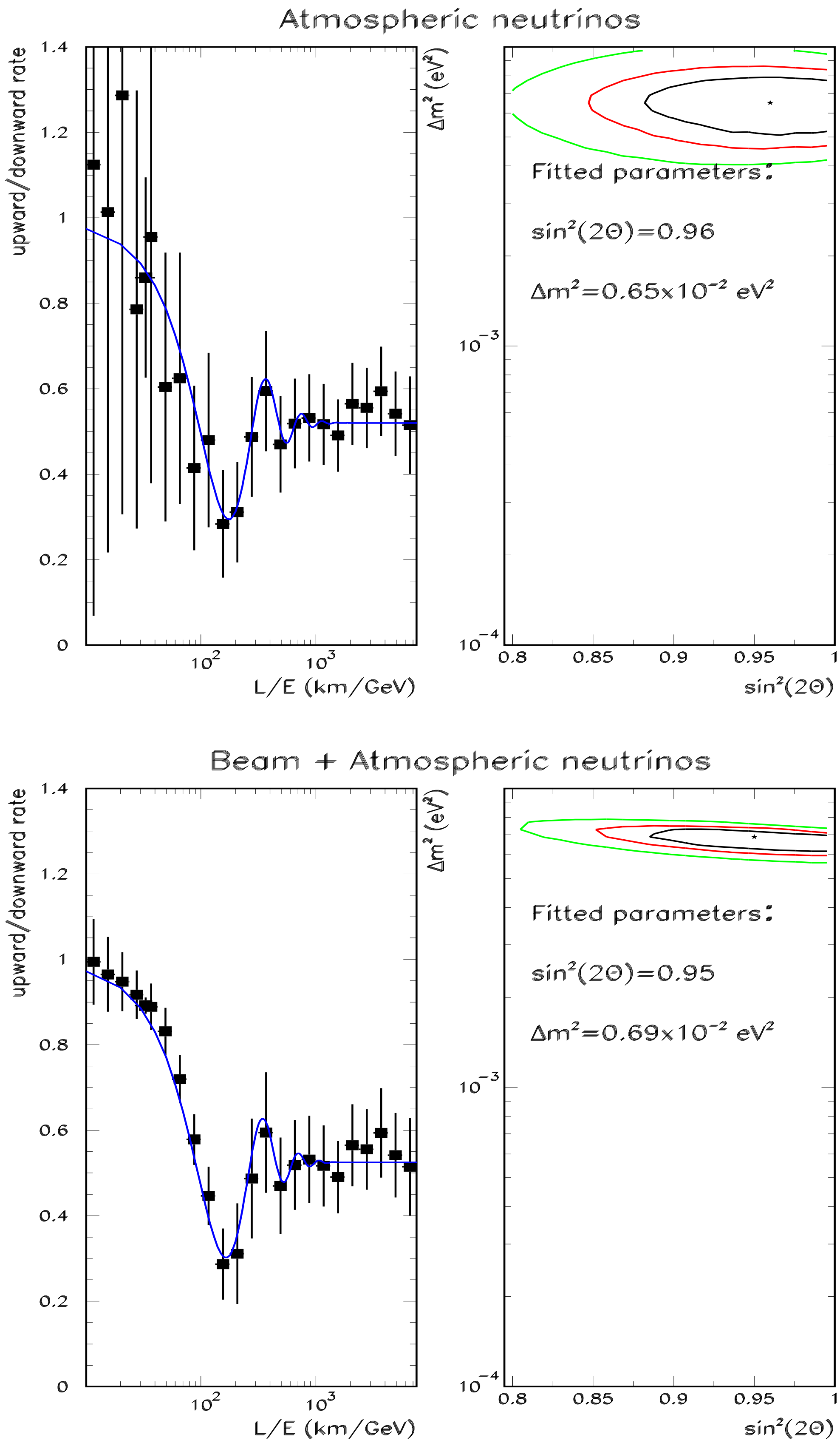

Figure 6.17: Comparison of parameter estimation capabilities between atmospherics (4 years) and a combination of beam (1 year) + atmospherics (4 years). The simulated Δm^2 is $7\,10^{-3}\ eV^2$.

Chapter 7

Physics at a Neutrino Factory

7.1 Introduction

The atmospheric [97, 98] plus solar [99] neutrino data point to neutrino oscillations [100, 26] and can be easily accommodated in a more general three-family mixing scenario.

Let U, with $(\nu_e, \nu_\mu, \nu_\tau)^T = U \cdot (\nu_1, \nu_2, \nu_3)^T$, be the leptonic Cabibbo-Kobayashi-Maskawa (CKM) matrix in its most conventional parametrization [16]:

$$U \equiv U_{23} U_{13} U_{12} \equiv \begin{pmatrix} 1 & 0 & 0 \\ 0 & c_{23} & s_{23} \\ 0 & -s_{23} & c_{23} \end{pmatrix} \begin{pmatrix} c_{13} & 0 & s_{13} e^{i\delta} \\ 0 & 1 & 0 \\ -s_{13} e^{-i\delta} & 0 & c_{13} \end{pmatrix} \begin{pmatrix} c_{12} & s_{12} & 0 \\ -s_{12} & c_{12} & 0 \\ 0 & 0 & 1 \end{pmatrix} \tag{7.1}$$

with $s_{12} \equiv \sin\theta_{12}$, and similarly for the other sines and cosines. Oscillation experiments are sensitive to the neutrino mass differences and the four parameters in the mixing matrix of Eq. (7.1): three angles and the Dirac CP-odd phase.

The SuperKamiokande [97] data on atmospheric neutrinos could be interpreted as oscillations of muon neutrinos into neutrinos that are not ν_e's, with a mass gap that we denote by Δm^2_{23}. Roughly speaking, the measured mixing angle θ_{23} is close to maximal and $|\Delta m^2_{23}|$ is in the range 10^{-3}–10^{-2} eV^2. The solar neutrino deficit is interpreted either as MSW (matter enhanced) oscillations [26] or as vacuum oscillations (VO) [100] that deplete the original ν_e's, presumably in favour of ν_μ's or alternatively into sterile neutrinos. The corresponding squared mass differences –$\mathcal{O}(10^{-5}$-$10^{-4})$ eV^2 for the large mixing angle MSW solution (LMA-MSW), $\mathcal{O}(10^{-6})$ eV^2 for the small mixing angle MSW solution (SMA-MSW), or $\mathcal{O}(10^{-10})$ eV^2 for VO– are significantly below the range deduced from atmospheric observations. We identify this mass difference with Δm^2_{12} in this parametrization. Its sign is constrained by solar data: while the SMA-MSW solution exists only for positive Δm^2_{12}, in the LMA-MSW range there is also a small window at negative values [101].

These oscillation signals will be confirmed and further constrained in ongoing and planned atmospheric, solar and long baseline reactor experiments [102], as well as in future long baseline accelerator neutrino experiments [103]. In a few years they will answer the question of sterile neutrinos contributing or not to present data. The MSW effect is expected to play a major role in explaining the solar deficit and both solar and reactor experiments will also clarify whether Nature has chosen the LMA-MSW rather than SMA-MSW or VO solutions.

The atmospheric neutrino parameters will be known with better precision, as shown in section 5, using the up-down symmetry of high energy atmospheric neutrinos and a detector with good L/E resolution as the massive magnetic calorimeter. Otherwise, if $|\Delta m^2_{23}|$ lays in the upper part of the SK allowed region, projected long baseline accelerator experiments will improve the precision of $|\Delta m^2_{23}|$ and θ_{23}. For instance, $|\Delta m^2_{23}|$ is expected to be measured at MINOS with an accuracy below 10% if $|\Delta m^2_{23}| > 3 \times 10^{-3}$ eV^2 [104].

Nevertheless, there is a strong case for going further in the fundamental quest of the neutrino masses and mixing angles, as a necessary step to unravel the fundamental new scale(s) behind neutrino oscillations. In ten years from now no significant improvement is expected in the knowledge of:

- The angle θ_{13}, which is the key between the atmospheric and solar neutrino realms, for which the present CHOOZ bound is $\sin^2\theta_{13} \leq 5 \times 10^{-2}$ [105][106].
- The sign of Δm^2_{23}, which determines whether the three-family neutrino spectrum is of the "hierarchical" or "degenerate" type (i.e. only one heavy state and two almost degenerate light ones, or the reverse).
- Leptonic CP-violation.
- The precise study of matter effects in the ν propagation through the Earth: a model-independent experimental confirmation of the MSW effect will not be available.

The most sensitive method to study these topics is to measure the transition probabilities involving ν_e and $\bar{\nu}_e$, in particular $\nu_e(\bar{\nu}_e) \to \nu_\mu(\bar{\nu}_\mu)$. This is precisely the golden measurement at the *neutrino factory* [107]. Such a facility is unique in providing high energy and intense $\nu_e(\bar{\nu}_e)$ beams coming from positive (negative) muons which decay in the straight sections of a muon storage ring [108]. Since these beams also contain $\bar{\nu}_\mu(\nu_\mu)$ (but no $\nu_\mu(\bar{\nu}_\mu)$!), the transitions of interest can be measured by searching for "wrong-sign" muons: negative (positive) muons appearing in a massive detector with good muon charge identification capabilities.

The first exploratory studies of the use of a neutrino beam with these characteristics [109] were made in the context of two-family mixing. In this approximation, the wrong-sign muon signal in the atmospheric range is absent, since the atmospheric oscillation is $\nu_\mu \leftrightarrow \nu_\tau$. The enormous physics reach of such signals in the context of three-family neutrino mixing was first realized in [110], where the authors put the emphasis on the measurement of the angle θ_{13} and CP-violation (see also [111]). The latter may be at reach if the solar deficit corresponds to the LMA-MSW solution [110, 112, 113]. It has also been shown [116] that the precision in the knowledge of the atmospheric parameters θ_{23} and $|\Delta m^2_{23}|$ can reach the percent level at a neutrino factory, using muon disappearance measurements. Furthermore, it was pointed out [114, 115, 116] that the sign of Δm^2_{23} can also be determined at long baselines, through sizeable matter effects. The importance of measuring precisely Earth matter effects in a clean and model-independent way, both for the understanding of the fundamental parameters and for their intrinsic interest has been stressed in refs. [117, 118, 119, 120].

We shall consider the following "reference set-up": neutrino beams resulting from the decay of $2 \times 10^{20} \mu^+$'s and/or μ^-'s per year in a straight section of an $E_\mu = 50$ GeV muon accumulator. A long baseline (LBL) experiment with a 34 kt detector and five years of data taking is considered. Alternatively, the same results could be reached in one year of running for the higher intensity option of the machine, providing 10^{21} useful μ^+'s and μ^-'s per year. The realistic simulation of the massive magnetized iron calorimeter described in section 4 will be considered and detailed estimates of the corresponding expected backgrounds and efficiencies will be included in the analysis. Two reference baselines are discussed: 732 km and 3500 km.

7.2 Fluxes and charged currents.

7.2.1 The Neutrino Factory

One of the conclusion of the first neutrino factory workshop, held at Lyon [121] in 1999, was the convergence of the various machine designs existing previously, to an essentially unified design [122], based on a muon accumulator with either a triangular or a bow-tie shape. Both geometries permit two straight sections pointing to different directions, allowing two different baselines.

It was also agreed in Lyon that the beam power on target should not exceed 4 MW. This, in turn, limits the production of muons to 10^{21} per year, out of which only 20-25 % are useful (that is, decay in the straight sections pointing towards the detectors). Agreement was also found upon other important parameters, namely the machine dual polarity (i.e, the ability to store μ^+ and μ^-, although not simultaneously) and the maximum realistic energy to accelerate the stored muons, which was fixed at 50 GeV.

Ultimate sensitivity to the neutrino mixing matrix parameters, in particular to θ_{13} and δ, require a data set as large as possible. The analysis presented in this chapter assumes a total data set of 10^{21} useful μ^+ decays.

A very schematic layout of the neutrino factory complex is shown in figure 7.1 with a view to illustrating its salient features.

The protons deliver a power of 4 MW onto a high-Z target. The target technology is very difficult, as very strong pressure waves have to be sustained. Also, a high amount of heat must be taken away from the target, as $\sim 25\%$ of the beam power is dissipated in the target. The target is embedded in a strong solenoidal field of some 20 T. The accepted forward-going pions are phase rotated, i.e. their momentum spread is reduced at the cost of bunch lengthening. After a drift space where the pions decay, the decay muons are "cooled" with a relatively moderate compression of the six-dimensional phase space by a factor of 75. Since muons are unstable (lifetime $\tau_\mu = 2.2\ \mu s$), all further actions on them must be highly efficient so as to accelerate them as quickly as possible to their final momentum, thus profiting to a maximum from Lorentz time dilation ($\beta\gamma = 1.0\ ms$ for circulating muons of 50 GeV/c momentum).

The cooled muons are first accelerated to $\sim 2\ GeV$, then they enter two recirculating linacs, where they are repeatedly accelerated in a straight section, and returned in recirculating arcs. Each arc is optimized for a certain momentum, rendering a number of discrete arcs necessary. For physics reasons, a momentum range up to 50 GeV/c is desired, where 50 GeV/c is a limit imposed by financial consideration rather than by physics objectives.

Finally, the muons enter the muon storage ring. It has two straight sections, each pointing to "far" detectors at different distances (say 732 km and 3500 km), implying inclination angles of 3° and 16°, respectively. The arcs are as short as possible. The two straight sections and the arcs are arranged in a near-planar geometry. One or several "near" detectors would be located

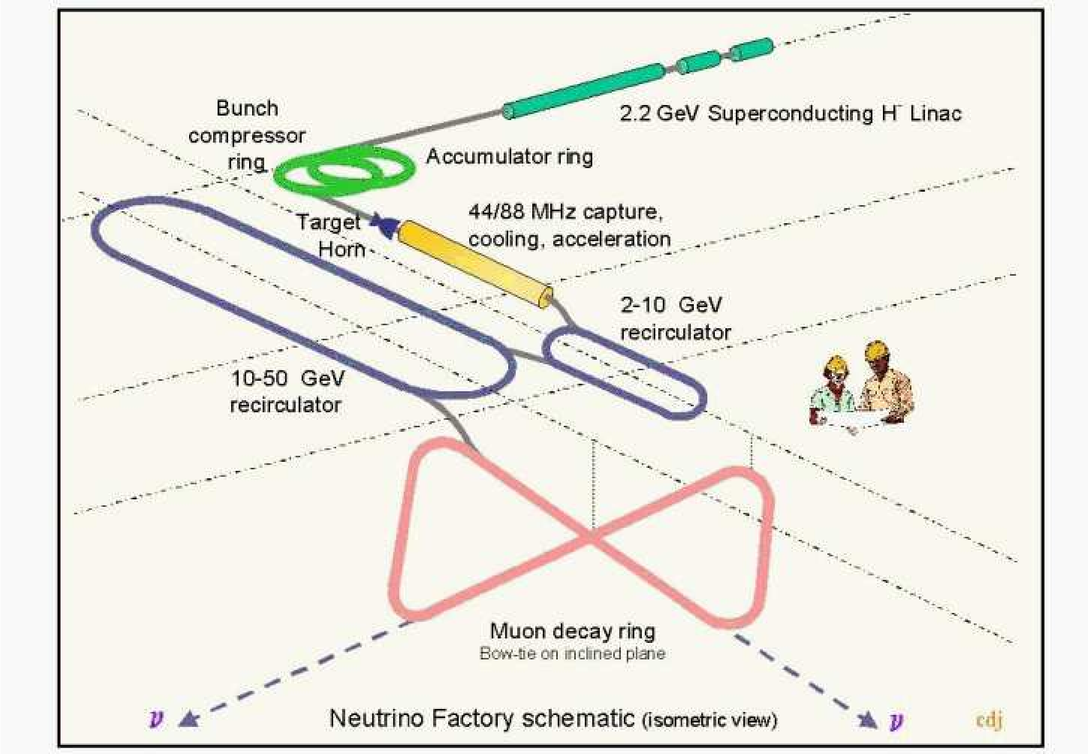

Figure 7.1: Generic layout of the neutrino factory complex.

at the end of one straight section.

While the overall design is considered feasible by the experts, it is recognized that a lot of R&D work must be successfully accomplished before a serious engineering design can be made. Particularly critical areas are the target zone and the muon cooling. The next few years are expected to be busy with a variety of dedicated R&D experiments.

7.2.2 Number of events

In the muon rest-frame, the distribution of muon antineutrinos (neutrinos) and electron neutrinos (antineutrinos) in the decay $\mu^\pm \to e^\pm + \nu_e(\bar\nu_e) + \bar\nu_\mu(\nu_\mu)$ is given by:

$$\frac{d^2N}{dx d\Omega} = \frac{1}{4\pi}[f_0(x) \mp \mathcal{P}_\mu f_1(x)\cos\theta]\,, \tag{7.2}$$

where E_ν denotes the neutrino energy, $x = 2E_\nu/m_\mu$ and $\mathcal{P}_\mu$ is the average muon polarization along the beam directions. θ is the angle between the neutrino momentum vector and the muon spin direction and m_μ is the muon mass. The positron (electron) flux is identical to that for muon neutrinos (antineutrinos), when the electron mass is neglected. The functions f_0 and f_1 are given in Table 7.1 [123].

In the laboratory frame, the neutrino fluxes, boosted along the muon momentum vector, are given by:

$$\frac{d^2N_{\bar\nu_\mu,\nu_\mu}}{dy d\Omega} = \frac{4n_\mu}{\pi L^2 m_\mu^6}\; E_\mu^4 y^2\,(1-\beta\cos\varphi)\; \Big\{\Big[3m_\mu^2 - 4E_\mu^2 y\,(1-\beta\cos\varphi)\Big]$$

	$f_0(x)$	$f_1(x)$
ν_μ, e	$2x^2(3-2x)$	$2x^2(1-2x)$
ν_e	$12x^2(1-x)$	$12x^2(1-x)$

Table 7.1: Flux functions in the muon rest-frame as in ref. [123].

$$\mp \mathcal{P}_\mu \left[m_\mu^2 - 4E_\mu^2 y\,(1-\beta\cos\varphi) \right] \Big\} ,$$

$$\frac{d^2 N_{\nu_e,\bar\nu_e}}{dy d\Omega} = \frac{24 n_\mu}{\pi L^2 m_\mu^6} E_\mu^4 y^2 (1-\beta\cos\varphi) \Big\{ \left[m_\mu^2 - 2E_\mu^2 y\,(1-\beta\cos\varphi) \right] \mp \mathcal{P}_\mu \left[m_\mu^2 - 2E_\mu^2 y\,(1-\beta\cos\varphi) \right] \Big\} . \tag{7.3}$$

Here, $\beta = \sqrt{1 - m_\mu^2/E_\mu^2}$, E_μ is the parent muon energy, $y = E_\nu/E_\mu$, n_μ is the number of useful muons per year obtained from the storage ring and L is the distance to the detector. φ is the angle between the beam axis and the direction pointing towards the detector, assumed to be located in the forward direction of the muon beam. The angular divergence will be taken as constant, $\delta\varphi \sim 0.1$ mr.

Unlike traditional neutrino beams obtained from π and K decays, the fluxes in Eq. (7.3), in the forward direction, present a leading quadratic dependence on E_ν. As a consequence, the oscillation signal does not decrease with increasing E_μ.

The charged current neutrino and antineutrino interaction rates can be computed using the approximate expressions for the neutrino-nucleon cross sections with an isoscalar target,

$$\sigma_{\nu N} \approx 0.67 \times 10^{-42} \times \frac{E_\nu}{\text{GeV}} \times \text{m}^2 , \qquad \sigma_{\bar\nu N} \approx 0.34 \times 10^{-42} \times \frac{E_\nu}{\text{GeV}} \times \text{m}^2 . \tag{7.4}$$

It follows that the number of charged current (CC) events at a neutrino factory scales cubically with energy.

The energy spectrum of the $\bar\nu_\mu$ CC interaction and the resulting μ^+ energy spectrum are shown in figure 7.2, assuming that muons are accelerated up to 50 GeV. In the analysis we use μ^+, instead of μ^-, because the signal-to-noise ratio is higher, due to the differences in cross-section between neutrinos and anti-neutrinos.

7.3 Oscillation Probability

We develop the analysis in a 3-flavour scheme, using vacuum oscillation probability, since the baseline under study is 732 km (CERN-LNGS). Matter effects become important over $O(3000\ km)$, so vacuum oscillation probability should be used also for the second baseline studied (3500 km).

For a 50 GeV ν-factory, the energy range is such that $\Delta m^2 L/E_\nu \ll 1$ for the smaller (Δm_{12}^2) but not necessarily for the larger (Δm_{23}^2) of the mass gaps. Even then, solar and atmospheric transitions are not (provided $\theta_{13} \neq 0$) two separate two-generation oscillations. For $|\Delta m_{12}^2| \ll |\Delta m_{23}^2|$, neutrino oscillation probabilities at terrestrial distances are accurately described by only three parameters, θ_{23}, $\Delta m_{23}^2 = \Delta m_{13}^2$ and θ_{13}:

$$P_{\nu_e\nu_\mu(\bar\nu_e\bar\nu_\mu)} = s_{23}^2 \sin^2 2\theta_{13} \sin^2\left(\frac{\Delta_{13} L}{2}\right) ,$$

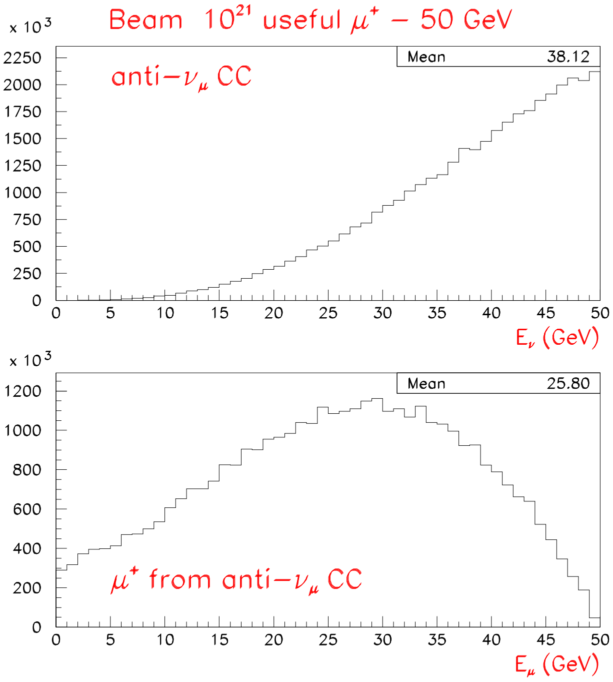

Figure 7.2: *Top:* $\bar{\nu}_\mu$ CC interaction energy spectrum. *Bottom:* μ^+ energy spectrum

$$
\begin{aligned}
P_{\nu_e\nu_\tau(\bar{\nu}_e\bar{\nu}_\tau)} &= c_{23}^2 \sin^2 2\theta_{13} \sin^2\left(\frac{\Delta_{13}\,L}{2}\right) , \\
P_{\nu_\mu\nu_\tau(\bar{\nu}_\mu\bar{\nu}_\tau)} &= c_{13}^4 \sin^2 2\theta_{23} \sin^2\left(\frac{\Delta_{13}\,L}{2}\right) ,
\end{aligned} \tag{7.5}
$$

where

$$\Delta_{ij} \equiv \frac{\Delta m_{ij}^2}{2E_\nu} . \tag{7.6}$$

The present best fit value for θ_{13} is in the range 6°–8°[124, 125], although it is compatible with zero within errors.

The energy spectrum of the ν_e CC interaction is shown in figure 7.3-*top* together with the oscillation probability $\nu_e \to \nu_\mu$. The oscillation parameters values for this analysis are $\theta_{13} = 13°$, $\theta_{23} = 45°$ and $\Delta m_{23}^2 = 4 \times 10^{-3}$, as chosen in [126], in order to compare results with the Large Magnetic Detector (LMD) analysis. Notice however that results for the fractional background and efficiencies should be rather insensitive to the particular choice of parameters. In figure 7.3-*centre* is shown the ν_μ CC interaction spectrum coming from oscillated ν_e and in figure 7.3-*bottom* the corresponding μ^- spectrum inside the apparatus. The signal spectrum has a lower energy with respect to the background one, as it can be seen comparing figures 7.2-*bottom* and 7.3-*bottom*. This will be important in the resulting efficiencies and fractional background.

Table 7.2 shows the number of interactions corresponding to a total of 10^{21} useful μ^+ decays and a 34 kt detector at our reference baselines.

The background is essentially related to the beam intensity, so it scales as $1/L^2$; the signal is related to the beam intensity and the oscillation probability, so it scales as $\frac{1}{L^2} sin^2(\frac{\Delta m^2 L}{E})$ and

Baseline (km)	$\bar{\nu}_\mu$ CC	ν_e CC	$\bar{\nu}_\mu + \nu_e$ NC	ν_μ (signal)
732	3.0×10^7	5.0×10^7	2.6×10^7	0.94×10^5
3500	1.0×10^6	2.0×10^6	1.0×10^6	0.85×10^5

Table 7.2: *Data samples expected in a 34 kt detector for* 10^{21} *useful* μ^+ *decays.* $\nu_e \to \nu_\mu$ *oscillations with parameters as in text.*

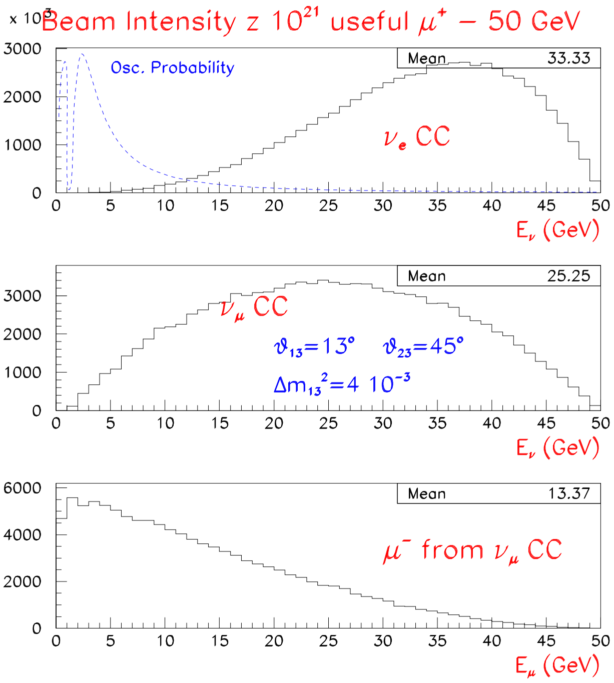

Figure 7.3: *Top:* ν_e CC interaction energy spectrum and oscillation probability (scaled up for graphics reasons) for oscillation parameters described in text. *Centre:* ν_μ energy spectrum *Bottom:* μ^- energy spectrum

it results almost constant in L. (This is true below 3500 km. For higher distances the sinus is no more linear and, moreover, matter effects become important). The signal-over-noise ratio is, thus, better at 3500 km than at 732 km.

7.4 Search for wrong-sign muon events

We consider the ($\bar{\nu}_\mu$, ν_e) neutrino beam from a μ^+ beam of $E_\mu = 50$ GeV (the dependence of the backgrounds with the energy of the muon beam was discussed in [127], where it was shown that optimal performance is obtained at the highest possible energy). The bulk of the events in the detector are $\bar{\nu}_\mu$ charged currents, signaled by the presence of a positive primary muon in the event, $\bar{\nu}_\mu$ and ν_e neutral currents, which are events with no primary leptons, and ν_e charged currents, for which we assume that the primary electron is not identified. On top of those events, one searches for wrong sign μ^- arising from the ν_μ produced via the oscillation $\nu_e \to \nu_\mu$.

7.5 Background sources

The potential backgrounds to the wrong sign μ^- events signalling the presence of oscillations are:

- events in which the charge is wrongly assigned,
- wrong sign muons from the hadronic part of the CC interaction.

We will examine the way to reject these background sources in detail in the following sections.

7.5.1 Charge misidentification

A source of background is given by the errors in the muon charge identification.
In order to study the efficiency and the background rejection power, we generate, using the Lipari event generator [128], 5×10^5 $\bar{\nu}_\mu$ CC interactions, sampled according to the spectrum in figure 7.2-*top* (background) and 1×10^5 ν_μ CC interactions accordingly to 7.3-*centre* (signal).
The detector structure, the digital response and the real magnetic field are simulated with the GEANT package.
The muon track is then fitted using the GEANE package [93] and the Kalman filter technique, developed for the CNGS beam analysis. The muon momentum is estimated from range, for contained events, and from curvature in magnetic field, for outgoing events (see chapter 6 for further details on the muon reconstruction technique).

Given the magnetic field structure of figure 5.1 it is quite easy to see the difference between a μ^+ and a μ^- events, that present an opposite curvature while traversing the detector, as shown in figure 7.4. The vertical red lines delimit the regions in which the magnetic field lines point towards the same direction along the x axis. An inversion in the track curvature (positive or negative) is observable when the track spans more than one region. We perform a parabolic fit in each of these regions and we check the sign of the leading term of the parabola, that is related to the charge of the muon.

In order to reduce the charge misidentification we ask the event to have

- P_μ from range greater than 5 GeV,

and we make the parabolic fit in the regions where

- there are at least 4 muon hits
- the muon spans at least 300 cm.

We accept the event if the results of the fits in each region are consistent to each other, otherwise the event is not used in the analysis. Furthermore, we need to reject events that have hits in the two lateral parts of the detector, with respect to the beam direction (we ask that the event has no hits with $x < 150$ cm and $x > 1350$ cm, see chapter 6 for the axis definition),

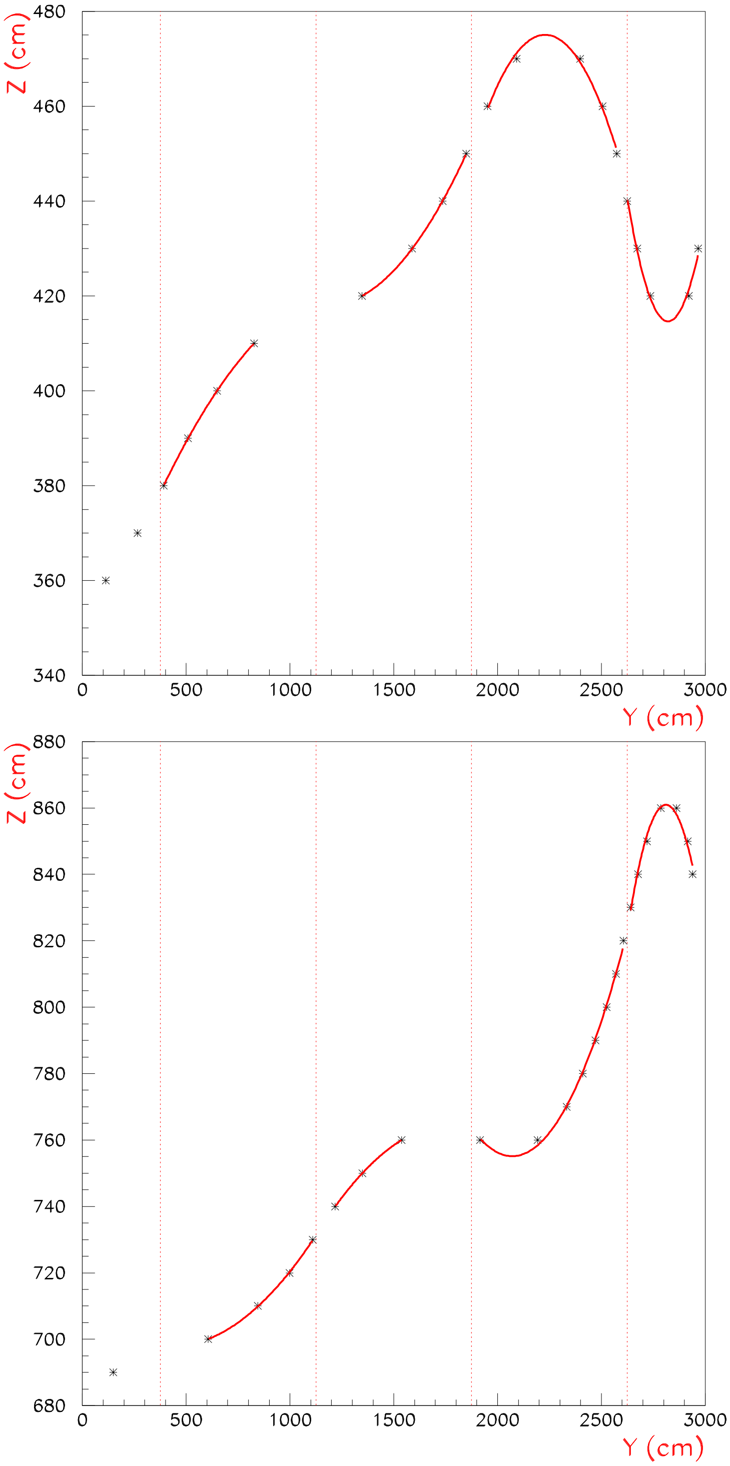

Figure 7.4: *Top:* Side view event display of a μ^- (signal) in the apparatus. The vertical dashed lines indicate the position in which the magnetic field lines change direction, causing the inversion in track curvature; the black asterisk are the muon hits and the continuous red lines are the result of a parabolic fit in each region. *Bottom:* The same for μ^+ (background)

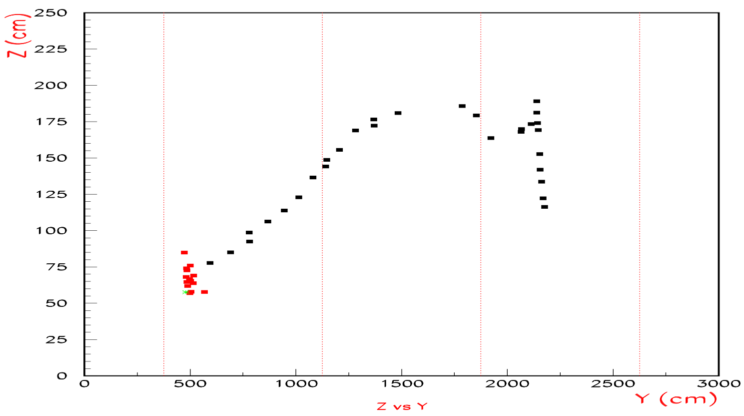

Figure 7.5: Side view event display of a μ^+ (background) in the apparatus where a large angle scattering is occurred in the final part of the track.

in which the magnetic field lines are parallel to the incoming track and are not able to bend it enough.

There is a sample of background events (μ^+) that survive the outlined cuts; they are due to a large angle scattering in their evolution through the detector, as in figure 7.5. It is known (see for example the Opera proposal [49] for a detailed discussion) that this process is overestimated in the Geant simulation; moreover a dedicated procedure to recognize events in which there is a non continuous change in the slope of the track is possible (for example, looking at the changes in the Kalman filter evolution), so these kind of background events could be removed.

After the selection cuts the signal efficiency is 34%, while the fractional background is 10^{-6}.

7.5.2 Wrong sign muons from hadrons

In this category there are various typologies of events:

1. $\bar{\nu}_\mu$ CC events in which the positive muon is not detected, and a secondary negative muon arising from the decay of π^-, K^- and D^- hadrons fakes the signal. The most dangerous events are those with $D^- \to \mu^-$, which yield an energetic muon with a spectrum similar to the signal.

2. ν_e CC events, for which it is assumed that the primary electron is never detected. Charm production is not important for this type of events since the charmed hadrons in the hadronic jet are predominantly positive. On the contrary, fake μ^- arise from the decay of negative pions and kaons in the hadronic jet.

3. $\bar{\nu}_\mu$ and ν_e NC events. Fake μ^- arise in this case also predominantly from the decay of negative pions and kaons, since charm production is suppressed with respect to the case of CC.

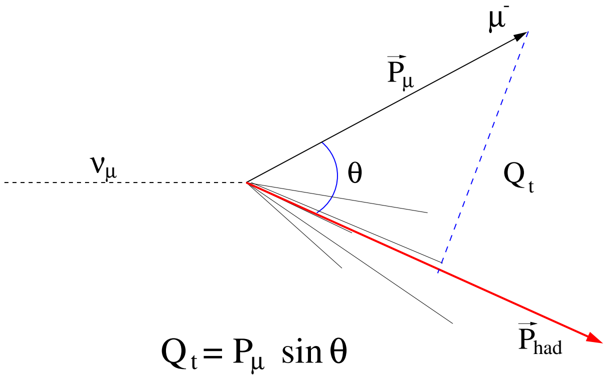

Figure 7.6: Definition of the kinematical variables used in this study.

In [126] and [130] it is shown that these backgrounds can be efficiently suppressed using two cuts:

- the momentum of the muon, $P_\mu > 5\ GeV$
- a variable measuring the isolation of the muon, $Q_t \equiv P_\mu \sin^2\theta > 1.4\ GeV$ (see figure 7.6).

The first cut is easily reproducible with the MONOLITH detector. The second one has to be dealt with carefully. It strongly depends on the hadronic angular resolution.

A first approach could be to use only a strong cut in muon momentum, say $P_\mu > 20\ GeV$. The signal efficiency decreases to 11% and the fractional backgrounds, as shown in [126], become

$\bar{\nu}_\mu$ CC	ν_e CC	$\bar{\nu}_\mu + \nu_e$ NC	ν_μ (signal)
$3.\ 10^{-6}$	$1.\ 10^{-8}$	$1.\ 10^{-6}$	11%

Otherwise, to use the Q_t cut it is necessary to perform a detailed study of the hadronic shower direction reconstruction.

Hadron angle

We have estimated the ability of MONOLITH to determine the direction of hadronic showers. We generate 6×10^5 ν CC interaction in the correct ν-factory energy range. Each event was required to have at least 2 hadronic hits. The centroid of the shower is formed by summing over the positions of the hits in the events and extracting the average value in each read-out view. A vector is then drawn from the event vertex, reconstructed as the first hadronic hit from the CERN direction, and the shower centre. Despite the coarse granularity of the detector, resolutions of the order of 5 cm on the vertex position are achievable on each coordinate (see figure 7.7). However this finite resolution introduce a large uncertainty in the direction reconstruction. A pictorial example of the technique used to determine the hadron shower direction and the impact of vertex reconstruction is shown in figure 7.8. The angle between the reconstructed shower direction and

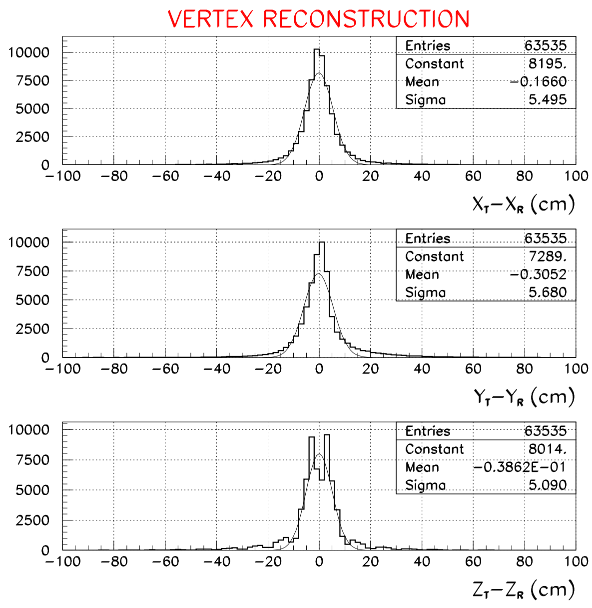

Figure 7.7: Vertex resolution in the transversal *(top)*, longitudinal *(center)* and vertical *(bottom)* coordinate for the 8 cm horizontal planes option.

the true shower direction is then calculated. At each energy bin, the resulting distribution in θ_{space}, the space angle between the true and reconstructed directions, is plotted and fitted to a two parameter function of the form:

$$N(\theta_{space}) = \frac{N}{2\pi\theta_0^2}\ exp(\frac{\theta_{space}^2}{-2\theta_0^2})d\Omega \tag{7.7}$$

The hadron shower angular resolutions calculated in this way are shown in figure 7.9 where, in order to improve the resolution, various detector configurations are taken into account. We try both to change the iron plane thickness and the plane orientation to see which configuration gives the better improvement. The vertex resolution for the vertical 8 cm planes is also shown in figure 7.10; the resolution is a factor 2 better than for horizontal planes (figure 7.7).

The hadron shower angular resolutions can be parametrized over the energy range by

$$\theta_0 = \frac{A}{\sqrt{E}} + \frac{B}{E} \tag{7.8}$$

with θ_0 in degrees and E in GeV.
The fits are superimposed in figure 7.9.
In the LMD analysis they choose to use the MINOS results for the hadron shower angular resolution [129] as reference detector performance: they obtained $A = 16.67\ GeV^{1/2}$ and $B = 12.15\ GeV$. It is important to notice that the MONOLITH and the MINOS analysis are the same, but MINOS uses the true vertex information for the determination of the direction, so the MONOLITH analysis is more realistic.

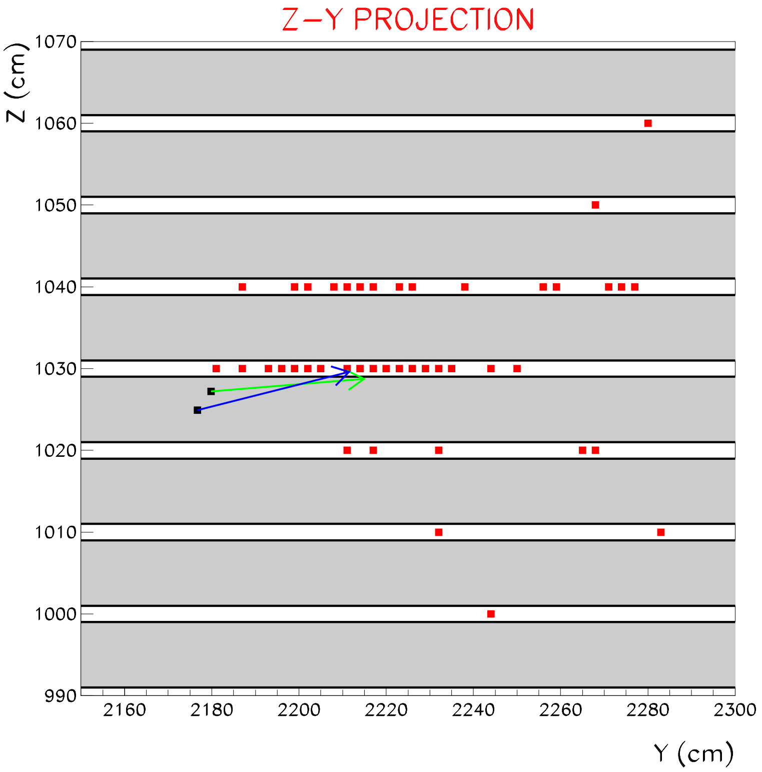

Figure 7.8: Event display of the ZY projection (side view) of an hadronic interaction. The blue arrow shows the true hadronic shower vector, the green arrow shows the reconstructed one, from reconstructed vertex to reconstructed centre of gravity of the shower.

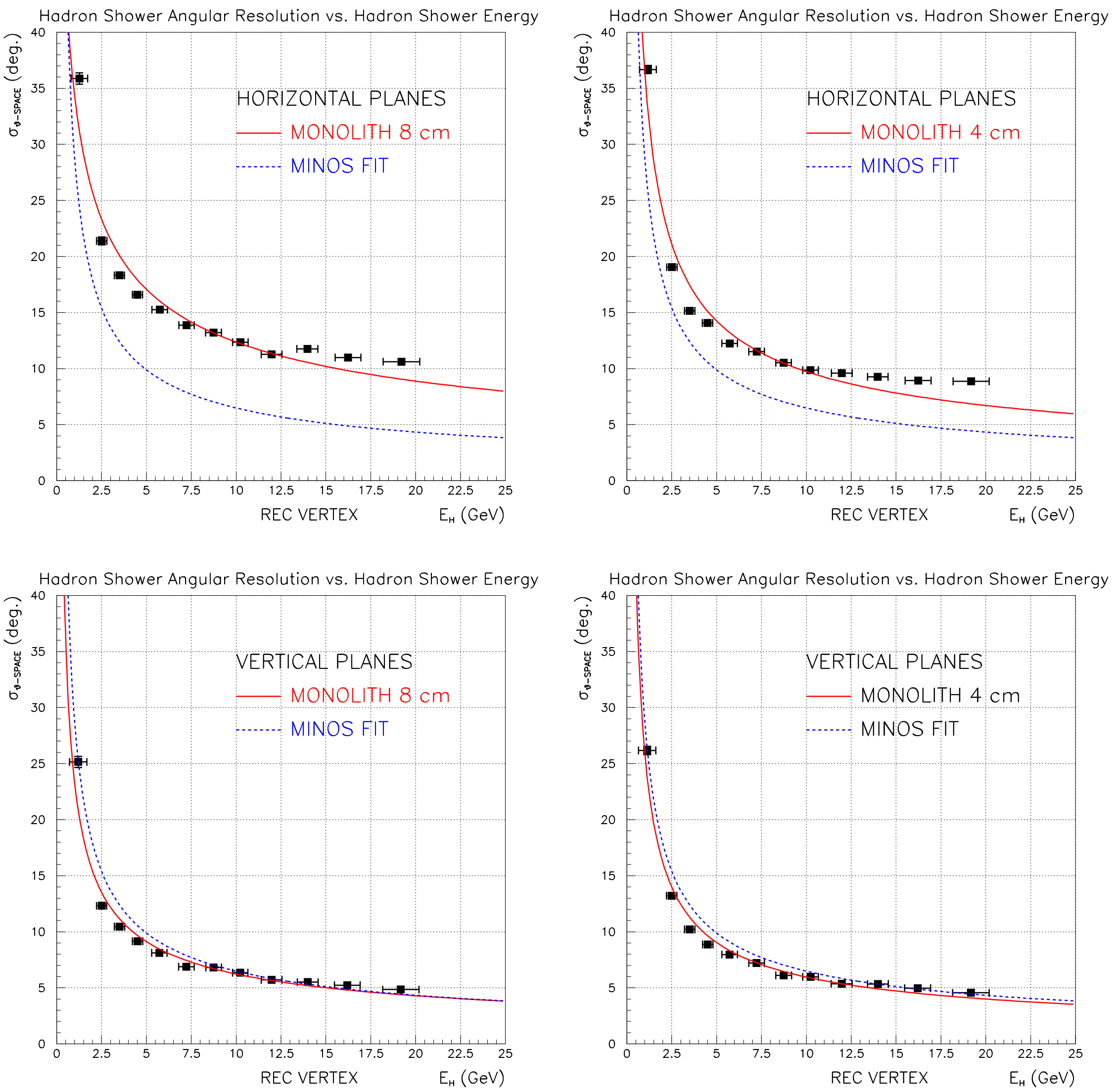

Figure 7.9: Hadron shower angular resolutions of the MONOLITH detector. *Top-Left:* horizontal 8 *cm* planes. *Top-Right:* horizontal 4 *cm* planes. *Bottom-Left:* vertical 8 *cm* planes. *Bottom-Right:* vertical 4 *cm* planes. Each one is compared with the MINOS fit (blue dashed line).

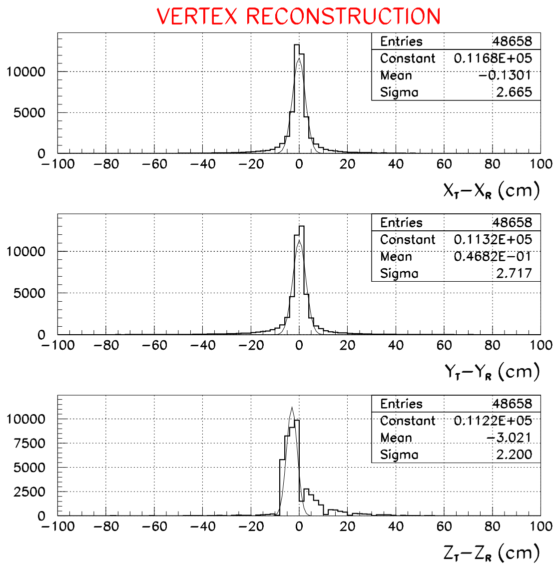

Figure 7.10: Vertex resolution in the transversal *(top)*, longitudinal *(centre)* and vertical *(bottom)* coordinate for the 8 *cm* vertical planes option.

The resolution for the MONOLITH base option (horizontal planes-8 *cm*) is about twice the MINOS (LMD) one, for the whole energy range; a bit lower in the horizontal-4 *cm* option and very similar to MINOS both in the vertical-8 *cm* and vertical-4 *cm*. The most important improvement is the orientation of the iron planes from horizontal (parallel to the incoming beam) to vertical (orthogonal to the beam); the calorimeter sampling (from 8 *cm* to 4 *cm*) does not significantly improve the performances. Fixing the B parameter in the fit to the MINOS value (12.15 GeV), the resulting A parameter for the different MONOLITH options are shown in table 7.3.

Having different hadronic shower direction resolution, the ability to reject the backgrounds varies. Following the analysis in [126] and [130], the scale factor for the fractional background (i.e. how bigger is the MONOLITH fractional background w.r.t. MINOS) could be estimated for each detector configuration and it is shown in table 7.3 as well as the resulting fractional backgrounds.

Detector config.	A ($GeV^{1/2}$)	Scale factor	F_{bkg} $\bar{\nu}_\mu$ CC	F_{bkg} ν_e CC	F_{bkg} ν NC
Horizontal-8 *cm*	32.	3.	3.3×10^{-6}	3.0×10^{-7}	6.0×10^{-7}
Horizontal-4 *cm*	26.	2.4	2.6×10^{-6}	2.4×10^{-7}	4.8×10^{-7}
Vertical-8 *cm*	16.	1.	1.1×10^{-6}	1.0×10^{-7}	2.0×10^{-7}

Table 7.3: *Fitted parameter, scale factor and fractional backgrounds for the wrong sign muon search with μ^+ decays (various MONOLITH option).*

Once taken into account properly the different hadronic angular resolution (and so the different rejection power) the LMD analysis is fully reproducible. We apply the same cuts ($P_\mu > 5\ GeV$ and $Q_t > 1.4\ GeV$) and the efficiency over the signal sample, including also the charge identification cuts, results 16%.

A summary of the number of background and signal events surviving cuts are reported in table 7.4. The fractional background and efficiency are conservatively assumed to be the same as in the base option also in the Horizontal-4 cm and Vertical-8 cm, even if improvements are expected in both configurations.

Detector config.	$\bar{\nu}_\mu$ CC wrong charge	$\bar{\nu}_\mu$ CC	ν_e CC	$\bar{\nu}_\mu + \nu_e$ NC	ν_μ (signal)
Horizontal-8 cm (only P_μ cut)	30	90	0.5	26	1.06×10^4
Horizontal-8 cm	30	100	15	16	1.5×10^4
Horizontal-4 cm	30	80	12	13	1.5×10^4
Vertical-8 cm	30	33	5	5	1.5×10^4

Table 7.4: *Events surviving cuts in a 34 kt detector for 10^{21} useful μ^+ decays. Oscillation parameters as in section 7.3*

7.6 $sin^2(2\theta_{13})$ sensitivity

To show the performance of the MONOLITH detector we study the θ_{13} sensitivity.

Given the oscillation probability in formula 7.5, the number of signal events is calculated for each value of Δm^2_{23} and θ_{13}, while θ_{23} is kept fixed at 45°. The sensitivity region in the parameter space is the one where

$$N_{signal} > 4\sigma_{bkg}$$

where N_{signal} is the number of signal events for the current parameters and σ_{bkg} is the error in the background estimation, calculated summing in quadrature the statistical error and a 5% systematic error. Signal efficiency and background rejection are taken into account for each detector configuration.

The results are shown in figure 7.11 for the MONOLITH base option (P_μ cut and combined P_μ and Q_t cuts), and for the vertical planes option. The Chooz excluded region [105] is superimposed as well as the sensitivity region of the future JHF SuperBeam (OAB 2° option) [131]. The 90% $C.L.$ Super-Kamiokande region of Δm^2_{23} is shown with the current best fit value of $3\ 10^{-3}$. The Monolith sensitivity region is two order of magnitude below the current limit and about one order of magnitude below the reach of a SuperBeam, even in the easiest approach (just P_μ cut), providing a very robust capability in extending the current limits on θ_{13} sensitivity.
If we change the baseline from 732 km to 3500 km (that are, for instance, CERN-Gran Sasso and CERN-Canary Island respectively) the background events scale as L^{-2} while the signal remains almost constant (the growing oscillation probability compensates the lower flux), so the sensitivity extends to lower θ_{13} values, as shown in figure 7.12.
The improvement expected having a 100 kt detector (instead of a 34 kt one) for the same

exposure (5 years of data taking at the nominal intensity of 2×10^{20} decaying muons per year) is shown in figure 7.13.

7.7 Test beam measurements of the hadronic shower direction

We use the data collected during a test at the CERN PS T7 beam, with the prototype described in section 4.8 to evaluate the ability to reconstruct the hadron shower direction. Here we remind of the main characteristics of the prototype and of the beam.
The test prototype is made of 20 iron planes (100×100 cm^2) 5 cm thick, 2 cm apart, interleaved with 20 active detector planes. The readout system is based on the use of flat cables acting as 96 1cm wide pick-up strips.
The CERN PS T7 beam provides particles (mainly pions) in the range between 2 and 10 GeV. Figure 7.14 shows the typical pattern for a 10 GeV pion taken from the online event display. The muons, selected as events traversing a 1 m thick iron block placed behind the prototype, are used to estimate the true beam direction; an example of a muon event is shown in figure 7.14 and the distribution of the muon direction is in figure 7.15 showing an uncertainty of 1°.

For each selected pion event, we apply the direction reconstruction technique outlined in section 7.5.2 and we compare the true direction with the reconstructed one (see figure 7.16). The angular distribution is evaluated at each pion energy bin and the resulting resolution θ_0 (see formula 7.7) is plotted in figure 7.17. The experimental data are fitted using the function 7.8 and compared with the reference MINOS fit.

The strip width in the prototype calorimeter is 1 cm; putting in OR three adjacent strip it is possible to simulate the performances of a 3 cm strip width. Moreover, taking into account in the analysis only the hits related to even (or odd) active planes, we are able to study a 10 cm thick calorimeter.
From figure 7.17 we can conclude that, even in the worst case presented that is a 10 cm thick iron calorimeter orthogonal to the beam with 3 cm strip width, it is possible to reach the requested performances, that is the MINOS one, in the hadronic angular resolution. In this way we prove with experimental data the simulations described in this chapter, providing a robust indication that the outlined detector geometry fulfills the requirement for the study of the wrong sign muon events.

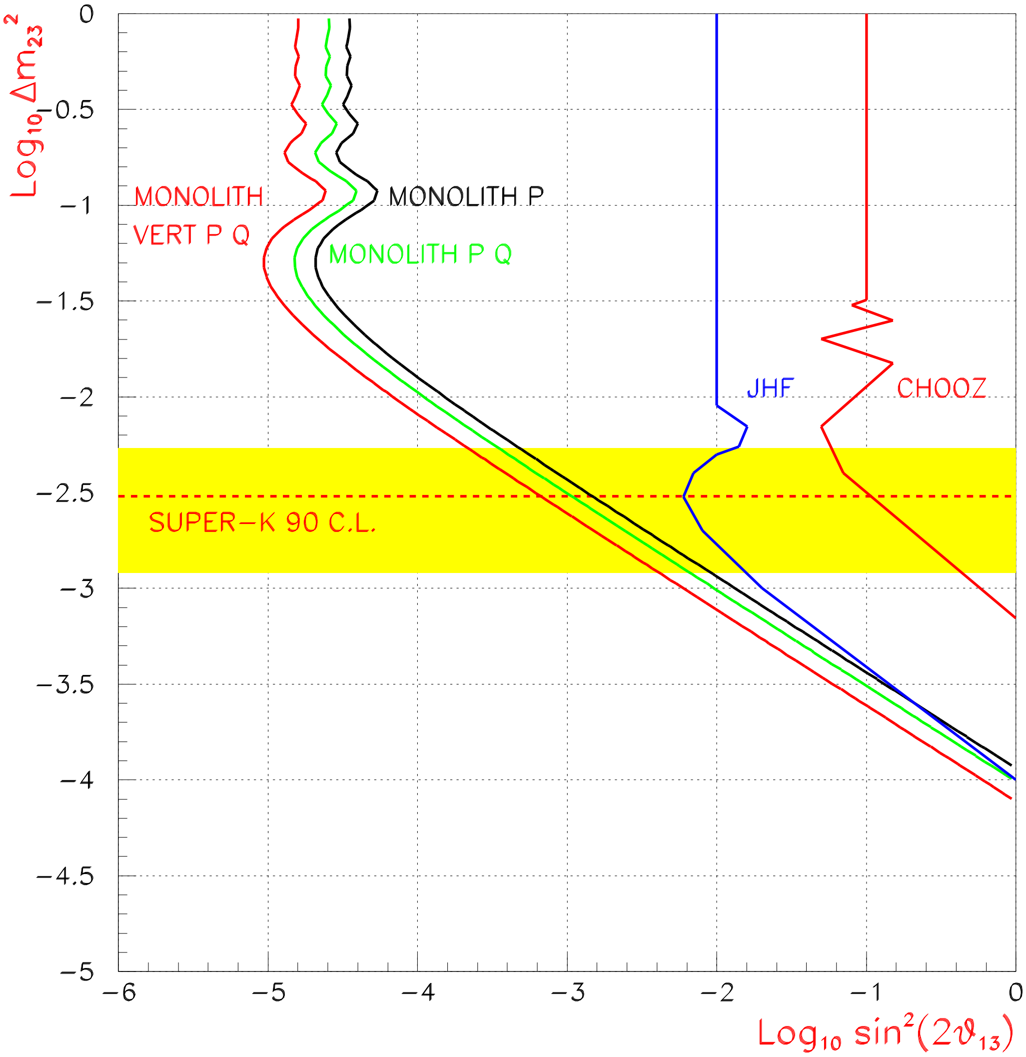

Figure 7.11: 4σ sensitivity region in the parameter space (Δm^2_{23} , θ_{13}) of the MONOLITH detector at the baseline of 732 km. *Black line:* horizontal-8 cm planes (just P_μ cut). *Green line:* horizontal-8 cm planes (combined P_μ and Q_t cut). *Red line:* vertical 8 cm planes (combined P_μ and Q_t cut). The Chooz excluded region [105] is superimposed as well as the sensitivity region of the future JHF SuperBeam (OAB 2° option) [131] and the Super-Kamiokande allowed Δm^2_{23} region.

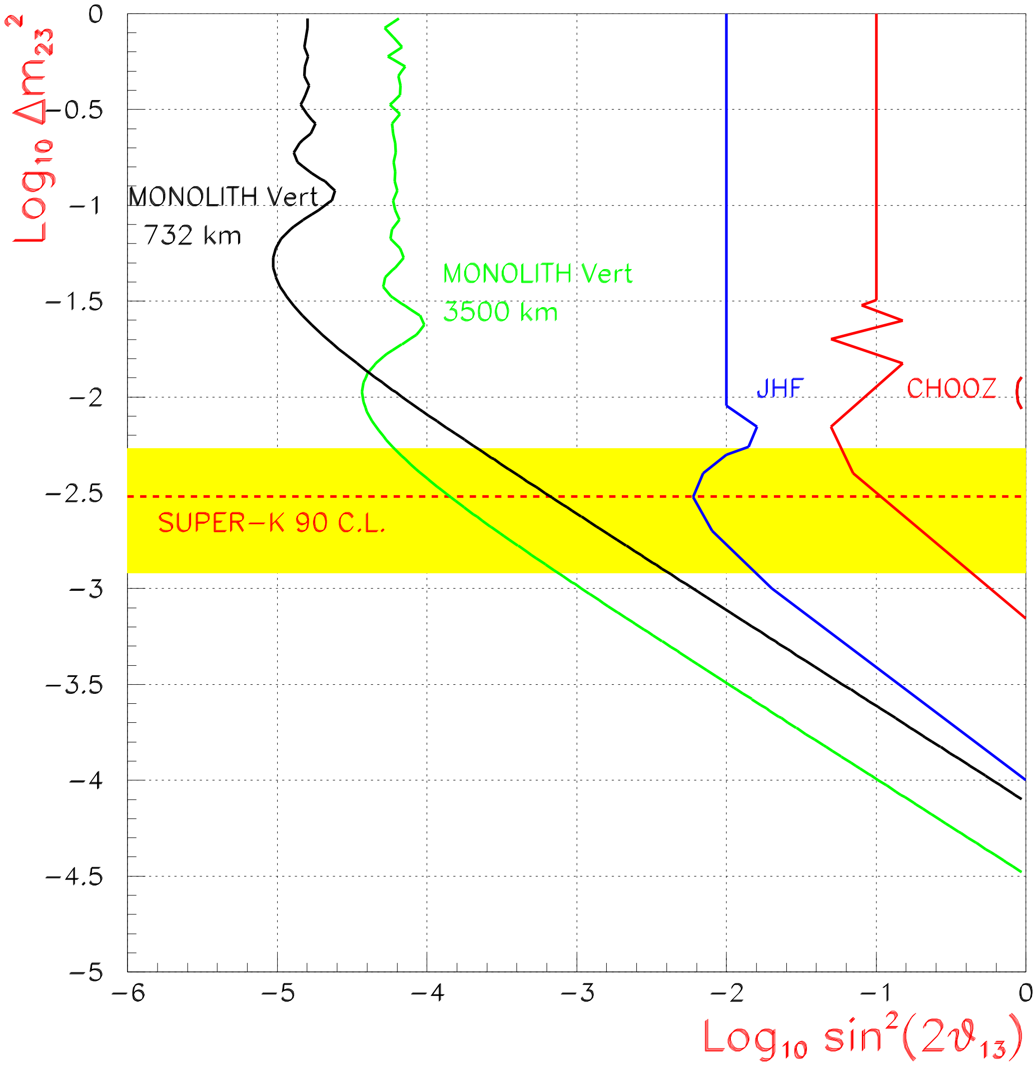

Figure 7.12: 4σ sensitivity region in the parameter space (Δm^2_{23} , θ_{13}) of the MONOLITH detector, in the vertical $8\ cm$ planes option. *Black line:* baseline $732\ km$ (i.e. CERN-Gran Sasso). *Green line:* baseline $3500\ km$ (i.e. CERN-Canary Island). The Chooz excluded region [105] is superimposed as well as the sensitivity region of the future JHF SuperBeam (OAB 2° option) [131] and the Super-Kamiokande allowed Δm^2_{23} region.

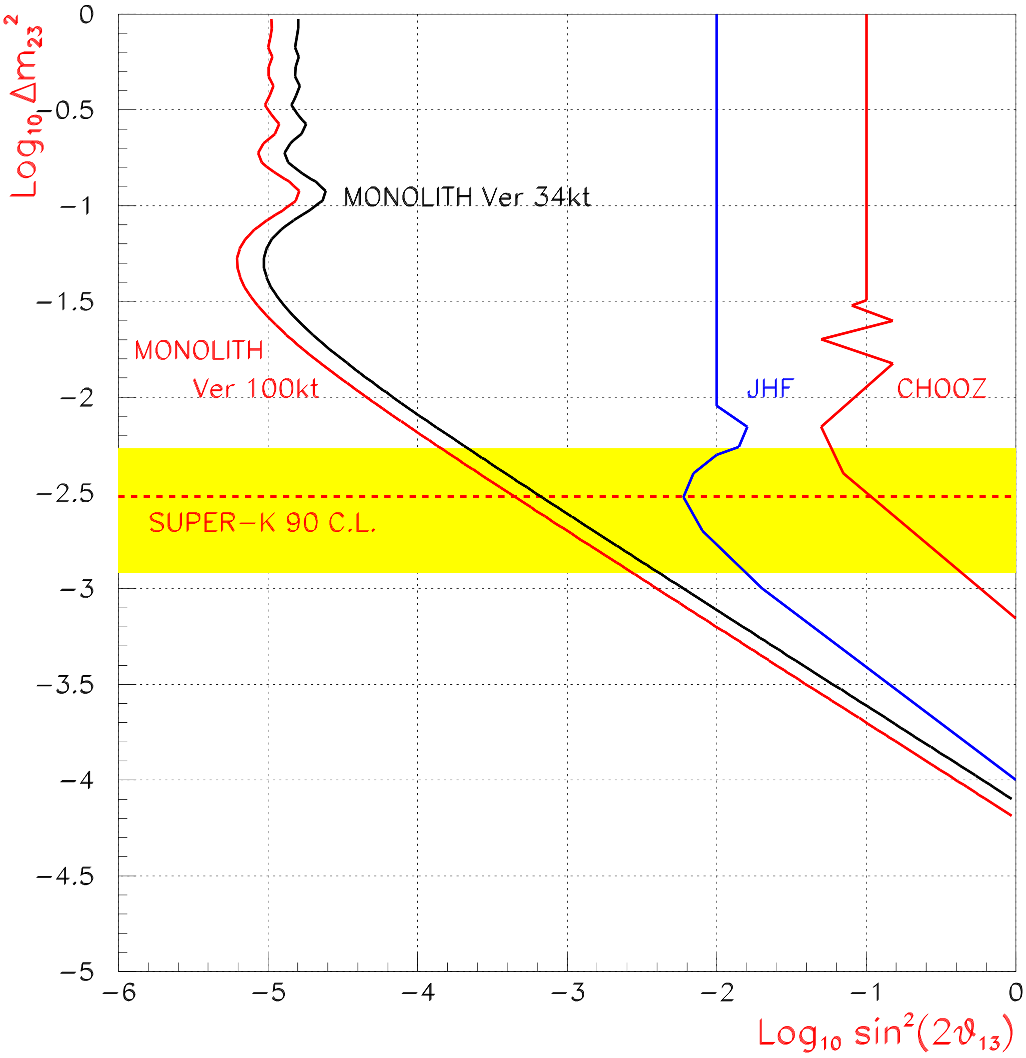

Figure 7.13: 4σ sensitivity region in the parameter space (Δm^2_{23} , θ_{13}) of the MONOLITH detector at the baseline of 732 km, in the vertical 8 cm planes option. *Black line:* detector mass 34 kt. *Red line:* detector mass 100 kt. The Chooz excluded region [105] is superimposed as well as the sensitivity region of the future JHF SuperBeam (OAB 2° option) [131] and the Super-Kamiokande allowed Δm^2_{23} region.

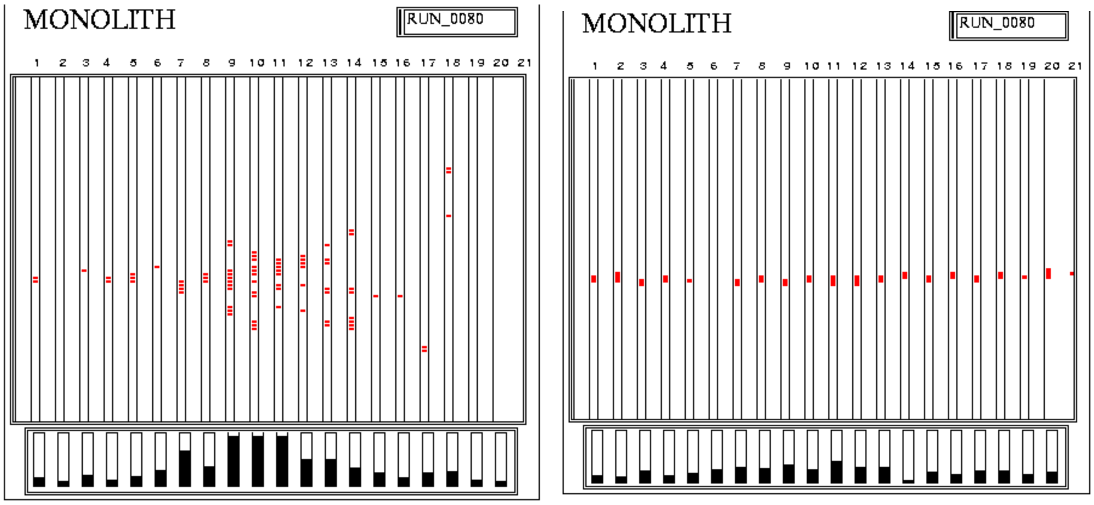

Figure 7.14: Event display of particles interacting in the calorimeter prototype. *Left:* 10 GeV pion. *Right:* 10 GeV muon.

7.8 Summary and conclusions

A realistic simulation of the performance of the MONOLITH detector as a target for a ν-factory beam has been developed. The hadron shower direction reconstruction and the charge identification of muons have been studied in detail.
Several background sources have been taken into account, as well as several detector configurations. A background rejection of the order of 10^{-6} is achievable, with an overall efficiency of 16%.

The sensitivity region in the $(\Delta m^2_{23}, sin^2(2\theta_{13}))$ parameter space is presented. It is about two order of magnitude better than the current Chooz limit in the whole Super-Kamiokande 90% $C.L.$ allowed region of Δm^2_{23}, if the baseline is 732 km; better at 3500 km.
This result is achieved also in the simplest version of the detector configuration and of the analysis, i.e. horizontal-8 cm planes and a simple muon momentum cut. Among the possible improvements, the best seems to be the vertical-8 cm planes option, that provides a very good hadronic background rejection. As shown in section 5.6, this choice of the detector has also good performances with atmospheric neutrinos.

The results of the analysis of a test beam prototype confirm that the requested hadronic angular resolution is achievable with the massive magnetized calorimeter design.

Moreover, it is shown in [132] that, having such good efficiency and background rejection power for the wrong sign muon signal, the MONOLITH detector on a ν-factory beam has the opportunity to study very important physics tasks as the sign of Δm^2, precise study of matter effects and, if the solar problem solution is the LMA one, CP-violation in the leptonic sector.

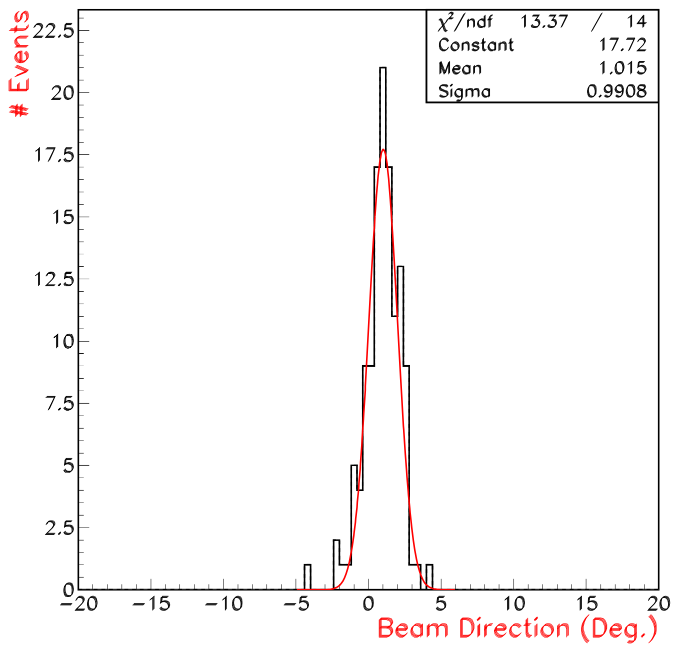

Figure 7.15: Angular distribution of the muons in the prototype.

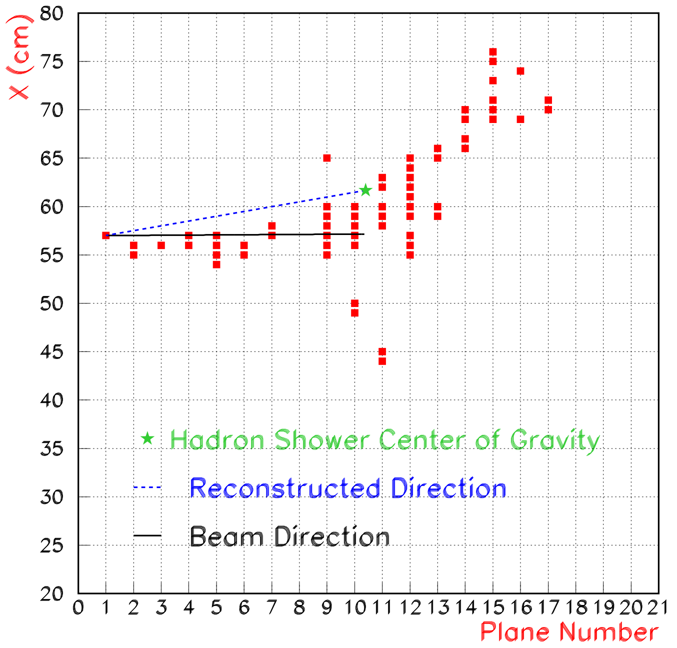

Figure 7.16: Hadronic shower direction as reconstructed in a pion event.

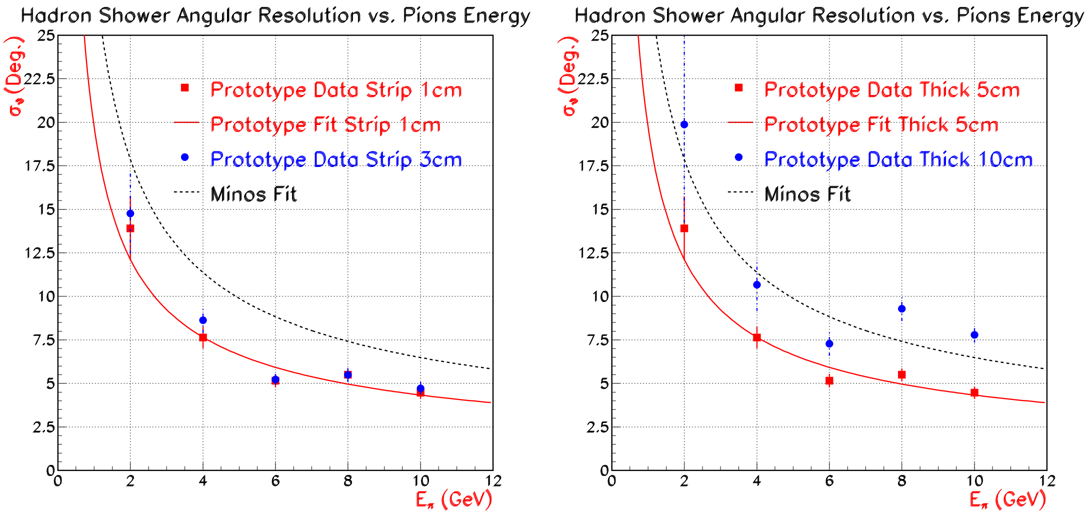

Figure 7.17: Hadronic angular resolution of the calorimeter prototype. *Left:* Comparison between the MINOS fit (black dashed line) and the results of the 5 *cm* thick prototype with 1 *cm* strip width (red squares and continuous line) and 3 *cm* strip width (blue dots). *Right:* Comparison between the MINOS fit (black dashed line) and the results of the 5 *cm* thick prototype (red squares and continuous line) and 5 *cm* thick prototype (blue dots).

Chapter 8

Conclusions

We showed the feasibility of a 34 kt magnetized iron detector which is able to give a crucial contribution in the current scenario of the neutrino oscillation experiments.

By exploiting the high energy component of the atmospheric muon neutrino fluxes, the massive magnetic calorimeter has the capability to detect the oscillation pattern from the comparison of L/E spectra of upgoing and downgoing neutrinos. The outlined analysis takes advantage of the up/down symmetry of the high energy atmospheric neutrino fluxes, which makes high energy atmospheric neutrinos an ideal source for disappearance experiments.

In the apparatus considered, the determination of the neutrino energy and direction relies mostly on the muon reconstruction. By means of the measurement of ν_μ disappearance, the existence of oscillations can be (dis)proved and the parameters measured over the entire range suggested by Super-Kamiokande and Kamiokande results. Moreover, unconventional models still consistent with Super-Kamiokande data can be discriminated by the observation of the oscillation pattern.

A full simulation of a different detector geometry, based on vertical planes, has been developed and results are comparable with the horizontal option. The main difference is the lower efficiency for large L/E events (i. e. near to vertical). However, these events are in the region where the oscillation averages, out of the first oscillation dip. This results in a lower precision in the mixing angle, but does not affect the determination of the Δm^2 and the capability to see the full first oscillation swing.

A 12 kt module shows resolutions similar to the full detector and efficiency lowered only by the minor fiducial volume. The collected statistics is therefore reduced by a factor 3.5. Taking data for four years allows to confirm the SK results with different systematics and to improve the precision of the Δm^2 parameter, but the discrimination between different physics mechanisms is not under reach.

We studied also the performances of the detector in the analysis of the events produced by the CERN to Gran Sasso neutrino beam.

Despite its design being optimised for atmospheric neutrinos, even the uniform detector option will allow to collect a huge amount of events from the beam with good resolution. An addition of vertical planes can increase the selection efficiency, in particular for $E_\nu \geq 15$ GeV.

Depending on Δm^2 and assuming a 10% systematic uncertainty in beam shape, a deficit of events as a function of L/E can be seen in 1 year of data taking.

Furthermore, the up/down analysis of MONOLITH from atmospheric neutrinos can be complemented by a big sample of data from the CNGS beam at small L/E to reduce statistical errors. Although this will make the analysis dependent on Monte Carlo and beam systematics, it will yield a useful complement, especially if Δm^2 lays in the upper part of the Super-Kamiokande allowed region. However, the systematic uncertainty due to the beam shape knowledge needs to be further investigated. The CNGS events could also act as redundant consistency check for the first years of data taking.

Of course, given the high interaction rate ($\sim$ 40000 selected events per year), the MONOLITH experiment can act as a good quality monitor of the CNGS beam.

A realistic simulation of the performance of the MONOLITH detector as a target for a ν-factory beam has been developed. The hadron shower direction reconstruction and the charge identification of muons have been studied in details.
Several background sources have been taken into account, as well as several detector configurations. A background rejection of the order of 10^{-6} is achievable, with an overall efficiency of 16%.

The sensitivity region in the (Δm^2_{23} , $sin^2(2\theta_{13})$) parameter space is presented. It is about two order of magnitude better than the current Chooz limit in the whole Super-Kamiokande 90% $C.L.$ allowed region of Δm^2_{23}, if the baseline is 732 km; better at 3500 km.

This result is achieved also in the simplest version of the detector configuration and of the analysis, i.e. horizontal-8 cm planes and a simple muon momentum cut. Among the possible improvements, the best seems to be the vertical-8 cm planes option, that provides a very good hadronic background rejection. We stress that this choice of the detector has also good performances with atmospheric neutrinos.

The results of the analysis of a test beam prototype confirm that the requested hadronic angular resolution is achievable with the massive magnetized calorimeter design.

Moreover, having such good efficiency and background rejection power for the wrong sign muon signal, the MONOLITH detector on a ν-factory beam has the opportunity to study very important physics tasks as the sign of Δm^2, precise study of matter effects and, if the solar problem solution is the LMA one, CP-violation in the leptonic sector.

Many of these measurements are unique to this detector, and therefore complementary to other planned neutrino physics programmes. They can be achieved on a relatively short timescale, at a cost which is dominated by the required detector mass. Furthermore, a detector of this kind, that could give a unique contribution to the current neutrino oscillations scenario both in the atmospherics and long-baseline projects, fits into even more ambitious long-term programmes for neutrino factories.

Acknowledgements

I would like to thank Evgeny Akhmedov, Pietro Antonioli, Giacomo Bari, Maurizio Basile, Graziano Bruni, Friedrich Dydak, Domenico Esposito, Francesco Esposito, Marco Garbini, Paolo Giusti, Juan Jose Gómez-Cadenas, Paolo Lipari, Helenia Menghetti, Rosario Nania, Anna Natali, Alessandro Pesci, Stefano Ragazzi, Gabriella Sartorelli, Cecilia Selvi and Tommaso Tabarelli de Fatis for their encouragement and for various but crucial contribution to the development of my Ph.D. thesis.

Bibliography

[1] Altmann M. F., Mossbauer R. L. and Oberauer L. J. N. , Rept. Prog. Phys. **64** (2001) 97-146;
J.N. Bahcall, P.I. Krastev, and A.Yu. Smirnov, Phys. Rev. **D 59** (1999) 046002;
N. Hata and P. Langacker, Phys. Rev. **D 56** (1997) 6107;
V. Castellani et al., Phys. Rep. **281** (1997) 309.

[2] see e.g. G.L. Fogli et al., Phys. Rev. **D 55** (1997) 4385; Phys. Rev. **D 57** (1998) 5893;
Y. Totsuka, talk given at *TAUP 2001*, Laboratori Nazionali del Gran Sasso, Italy, September 8-12 2001.

[3] Super-Kamiokande Collaboration, Y. Fukuda *et al.*, Phys. Rev. Lett. **81** (1998) 1562;
Super-Kamiokande Collaboration, Y. Fukuda *et al.*, Phys. Lett. **B 436** (1998) 33;
Super-Kamiokande Collaboration, Y. Fukuda *et al.*, Phys. Lett. **B 433** (1998) 9;
Super-Kamiokande Collaboration, Y. Fukuda *et al.*, Phys. Rev. Lett. **85** (2000) 3999;
J. Goodman, talk given at *Lepton Photon 01, XX International Symposium on Lepton and Photon Interactions at High Energies*, 23-28 July 2001, Rome Italy.

[4] KEK proposal E-362, K2K (KEK to Kamioka) neutrino oscillation experiment at KEK-PS, hep-ex/9803014.

[5] J. E. Hill for the K2K collaboration, hep-ph/0110034.

[6] Fogli *et al.*, hep-ph/0110089.

[7] LSND Collaboration, C. Athanassopoulos *et al.*, Phys. Rev. Lett. **75** (1995) 2650;
J.E. Hill, Phys. Rev. Lett. **75** (1995) 2654;
LSND Collaboration, C. Athanassopoulos *et al.*, Phys. Rev. **C 54** (1996) 2685;
LSND Collaboration, C. Athanassopoulos *et al.*, Phys. Rev. Lett. **77** (1996) 3082;
LSND Collaboration, C. Athanassopoulos *et al.*, Phys. Rev. **C 58** (1998) 2489;
LSND Collaboration, C. Athanassopoulos *et al.*, Phys. Rev. Lett. **81** (1998) 1774.

[8] see e.g. J. Primack and A. Klypin, Nucl. Phys. Proc. Suppl. **51 B** (1996) 30.

[9] see e.g. S. Pakvasa, Invited talk at *8th International Workshop on Neutrino Telescopes*, Venice, Italy, 23-26 Feb 1999, hep-ph/9905426, and references therein.

[10] V. Barger *et al.*, hep-ph/9907421;
V. Barger *et al.*, Phys. Rev. Lett. **82** (1999) 2640.

[11] R. Barbieri *et al.*, P. Creminelli, and A. Strumia, IFUP-TH-2000-00, hep-ph/0002199, February 2000.

[12] E. Lisi, A. Marrone, and D. Montanino, hep-ph/0002053, February 2000.

[13] G. Mannocchi *et al.*, CERN/OPEN-98-004.

[14] C. Albright *et al.*, FERMILAB-FN-692, May 2000.
V. Barger *et al.*, hep-ph/0003184, March 2000, hep-ph/0004208, April 2000.
A. Cervera *et al.*, hep-ph/0002108, February 2000.
A. Bueno, M. Campanelli, and A. Rubbia, hep-ph/0005007, May 2000.
M. Freund, P. Huber, and M. Lindner, TUM-HEP-373/00, hep-ph/0004085, April 2000.

[15] DONUT Collaboration, Taipei 2000, APPC 2000, 58-63.
Okada, K. for the DONUT Collaboration, talk at *Neutrino Oscillations Workshop NOW2000*, Conca Specchiulla, Italy, Sept. 9-16, 2000. Transparencies at http://www.ba.infn.it/ now2000/views/slides/

[16] Z. Maki, M. Nakagawa and S. Sakata, Prog. Theor. Phys. **28** (1962) 970;
Particle Data Group, Eur. Phys. Journ. **C 3** (1998) 1.

[17] S. Sarkar, Rep. Prog. Phys. **59** (1996) 1493; hep-ph/9602260.

[18] B. Pontecorvo, Sov. Phys. JETP **6** (1958) 429;
Sov. Phys. JETP **7** (1958) 172.

[19] Z. Maki, M. Nakagawa, S. Sakata, Progr. Theor. Phys. **28** (1962) 870.

[20] S.M. Bilenky, C. Giunti, W. Grimus, Prog. Part. Nucl. Phys. **43** (1999) 1.

[21] Baudis, L. *et al.*, Heidelberg-Moscow Collaboration (1999) *Phys. Rev. Lett.* **83**, 41.

[22] Ejiri, H., Talk given at *Neutrino 2000*, see ref. [28].

[23] G.G. Raffelt, W. Rodejohann, Lectures given at *4th National Summer School for German-speaking Graduate Students of Theoretical Physics*, Saalburg, Germany, 31 Aug - 11 Sep 1998, hep-ph/9912397.

[24] S.P. Mikheyev, A.Yu. Smirnov, Sov. Phys. Usp. **30** (1987) 759;
Prog. Part. Nucl. Phys. **23** (1989) 41.

[25] S.M. Bilenky, J. Hošek, S.T. Petcov, Phys. Lett. **B94** (1989) 495;
I.Yu. Kobzarev *et al.*, Sov. J. Nucl. Phys. **32** (1980) 823;
M. Doi *et al.*, Phys. Lett. **B102** (1981) 323;
P. Langacker *et al.*, Nucl. Phys. **B282** (1987) 589.

[26] L. Wolfenstein, Phys. Rev. **D 17** (1978) 2369; Phys. Rev. **D 20** (1979) 2634;
S.P. Mikheyev and A.Y. Smirnov, Sov. J. Nucl. Phys. **42** (1985) 913; Nuovo Cimento **9C** (1986) 17.

[27] For reviews see, e.g., [24, 20] and T.K. Kuo, J. Pantaleone, Rev. Mod. Phys. 61 (1989) 937.

[28] Lobashev, V.M., Talk given at the *XIX Intern. Conf. on Neutrino Phys. and Astrophys. "Neutrino 2000"*, Sudbury, Canada, June 16 – 21, 2000. Tranparencies at http://nu2000.sno.laurentian.ca/

[29] Suzuki, Y., Talk given at *Neutrino 2000*, see ref. [28].

[30] Gonzalez-Garcia, M.C. *et al.*, hep-ph/0009350.

[31] Recent fits of the solar neutrino data can also be found in Gonzalez-Garcia, M.C. and Peña-Garay, C., hep-ph/0009041; talks given by Montanino, D. and Palazzo, A. at *NOW2000*, see ref. [15]; Gonzalez-Garcia, M.C. *et al.*, ref. [30].

[32] Fogli, G.L., Lisi, E. and Montanino (1996) *Phys. Rev.* **D54**, 2048.

[33] Giunti, C., Gonzalez-Garcia, M.C. and Peña-Garay, C. (2000) *Phys. Rev.* **D62**, 013005.

[34] de Gouvêa, A., Friedland, A. and Murayama, H. (2000) *Phys. Lett.* **B490**, 125.

[35] Smirnov, A.Yu., Talk given at *Neutrino 2000*, see ref. [28]; hep-ph/0010097.

[36] McDonald, A.B. for the SNO Colaboration, Talk given at *Neutrino 2000*, see ref. [28]; hep-ex/0011025.

[37] For recent discussions see de Gouvêa, A., Friedland, A. and Murayama, H., hep-ph/9910286;
Fogli, G.L. *et al.* (2000) *Phys. Rev.* **D61**, 073009.

[38] CHOOZ Collaboration, Apollonio, M. *et al.*, *Phys. Lett.* **B466**, 415.

[39] Mills, G. for the LSND Collaboration, Talk given at *Neutrino 2000*, see ref. [28].

[40] Eitel, K. for the KARMEN Collaboration, Talk given at *Neutrino 2000*, see ref. [28]; hep-ex/0008002.

[41] Bazarko, A.O. for the MiniBooNE Collaboration, Talk given at *Neutrino 2000*, see ref. [28]; hep-ex/0009056.

[42] The NUMI-MINOS Project, NUMI-L-375 report (may 98); The MINOS Detectors TDR, NUMI-L-337 report (october 98 version).

[43] S. Wojcicki, Proceedings of Neutrino '98, Takayama, Japan, June 4-9, 1998.

[44] Y. Oyama (E362 (K2K) Collaboration), Proceedings of *XXXV Rencontres de Moriond "Electroweak interactions and unified theories"*, Les Arcs, Savoie, France, March 11-18, 2000, hep-ex/0004015, and references therein.

[45] CDHS Collaboration, F. Dydak *et al.*, Phys. Lett. **B 134** (1984) 281;
CHARM Collaboration, F. Bergsma *et al.*, Phys. Lett. **B 142** (1984) 103;
E776 Collaboration, L. Borodowsky *et al.*, Phys. Rev. Lett. **68** (1992) 274;
KARMEN Collaboration, B. Zeitnitz *et al.*, Prog. Part. Nucl. Phys.**40** (1998) 169;
Bugey Collaboration, B. Achkar *et al.*, Nucl. Phys. **B 434** (1995) 503;
Krasnoyarsk Collaboration, G.S. Vidyakin *et al.*, JETP Lett. **59** (1994) 237.

[46] H. Sobel (Super-Kamiokande Collaboration), Proceedings of *XIX International Conference on Neutrino Physics and Astrophysics (Neutrino 2000)*, Sudbury, Canada, June 16-21, 2000.

[47] Kamiokande Collaboration, Y. Fukuda *et al.*, Phys. Lett. **B 335** (1994) 237.

[48] K. Elsener (editor), CERN 98-02 and INFN/AE-98/05, May 1998;
R. Bailey *et al.*, CERN-SL-99-034-DI, June 1999.

[49] A. Ereditato, K. Niwa, and P. Strolin, INFN/AE-97/06, Nagoya DAPNU-97-07, January 1997;
OPERA Coll., *Experiment Proposal OPERA: an Appearance Experiment to Search for* $\nu_\mu \to \nu_\tau$ *Oscillations in the CNGS Neutrino Beam,* CERN/SPSC 2000-028, SPSC/P318, LNGS P25/2000, July 2000;
A.E. Asratyan et al., Nucl. Instr. and Meth. A450, 1 (2000).

[50] CHORUS Collaboration, E. Eskut *et al.*, Phys. Lett. **B 424** (1998) 202;
CHORUS Collaboration, E. Eskut *et al.*, Phys. Lett. **B 434** (1998) 205.

[51] ICARUS Collaboration, P. Benetti *et al.*, Nucl. Instr. Methods **A 327** (1993) 327; **A 332** (1993) 332; P. Cennini *et al.*, Nucl. Instr. Methods **A 333** (1993) 567;
A 345 (1994) 230; **A 355** (1995) 355;
ICARUS-CERN-Milano Collaboration, CERN/SPSLC 96-58, SPSLC/P 304, December 1996.
ICARUS Collaboration, ICARUS-TM/2001-08 LNGS-EXP 13/89 add.2/01

[52] NOMAD Collaboration, J. Altegoer *et al.*, Phys. Lett. **B 431** (1998) 219;
NOMAD Collaboration, P. Astier *et al.*, Phys. Lett. **B 453** (1999) 169.

[53] W.W.M.Allison *et al.*, Physics Letters B 449 (1999) 137

[54] MACRO Collaboration, M.Ambrosio *et al.*, INFN-AE 98/13 (1998); hep-ex/9807005
Phys. Lett. B434 (1998) 451-457

[55] Sobel, H., Talk given at *Neutrino 2000*, see ref. [28]; Learned, J.G., hep-ex/0007056.

[56] Kajita, T., Talk given at NOW2000, see ref. [15].

[57] The Super-Kamiokande Collaboration, Fukuda, S. *et al.*, hep-ex/0009001.

[58] Fogli, G.L, Lisi, E. and Marrone, A., hep-ph/0009299.

[59] Fogli, G.L. *et al.*, hep-ph/0009269.

[60] Barger, V. *et al.* (1999) *Phys. Lett.* **B462**, 109.

[61] The MONOLITH coll., LNGS P26/2000, CERN/SPSC 2000-031, SPSC/M657, August 15, 2000.

[62] A. Curioni *et al.*, hep-ph/9805249;
M. Aglietta *et al.*, LNGS-LOI 15/98, CERN/SPSC 98-28, SPSC/M615, Oct. 1998.

[63] MONOLITH Progress Report, LNGS-LOI 20/99, CERN/SPSC 99-24, August 1999.

[64] I216/P311 Proposal, M. Guler at al., CERN-SPSC/99-26, SPSC/P311, August 1999.

[65] G. Bencivenni *et al.*, Nucl. Instr. and Method **A 300** (1991) 572.

[66] G. Bencivenni *et al.*, Nucl. Instr. and Method **A 315** (1992) 507.

[67] M. De Deo *et al.*, LNGS -95/39, June 1995.

[68] G. Bencivenni *et al.*, Nucl. Instr. and Method **A 345** (1994) 456.

[69] G. Bencivenni *et al.*, Nucl. Instr. and Method **A 332** (1993) 368.

[70] C. Gustavino *et al.*, INFN/TC-99/14,Nucl. Instr. and Method. accepted

[71] K. Abe *et al.*, "Glass RPC Module for Belle Endcap KL/mu Detector", Proc. of *IV Int.Workshop on Resistive Plate Chamber and Related Detectors*, Napoli, Oct 15-16 1997. Ed. Sergio Ratti, Riccardo de Asmundis.
A. Abashian *et al.*,Nucl. Instr. and Meth. **A 449** (2000) 112-124.
K. Abe *et al.*Nucl. Instr. and Meth. **A** (2000), accepted.

[72] C. Gustavino *et al.*, *Proc. of RPC99*, Bari, 1999, in press; *Nucl. Instr. and Meth* submitted.
M. Ambrosio *et al.*, The MONOLITH Prototype, Proceedings of the Bari RPC workshop, October 1999, ftp://netview.ba.infn.it/rpc/proceedings/gustavino.ps, submitted to Nucl. Instr. and Meth.

[73] C. Gustavino *et al.*, *Proc. of 8th Pisa Meeting on Advanced Detectors*, La Biodola, Isola d'Elba, 2000, in press; *Nucl. Instr. and Meth*,accepted.

[74] GEANT Detector Description and Simulation Tools, CERN Program Library, Long Writeup W5013.

[75] R. E. Kalman, J. Basic Eng. 82 (1961) 34;
R. E. Kalman and R. S. Bucy, ibid. 83 (1961) 95;
see also W. Ledermann and E. Lloyd editors, *Handbook of Applicable Mathematics, Volume VI: Statistics*, John Wiley and Sons 1984, pag. 897.

[76] R. Fruhwirth, Nucl. Instrument and Method A 262 (1987) 444; *and references therein.*

[77] V. Agrawal, T.K. Gaisser, P. Lipari and T. Stanev, Phys. Rev. **D 53** (1996) 1314.

[78] M. Gluck, E. Reya and A. Vogt, Z. Phys. **C 67** (1995) 433.

[79] P. Lipari, M. Lusignoli and F. Sartogo, Phys. Rev. Lett. **74** (1995) 4384.

[80] T. K. Gaisser and T. Stanev, astro/ph-9708146.

[81] M. Honda *et al.*, Phys. ReV **D52** (1995) 4985.

[82] G. Battistoni *et al.*, Astroparticle Phys. **12**, 315 (2000).

[83] Y. Tserkonvyak at al., hep-ph/9907450.

[84] P. Lipari, hep-ph/0002282.

[85] P. Lipari, T. K. Gaisser and T. Stanev, Phys. Rev. **D 58** (1998) 073003.

[86] G. Battistoni and P. Lipari, hep-ph/9807475.

[87] P. Picchi and F. Pietropaolo, "Atmospheric Neutrino Oscillations Experiments", ICGF RAP. INT. 344/1997, Torino 1997, (CERN preprint SCAN–9710037).

[88] C. Walter (Super-Kamiokande Collaboration) Proceedings of EPS '99, Tampere, Finland, 15-21 July 1999.

[89] A. Curioni and T. Tabarelli de Fatis, *Geometrical sampling of L/E distributions*, NOSEX-003/98, unpublished.

[90] T. Tabarelli de Fatis, *Oscillations and experimental resolution*, NOSEX-002/98, unpublished.

[91] MINUIT, Function Minimization and Error Analysis, CERN Program Library Long Writeup D506.

[92] See for example: W.T. Eadje *et al.*, *Statistical Methods in Experimental Physics*, North-Holland Publishing Company, 1971, p. 243

[93] V. Innocente *et al.*, "GEANE : average tracking and error propagation package" in *Proceedings of Workshop on detector and event simulation in high energy physics* : Monte Carlo '91 Amsterdam, Netherlands ; 8 - 12 Apr 1991, edited by K. Bos and B. van Eijl, NIKHEF, Amsterdam, (1991) 58-78.

[94] P. Antonioli *et al.*, *First Study of MONOLITH performance on CNGS beam*, MONOLITH xx/2000, unpublished

[95] M. Bonesini *et al.*, Eur. Phys. J. C20 (2001) 13.

[96] http://proj-cngs.web.cern.ch/proj-cngs/cngs.htm, provided by F. Pietropaolo.

[97] Super-Kamiokande Collaboration, Y. Fukuda *et al.*, Phys. Lett. **B 433** (1998) 9;
Phys. Lett. **B 436** (1998) 33; Phys. Rev. Lett. **81** (1998) 1562;
Phys. Rev. Lett. **82** (1999) 2644; Phys. Lett. **B 467** (1999) 185;
T. Kajita, Nucl. Phys. **B** (Proc. Suppl.) **77** (1999) 123.

[98] Kamiokande Collaboration, S. Hatakeyama *et al.*, Phys. Rev. Lett. **81** (1998) 2016;
Soudan-2 Collaboration, E. Peterson, Nucl. Phys. **B** (Proc. Suppl.) **77** (1999) 111;
W. W. Allison, Phys. Lett. **B 449** (1999) 137;
MACRO Collaboration, F. Ronga *et al.*, Nucl. Phys. **B** (Proc. Suppl.) **77** (1999) 117.

[99] R. Davis *et al.*, Phys. Rev. Lett. **20** (1968) 1205;
B. T. Cleveland *et al.*, Astrophys. J. **496** (1998) 505;
K. Lande *et al.*, Nucl. Phys. (Proc. Suppl.) **77** (1999) 13;
T. Kirsten, Nucl. Phys. (Proc. Suppl.) **77** (1999) 26;
Kamiokande Collaboration, Y. Fukuda *et al.*, Phys. Rev. Lett. **77** (1996) 1683;
SAGE Collaboration,
Dzh. N. Abdurashistov *et al.*, Nucl. Phys. (Proc. Suppl.) **77** (1999) 20;
Super-Kamiokande Collaboration,
Y. Fukuda *et al.*, Phys. Rev. Lett. **82** (1999) 1810;
M. Smy *et al.*, hep-ex/9903034.

[100] B. Pontecorvo, J. Expt. Theor. Phys. **33** (1957) 549;
J. Expt. Theor. Phys. **34** (1958) 247; Sov. Phys. JETP **26** (1968) 984.

[101] A. de Gouvea, A. Friedland, H. Murayama, hep-ph/0002064.

[102] Super-Kamiokande home-page, http://www-sk.icrr.u-tokyo.ac.jp/doc/sk;
SNO home-page, http://snodaq.phy.queensu.ca/SNO/sno.html;
BOREXINO home-page, http://almime.mi.infn.it;
HERON home-page, http://www.physics.brown.edu/research/heron;
HELLAZ home-page, http://sg1.hep.fsu.edu/hellaz.

[103] K. Nishikawa, Nucl. Phys. (Proc. Suppl.) **77** (1999) 198;
B. C. Barish, Nucl. Phys. (Proc. Suppl.) **70** (1999) 227.

[104] D. A. Petyt,
"A study of parameter measurement in a long-baseline neutrino oscillation experiment",
Thesis submitted to Univ. of Oxford, England, 1998.

[105] M. Apollonio *et al.*, hep-ex/9907037.

[106] M.C. Gonzalez-García and C. Peña-Garay, hep-ph/0001129.

[107] S. Geer, Phys. Rev. **D 57** (1998) 6989.

[108] C. M. Ankenbrandt *et al.* (Muon Collider Collaboration),
Phys. Rev. ST Accel. Beams **2**, (1999) 081001;
B. Autin *et al.*, CERN-SPSC/98-30, SPSC/M 617 (October 1998);
S. Geer, C. Johnstone and D. Neuffer, FERMILAB-PUB-99-121.

[109] S. Geer and R. Raja,
"Workshop on Physics at the first muon collider and at the front end of a muon collider",
AIP Conf. Proc. **435** (1998).

[110] A. de Rújula, M. B. Gavela and P. Hernández, Nucl. Phys. **B 547** (1999) 21.

[111] B. Autin, A. Blondel and J. Ellis,
"Prospective study of muon storage rings", CERN 99-02, ECFA 99-197.

[112] K. Dick, M. Freund, M. Lindner and A. Romanino, Nucl. Phys. **B 562** (1999) 29.

[113] A. Donini, M. B. Gavela, P. Hernández and S. Rigolin, hep-ph/9909254.

[114] P. Lipari, Phys. Rev. **D61** (2000) 113004

[115] J. Ellis, hep-ph/9911440.

[116] V. Barger, S. Geer, R. Raja and K. Whisnant, hep-ph/9911524.

[117] M. Campanelli, A. Bueno and A. Rubbia, hep-ph/9905240.

[118] V. Barger, S. Geer and K. Whisnant, Phys. Rev. **D 61** (2000) 053004.

[119] I. Mocioiu and R. Shrock, hep-ph/9910554.

[120] M. Freund, M. Lindner, S. T. Petcov and A. Romanino, hep-ph/9912457.

[121] Nufact '99 Workshop, July 5-9th, Lyon; http://lyoninfo.in2p3.fr/nufact99/.

[122] The Neutrino Factory and Muon Collider Collaboration,
K. T. McDonald *et al.*, physics/9911009.

[123] See for example: T. K. Gaisser, *"Cosmic Rays and Particle Physics"*, Cambridge University Press, 1990.

[124] G. L. Fogli, E. Lisi, A. Marrone and G. Scioscia,
Phys. Rev **D59** (1999) 033001 and hep-ph/9904465.

[125] A. de Rújula, M. B. Gavela and P. Hernández, hep-ph/0001124.

[126] A. Cervera-Villanueva, F. Dydak and J.J. Gómez-Cadenas, talk given at *ν-Fact '00*, May 22-26th 2000, Monterey.

[127] A. Cervera-Villanueva, F. Dydak and J.J. Gómez-Cadenas,
talk given at *ν-Fact '99*, July 5-9th, Lyon.

[128] P. Lipari *et al.*, Phys. Rev. Lett. 74 (1995), 4384.

[129] P-875: A long-baseline neutrino oscillation experiment at Fermilab, NuMI-L-63 (1995);
http://www.hep.anl.gov/NDK/Hypertext/numi.html

[130] A. Cervera-Villanueva, talk given at the *Workshop on a Massive Underground Neutrino Detector with Leptonic Charge Sign Discrimination*, November 9-11 2001, Sitges.

[131] Y. Itow *et al.*, hep-ex/0106019.

[132] A. Cervera-Villanueva *et al.*, hep-ph/0002108.